REDOX CYCLING FOR AN IN-SITU ENZYME LABELED IMMUNOASSAY ON INTERDIGITATED ARRAY ELECTRODES

A Thesis
Presented to
The Academic Faculty

By

Sang Kyung Kim

In Partial Fulfillment
of the Requirement for the Degree
Doctor of Philosophy in
Bioengineering

Georgia Institute of Technology
August 2004

REDOX CYCLING FOR AN IN-SITU ENZYME LABELED IMMUNOASSAY ON INTERDIGITATED ARRAY ELECTRODES

Approved by:

Dr. Peter J. Hesketh, Advisor

Dr. Dale Edmondson

Dr. Albert B. Frazier

Dr. William D. Hunt

Dr. Jiri Janata

Date Approved: August 17. 2004

This thesis is dedicated to my parents, Hyung-Gon Kim and Young-Ok Cho,

without whom it would never have been accomplished.

ACKNOWLEDGMENTS

I would like to thank my thesis committee- Dr. Peter Hesketh, Dr. Dale Edmondson, Dr. William Hunt, Dr, Albert Frazier, and Dr. Jiri Janata- for their time, energy and assistance. I would like to give special thanks and acknowledge Dr. Hesketh for his unwavering encouragement and support, who provided guidance in various areas that helps me accomplish my research goals. I always owe to Dr. Hesketh for broadening my scientific and engineering view as well as the kind of researcher I have become today. I would also like to thank Dr. William Heineman for all his advice and input into the biochemical aspect of the project.

A number of individuals have been very helpful to me. I would first like to thank Dr. Jennifer Thomas, just graduated from University of Ciccinati, who carried out the project with me and made good contributions to the biochemical part. I would also like to thank all the lab members, especially Rajesh Luharuka and Arnab Choudhury, for their help on SLA fabrication, Sounghwan Lyu, for his help in modeling flow field, Dr. Hongseok Noh for his technical help. I would also thank Yoonsu Choi and Yongkyu Yoon, at Dr. Allen's group, for their help on fabrication in the cleanroom. The staffs of the MiRC cleanroom have been more than helpful in running and understanding the equipment.

I also want to give a personal thanks to my close friends at Chicago who have always been generous and understanding as well as my husband Kwangpyo Kim for his unconditional support.

TABLE OF CONTENTS

ACKNOWLEDGMENTS iii

LIST OF TABLES vii

LIST OF FIGURES viii

SUMMARY xii

1. INTRODUCTION 1
1.1. Motivations for the Electrochemical Enzyme Assay with IDA Electrodes 1

2. BACKGROUND 4
2.1. Redox Cycling On IDA Electrodes 4
2.2. General Equation for a Diffusion Limited Current 6
2.3. Model of Redox Current on IDA Electrodes 8
2.4. Fabrication Methods of IDA Electrodes 12
2.4.1. Directionality of Metal Deposition with an Evaporator 13
2.4.2. Carbon Electrodes 15
2.5. Electrochemical Immunoassay 16
2.5.1. Sandwich Immunoassay 17
2.5.2. 4-Aminophenol as a Reversible Analyte. 19
2.5.3. Paramagnetic Beads as a Solid Phase 21
2.6. Magnetic Collector in a Microfluidic System 23
2.6.1. Superparamagnetic Microbeads: Dynabeads 24
2.6.2. Permanent Magnet vs. Electromagnet 27
2.7. Fluid Flow in a Microchannel 30
2.8. Stereolithography: Design and Fabrication of Microchannel 33

3. FABRICATION OF IDA ELECTRODE 35
3.1. Fabrication of Coplanar IDA Electrodes 36
3.1.1. Oxidation 39
3.1.2. Photolithography 40
3.1.3. Metal Deposition 41
3.1.4. Lift-Off 43
3.1.5. PECVD of Si_3N_4 44
3.1.6. Reactive Ion Etching of Silicon Nitride Layer 45
3.1.7. Photoresist Removal & Cleaning 46
3.1.8. Dicing and Wiring 47
3.2. Fabrication of Comb IDA Electrodes 48
3.2.1. Si Etching: Bosch Process 50
3.2.2. Thermal Oxidation 54

3.2.3. Planarization of the Surface 56
3.2.4. Photolithography for Metal Pattern 57
3.2.5. Tilted E-Beam Evaporation 58
3.2.6. Photplithography for Passivation. 60
3.3. Fabrication of Comb IDA Electrodes for a Microfluidic System. 62
3.3.1. Electroplating of Ag 65
3.3.2. Electroless Chlorination of Ag 66
3.3.3. Stability of Ag/AgCl Reference Electrode 68

4. CHARACTERIZATION OF IDA ELECTRODES 70
4.1. Methods 71
4.2. Comparison of Pt and Au Electrodes 72
4.3. Stability of Pt Thin Film Electrodes 73
4.4. Dual Mode CV for Redox Cycling 78
4.5. Simulation of Redox Current on Coplanar and Comb IDA Electrodes 80
4.6. Comparison of Coplanar and Comb Electrodes 82

5. ELECTROCHEMICAL IMMUNOASSAY WITH IDA ELECTRODES 85
5.1. PAP/ PQI Redox Couple 86
5.1.1 Cyclic Votammetry of PAP/PQI in Alkaline Conditions. 86
5.1.2 Electrode Contamination and Cleaning 89
5.1.3 The Effect of pH 93
5.1.4 Dual Mode CV and CA 97
5.1.5 PAP Calibration Curve 100
5.2. β-Galactosidase as an Enzyme Label 102
5.2.1 Immobilization of β-Galactosidase on Microbeads 105
5.2.2 Experiments with a Rotating Disk Electrode 109
5.3. Immunoassay with Coplanar IDA Electrodes 111
5.3.1 Materials and Methods 111
5.3.2 Experimental Setup 113
5.3.3 Minimum Detectable Number of Beads 115
5.3.4 Mouse IgG Immunoassay 118
5.4. Comb IDA Electrodes for Microbead-Based Immunoassay 121
5.4.1 Horizontal Configuration of the Experiment 123
5.4.2 Current Response vs. Time 124
5.5. Reproducibility 128

6. MAGNETIC COLLECTOR 130
6.1 Model for a Magnetic Collector 131
6.1.1 Model for a Magnetic Collector 131
6.1.2 Calculation of the Equations 135
6.2. Distribution of Magnetic Beads in the Model 140
6.2.1 Interpretation of D_x (Distance of Settling) 140
6.2.2 The Length of Effective Magnetic Field 141
6.2.3 Collecting Efficiency vs. Flow Rate 142

6.3. Magnetic Beads Entrapped in a Real System 144
6.3.1 Methods 145
6.3.2 Comparison of the Model and the Real Magnetic Collector 147

7. IDA ELECTRODE INTEGRATED IN A MICROCHANNEL 149
7.1 Design of Microchannel and Platform 149
7.2 Fabrication of Microchannel Assembly 152
7.2.1 Stereolithography 152
7.2.2 PDMS Process 153
7.2.3 Material Stability of SLA and PDMS 154
7.2.4 Microbead Holdover on the Microchannel 155
7.2.5 Stabilization of Redox Cycling in a Microchannel 157
7.3. Viral Detection in a Microchannel 159
7.3.1 Methods 161
7.3.2 Minimum Detectable Number of Beads 164
7.3.3 MS2 Assay with RDE 167
7.3.4 MS2 Assay with IDA in a Fluidic Channel 169
7.3.5 Number of Beads vs. Signal from NSA 174

8. CONCLUSION 176

REFERENCES 181

LIST OF TABLES

Table 1 Steady state current for different IDA electrodes during CA…….. 84

Table 2 Calculated collecting efficiency of Dynabead M-280 for different flow rates (25 ~ 200 μL/min)…… 143

Table 3 Current response with varied number of beads in a IDA-integrated fluidic channel……... 175

Table 4 Comparison of 3 electrochemical immunoassay systems with IDA Electrodes ……180

LIST OF FIGURES

Figure 1 Conceptual diagram of redox cycling on an IDA electrode…… 3

Figure 2 Models for coplanar and comb IDA electrodes and resulted flux……...11

Figure 3 Time evolution of the evaporative coating of a feature with aspect ratio of 1.0……14

Figure 4 Enzyme labeled sandwich immunoassay ……... 18

Figure 5 Procedure of immunoassay with paramagnetic beads as a solid phase...22

Figure 6 Dynabeads M-280; superparamagnetic beads with diameter of 2.8 μm. … …….. 26

Figure 7 An equivalent electromagnet for a disk-shaped permanent magnet….. 29

Figure 8 Schematic of SLA system……. 34

Figure 9 Fabrication process for coplanar IDA electrodes …….. 37

Figure 10 IDA electrode fabricated with a mask of 2 μm gap between fingers… 38

Figure 11 Fabrication process for comb IDA electrodes…… 49

Figure 12 SEM image of trenches after 20 cycles of standard Bosch process….. 52

Figure 13 AFM image of a sidewall of a trench……. 53

Figure 14 (a) PECVD oxide (b)Thermal oxide…….. 55

Figure 15 Evaporated platinum layer on the sidewall of trench……. 59

Figure 16 Cross-section of a comb IDA electrode……. 61

Figure 17 The IDA chip for integration to a microfluidic system……. 64

Figure 18 The surface of electroplated Ag is chlorinated to form a AgCl layer… 67

Figure 19 Potentials of Ag/AgCl reference electrodes vs. time……. 69

Figure 20 Surface of IDA electrodes after 100 cyclic voltammetry……...73

Figure 21 Cyclic voltammogram for Pt disk and thin film electrodes in PBS buffer (pH 7). …….. 76

Figure 22 Cyclic voltammograms of a Pt IDA electrode for the stability test..... 77

Figure 23 Cyclic voltammograms with and without redox cycling……79

Figure 24 The calculated limiting current vs. size of gap for coplanar and comb electrodes…….……81

Figure 25 Dual mode cyclic voltammograms for coplanar and comb IDA electrodes …….. 83

Figure 26 Cyclic voltammograms of 1 mM PAP in tris buffer (pH 9.0)……88

Figure 27 Cyclic voltammograms of 10 mM $Fe(CN)_6^{3-}$ in phosphate buffer (pH 7) before and after experiments with PAP at pH 9…… 91

Figure 28 Cyclic voltammograms of clean tris buffer (pH 9) after fixed potential was applied in concentrated PAP solution…….92

Figure 29 pH dependency of PAP/PQI reversibility…….. 94

Figure 30 Cyclic voltammograms of 1 mM PAP in phosphate buffer (pH 7.5)….95

Figure 31 Cyclic voltammograms of 10 mM $Fe(CN)_6^{3-}$ in phosphate buffer (pH 7.5) before and after experiments with PAP at pH 7.5…….96

Figure 32 Dual mode cyclic voltammogram for 1 mM PAP in a phosphate buffer at pH 7.5 with varied collecting electrode potential…….. 99

Figure 33 Calibration curves of PAP with single mode, dual mode at the generator, and dual mode at the collector ……..101

Figure 34 Enzyme reactions of alkaline phosphate (ALP) and β-galactosidase (β-Gal) generating PAP……..103

Figure 35 Analytical concept of the electrochemical immunoassay with β-galactosidase …….……. 104

Figure 36 Fluorescence spectrum of 4-MU produced by enzyme reaction of β-Gal ……...……...……107

Figure 37 Saturation curve of enzyme binding by the fluorescence measurement. ……... 108

Figure 38 Saturation curve from the experiment with a rotating disk electrode… 110

Figure 39 Experimental setup for immunoassay with a coplanar IDA electrode.. 114

Figure 40 Current vs. time for varied number of beads with coplanar IDA electrode ……117

Figure 41 Chronoamperometry with mouse IgG standards……... 120

Figure 42 Experimental setup for immunoassay with a comb IDA electrode…… 123

Figure 43 Comparison of coplanar and comb IDA electrodes in terms of response time and sensitivity…… 126

Figure 44 Response vs. number of beads with comb IDA electrode……..127

Figure 45 A model for paramagnetic beads in a magnetic and flow field……. 134

Figure 46 Vertical monement, z(t), of M-280 Dyna beads after they enter the magnetic field of a disk permanent magnet (1250 Gauss) …… 137

Figure 47 The velocity profile of fully developed laminar flow (100 μL/min) in the microfluidic channel (500 μm × 300 μm)……138

Figure 48 The distribution of magnetic beads in x direction settled on the bottom of the cannel in the uniform field model…… 139

Figure 49 Microchannel on the permanent magnet and captured magnetic beads. ……146

Figure 50 The collecting efficiency of magnetic beads for different flow rate….. 148

Figure 51 The microchannel and plaform for the assembly with an IDA chip and a magnet…… 151

Figure 52 Stabilization time of redox cycling current in a fluidic channel…… 158

Figure 53 Schematic of the bead-based immunoassay for bacteriophage MS2…. 160

Figure 54 Experimental setup for IDA sensor in a fluidic channel…… 163

Figure 55 Response of IDA electrode integrated in a microchannel to enzyme saturated microbeads……..…… 166

Figure 56 MS2 assay with RDE…….168

Figure 57 Amperogram for the 100 ng/mL MS2 sample detected in the PDMS channel at an IDA electrode…….. 171

Figure 58 Current vs. time plots for the following MS2 concentrations detected in the PDMS channel at an IDA electrode……. 172

Figure 59 Calibration curve for MS2 with IDA sensor in a fluidic channel……...173

SUMMARY

This research is directed towards developing a more sensitive and rapid electrochemical sensor for enzyme labeled immunoassays by coupling redox cycling at interdigitated electrode arrays (IDA) with the enzyme label β-galactosidase. Coplanar and comb IDA electrodes with a 2.5 μm gap were fabricated and their redox cycling currents were measured. ANSYS was used to model steady state currents for electrodes with different geometries. Comb IDA electrodes enhanced the signal about 3 times more than the coplanar IDAs, which agreed with the results of the simulation. Magnetic microbead-based enzyme assay, as a typical example of biochemical detection, was done using the comb and coplanar IDAs. The enzymes could be placed close to the sensing electrodes (~10 μm for the comb IDAs) and detection took less than 1 min with a limit of detection of 70 amole of β-galactosidase. We conclude that faster and more sensitive assays can be achieved with the comb IDA.

A paramagnetic bead assay has also been demonstrated for detection of bacteriophage MS2, used as a simulant for biothreat viruses, such as small pox. The immunoassay was carried out in a microfluidic format with the IDA, reference and counter electrodes integrated on the same chip. Detection of 90 ng/mL MS2 or $1.5x10^{10}$ MS2 particles/mL was demonstrated.

Chapter 1 and 2 was assigned to the introduction and background of the research topic. Fabrication processes for 3 versions of IDA electrodes were described in chapter 3 and the IDA electrodes were characterized in chapter 4. In chapter 5, bead-based immunoassays demonstrated with an IDA electrode and coplanar and

comb IDA electrodes were compared. Next two chapters were dedicated to the integration IDA sensors in a fluidic format. Collecting efficiency of magnetic beads investigated with simulation and compared with an experimental result. The fluidic system for immunoassay was fabricated and applied to a viral detection.

1. INTRODUCTION

1.1 Motivations for the Electrochemical Enzyme Assay with IDA Electrodes

The need for sensitive and compact detection systems for toxins and biological warfare agents has recently become critical due to the threat of bioterrorism. Electrochemical detection generally requires only simple hazardous and inexpensive reagents and electrodes are practical for miniaturization based on microfabrication technology. Interdigitated array (IDA) microelectrodes are particularly interesting because geometric differences from conventional electrodes result in a redox cycling which enhances the current in a stationary solution [1](figure 1). Since each microband electrode in the IDA can be potentiated separately, an electroactive species generated at one microband electrode (generator) diffuses across a narrow gap and a reverse reaction take place at a second electrode (collector).

For a successful utilization of redox cycling in an electrochemical detection, the analytes need to be electrochemically reversible molecules. IDA electrodes has been applied to direct detection of several specific biomolecules such as catecholamine[2] and dopamine[3, 4]. However, they were suffered from the poor reversibility and a fair amount of interferants. An enzyme label converting an electro-inactive substrate into an electroactive product makes the electrochemical detection more versatile and with improved signal enhancement[5, 6]. In this case, enzymes also amplify the signal as one enzyme can produce many detectable molecules. This thesis concerns optimization of IDA electrodes for the successful coupling of redox cycling and enzyme-labeled assay.

Interferance could be avoided using paramagnetic beads both as a mobile solid phase on which the enzymes are immobilized and carrier of target analytes which can be collected at a desired position[7]. Magnetic force could easily separate the analytes from the other interfering elements and address into subsequent procedures such as incubation, cleaning and detection[8]. The concept of magnetic bead-based microfluidic detection system was successfully demonstrated by Ahn et.al. This study covers the modification of IDA structure to improve the redox cycling for the bead-based enzyme labeled assay. The behavior of paramagnetic beads in the magnetic collector was also investigated to achieve maximum response at the IDA electrode.

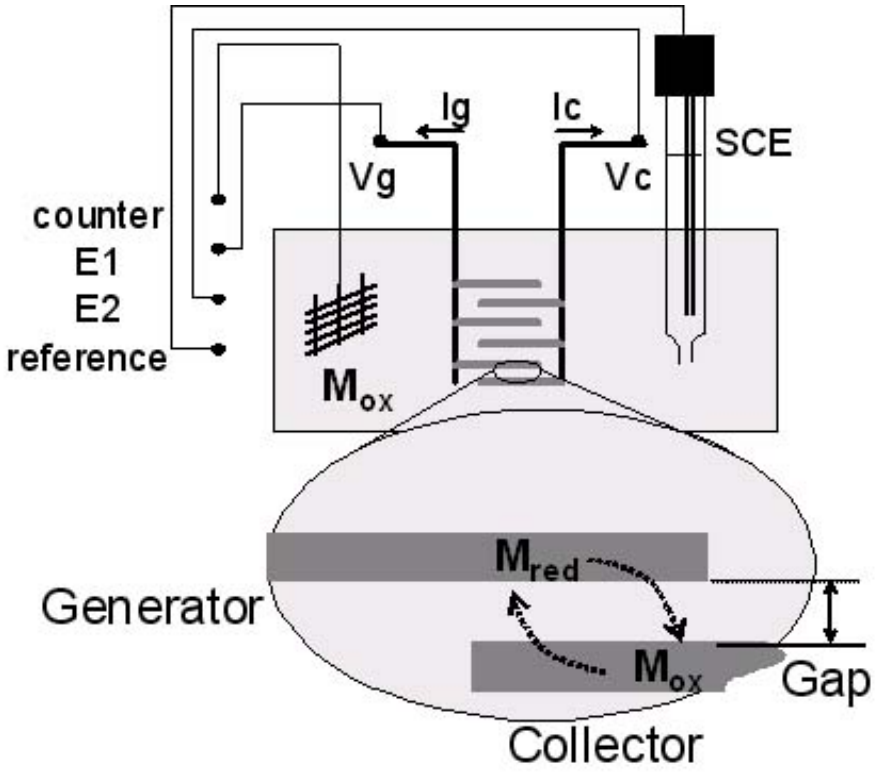

Figure 1. Conceptual diagram of redox cycling on an IDA electrode. Electrochemically reversible molecule, Mre, is generated from Mox and reverted reaching the collector

2 BACKGROUND

2.1 Redox Cycling on IDA Electrodes

Various detection methods have been applied to toxins, bacteria and viruses using either a fluorescent, radioactive or an electrochemical reagent. Electrochemistry offers advantages since it is unaffected by turbidity of the analyte solution and its simple instrumentation can be miniaturized to provide convenient detection in small volume. However, relatively low sensitivity of electrochemical detection limited its application to general biomolecular assays.

One of the most attractive aspects of IDA electrodes is the redox cycling arising from the close proximity of the electrodes. The IDA is made of two pairs of working electrodes consisting of parallel strips of metal fingers that are interdigitated and separated by insulating materials. The magnitude of the current in the dual mode with 1 μm gap is 50 times higher than that in the conventional chronoamperometry[9]. In an IDA with gap of 10 μm or smaller, the collecting efficiency is more than 90 % which means most of the species generated at one electrode are collected at the other.

The current was calculated on the basis of a twin electrode at coplanar geometric separation. The diffusion controlled limiting current at the coplanar IDA electrodes could be expressed[10]

$$|I_{lim}| = mbn\mathrm{FcD}[0.637\ln\{2.25(1+\mathrm{Wa/Wg})\} - 0.19/(1+\mathrm{Wa/Wg})^2]$$

where *m* is a number of band electrode pairs, *n* is the number of electrons, *b* is the band length, Wa is the band width, Wg is the gap, c is the concentration of the electroactive species, D is the diffusion coefficient, and F is Faraday's constant.

An IDA electrode with high collection efficiency is more effective for measuring small volume samples. When a single electrode is used for measuring small volume samples, the analyte is consumed by the electrochemical reaction. Then, the bulk concentration of an analyte decreases in a short time. In contrast, the concentration of the analyte in the sample changes very slowly when the IDA is used because the redox cycling regenerates the analyte. Voltammograms for 0.2~0.5 μl samples have been obtained with a low detection limit[11]

2.2 General Equation for a Diffusion Limited Current

The electrochemical system treated here is a reversible or quasi-reversible reaction

$$Ox + ne^- \leftrightarrow Red$$

where the potentials of the cathode and anode are sufficiently negative and positive, respectively, to effect reduction and oxidation and each electrode is non-polarizable. Thus, the current is limited only by the mass transfer in the solution. The mass transfer occurs by diffusion, migration, and convection. The current of redox cycling is measured in a stationary solution, convection is generally excluded. Migration effect is compensated with a high concentration of electrolyte in a buffer solution. Therefore, diffusion is the only mass transfer method which describes reaction rates on electrodes with various geometric structures.

Fick's laws are differential equations accounting for the flux of a substance and its concentration as functions of time and position. Fick's first law states that the flux is proportional to the concentration gradient $\partial C_o/\partial x$

$$-J(x,t) = D\frac{\partial C(x,t)}{\partial x}$$

Fick's second law is derived from the first law pertaining to the change in concentration of a species (M) with time. Since the variation in the diffusion coefficient can be neglected, the general formulation of Fick's second law for any geometry is

$$\frac{\partial C}{\partial t} = D\nabla^2 C$$

where ∇^2 is the Laplacian operator. Form of ∇^2 for band electrodes is

$$\frac{\partial^2}{\partial x^2} + \frac{\partial^2}{\partial y^2}$$

in 2-D model where x is the distance in the plane of the band and y is the distance normal to the band surface. An IDA electrode is an example of this model when the edge effect is ignored.

2.3 Model of Redox Current on IDA Electrodes

If we ignore the edge effect by assuming that the IDA has many legs and the length of the legs are much longer than the width, then the concentrations of the reduced and oxidized species are subject to the 2-D diffusion equation under steady state conditions (figure 2).

$$\frac{\partial C}{\partial t} = D(\frac{\partial^2 C}{\partial x^2} + \frac{\partial^2 C}{\partial y^2}) = 0$$

Since the molecular weights of the reduced (Red) and the oxidized (Ox) forms are very close, the diffusion coefficients of the two forms of the analyte are assumed to be the same. Then, the sum of oxidized and reduced forms is constant over the diffusion space and is equal to the sum of the bulk concentration (C_{Bulk}), which leads to the result that the concentration profiles of the reduced ($C_R(x,y,t)$) and the oxidized ($C_O(x,y,t)$) forms are symmetrical across the y-axis[12].

$C_R(x,y,t) + C_O(x,y,t) = C_{Bulk}$.....(*)

The solution of the above equation requires one initial condition and two boundary conditions for each diffusing species.

(a) Initial conditions

If the bulk solution contains only oxidized form at the start of the experiment, the initial condition is

$C_O(x,y,0) = C_{Bulk}$, $C_R(x,y,0) = 0$

(b) Semi-infinite boundary conditions

The electrochemical cell is large compared to the length of diffusion and each

form is recycled on IDA electrodes; hence the solution far from the electrodes is not altered by the process. The concentration reaches the initial value, so that

$$C_O\,(x,y,t) = C_{Bulk}\,, C_R\,(x,y,t) = 0 \qquad \text{for } x \to \infty$$

(c) Electrode surfce boundary conditions

Additional boundary conditions relate to concentration gradientsat the electrode surface. In a diffusion-limiting condition, the charge transfer reaction occurs at the moment of molecule's arrival at the electrode surface. Thus, Co at cathode and C_R at anode are zero where Co at anode and C_R at cathode are C_{Bulk} accoding to the equation(*).

$$C_O\,(\text{anode}) = C_{Bulk},\ C_O\,(\text{cathode}) = 0$$

$$C_R\,(\text{anode}) = 0,\ C_R\,(\text{cathode}) = C_{Bulk}$$

The effect of electrode geometry on the redox cycling current can be simulated with finite element method (FEM). The diffusion model above is identical to the conduction model in heat transfer. The equation was solved with the heat conduction model in ANSYS. The coplanar and comb structures are looked into as representative examples. Figure 2 illustrates simplified structures in rectangular unit cells and the results.

The flux profiles shown in Figure 2 indicate the flux of oxidized species, where the arrows are color coded as indicated. Arrows indicate the direction of chemical transport at each node. Here the diffusion pathways for coplanar electrode can be visualized and are clearly elliptical, whereas much of the diffusion pathways are straight lines for the comb-electrode geometry. Thus, the practical distance for diffusion becomes shorter for the comb geometry compared to the planar electrode, and hence the geometry

improves the efficiency of the redox cycling. The flux at the electrode surface represents current density. Both electrodes demonstrate a concentration of flux at the edge of the electrode and this effect is more distinct in the coplanar structure since the diffusion distance is minimum at the edges. At the center of electrodes, the flux of comb structure is higher (bluish green) than the coplanar one (light blue), which illustrates more distributed current through the surface of electrodes. The current will be calculated and compared with experimental value later in chapter 4.

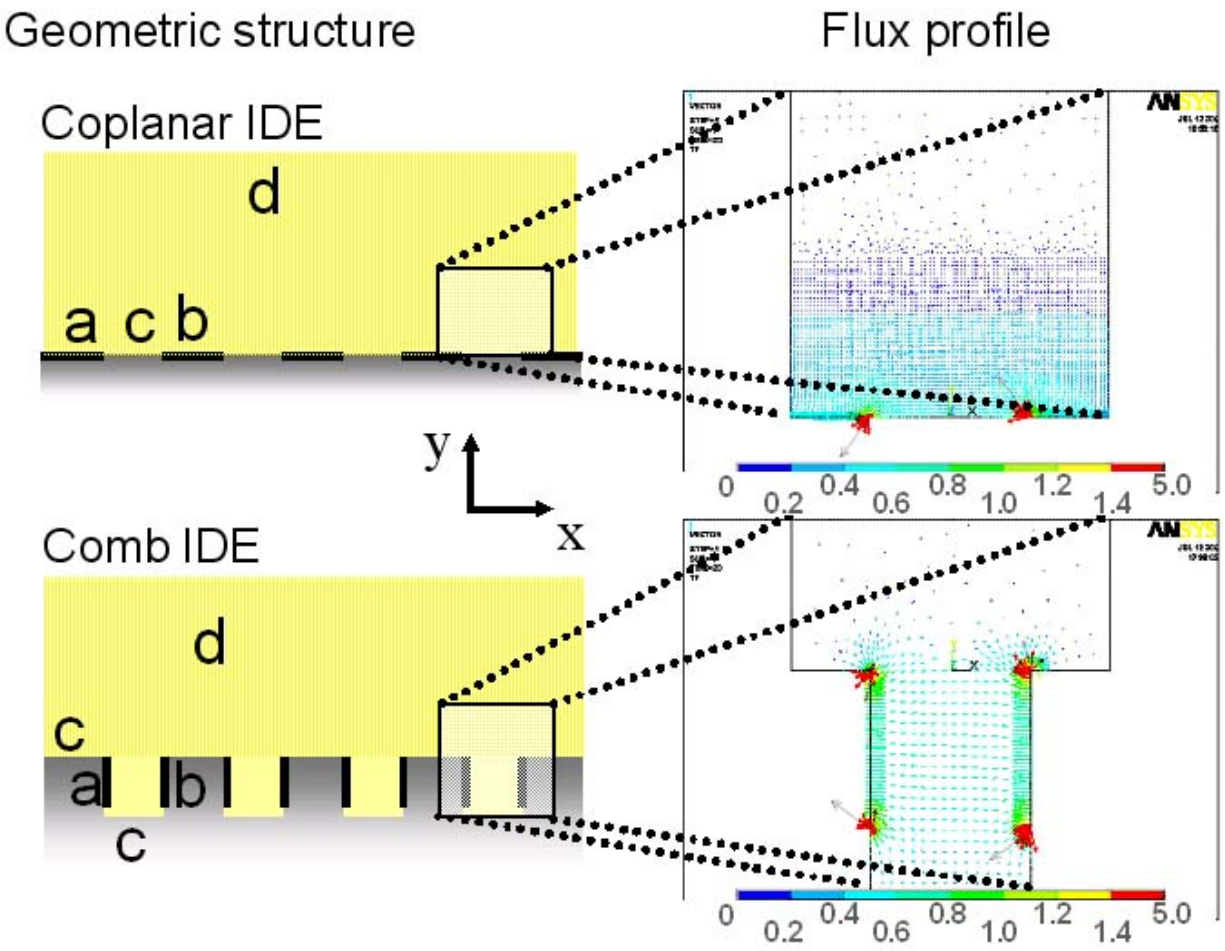

Figure 2. Models for coplanar and comb IDA electrodes and resulted flux. a, anode; b, cathode; c, insulated region; d, bulk solution.

2.4 Fabrication Methods of IDA Electrodes

Since IDA electrodes with smaller gap are more effective for electroanalysis, most of microfabrication technologies such as photolithography, thin film deposition and dry etching have been used to fabricate microarray electrodes[13]. Metal films have been widely used to fabricate IDA electrodes because they can be easily deposited on a substrate as a thin uniform film with fine patterns. They were generally deposited by sputtering or evaporation. Some non-metallic electrodes were built by sputtering or chemical vapor deposition.

2.4.1 Directionality of Metal Deposition with an Evaporator

Evaporation is an ultrahigh vacuum technique for the deposition of thin films. Generally, the chamber has a background pressure at 10^{-7}~10^{-6} Torr, and the metal to be evaporated is heated in a crucible. The vapor of the metal travels in a straight line to the substrates due to its long mean free path. Figure 3 shows a schematic of the geometry of a film evaporated over a step[14]. Over the scale of 1 μm, the incoming material beam can be considered nondivergent. When the incident atoms are immobile on the surface of the wafer, the topology will cast well defined shadows leaving the film discontinuous in the trench.

The poor step coverage was considered as a problem of evaporation in the IC fabrication process whereas sputtering forms a conformal layer. However, this character was utilized to build sub-micro scaled interdigitated electrodes[15,16]. Shallow trenches and hills are first made on the substrate and the substrate was fixed at an angle during the deposition. Then, the shadow kept the two electrodes separated. We deployed tilted evaporation to build IDA electrodes on trenches which improve redox cycling.

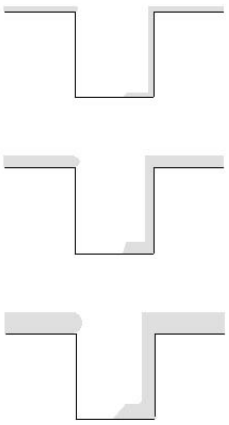

Figure 3. Time evolution of the evaporative coating of a feature with aspect ratio of 1.0, with little surface atom mobility and no rotation of substrate

2.4.2 Carbon Electrodes

For an effective redox cycling, the reaction on the electrodes needs to be reversible. However, lots of biomolecules experience non-reversible reaction and contaminate surface of electrodes. Conductive carbon film was tried for electroanalysis due to minimum surface contamination. Catecholamin was successfully detected with high collection efficiency on a carbon electrode, where carbon was pyrolytically deposited and etched with O_2 plasma[2]. Another advantage of carbon electrodes over metallic electrodes is a wider potential window particularly in the cathodic potential region resulting from the substantial overpotential of the hydrogen and oxygen reduction. Reduction of ruthenium hexamine was measured in the nanomole region which could not be observed at a Pt electrode due to a high background current[17].

Despite the clear benefit of carbon as an electrode material, carbon electrodes are still not prevailing due to difficulties in the fabrication. Since the adhesion of sputter- or chemical vapor-deposited carbon film to the substrate is poor, it is easily stripped off during the microfabrication process. The smallest gap realized is 2 μm so far and its electrochemical properties are still under basic tests[18]. The low conductivity of carbon films is also a problem because it causes a significant iR drop after microfabrication. Many researchers are actively working on simpler and more compatible process for highly conductive carbon electrodes.

2.5 Electrochemical Immunoassay

As redox cycling enhances current in electroanalysis, enzyme reaction is a very effective signal enhancement in biological systems. The redox cycling and enzyme reaction can be coupled if the enzyme label on the target analyte converts electrochemically inactive substrates into electrochemically active products.

Enzyme labeling is one of the most popular methods in immunoassay systems. Immunoassay is a very specific technique based on the exceptional specificity that an antibody has for its target antigen. Immunological detection has been proved successful for viruses as well as for toxins, bacteria, and spores, the other classes of bioterrorism agents, but improvements are needed for more sensitive and miniaturized assays[19]. Miniaturization affects portability as well as reducing the sample volume required for an immunoassay. For example, both neonatal and geriatric patients may have very little blood to give towards diagnostics and benefit from micro-volume analysis. Ultra-sensitive immunoassays can also help the diagnosis of diseases in earlier stages than is currently possible[20].

2.5.1 Sandwich Immunoassay

Immunoassays can be categorized into homogeneous and heterogeneous methods. Homogeneous methods do not include a step to separate bound antigen from free antigen. Heterogeneous methods, which have a separation step, result in substantially better limit of detection. Sandwich immunoassay is a type of heterogeneous immunoassay.

In a sandwich immunoassay, reagents other than the antigen are present in excess to drive the reactions to completion. The primary antibody is bound to a solid support, and the blocker protects free surface from nonspecific binding. The sample solution is added and the antigen is extracted from a sample upon binding to this antibody. Then, a labeled secondary antibody completes the immunoassay sandwich by recognizing a site on the antigen different from the primary antibody-binding site (figure 4). Labels on the secondary antibody include radiolabels, metal labels, optically active labels, and enzyme labels. Unlike other labels, enzymes amplify the signal as one enzyme can produce many detectable molecules. UV-visible absorbance, fluorescence, chemiluminescense, and electrochemistry are commonly used detection methods.

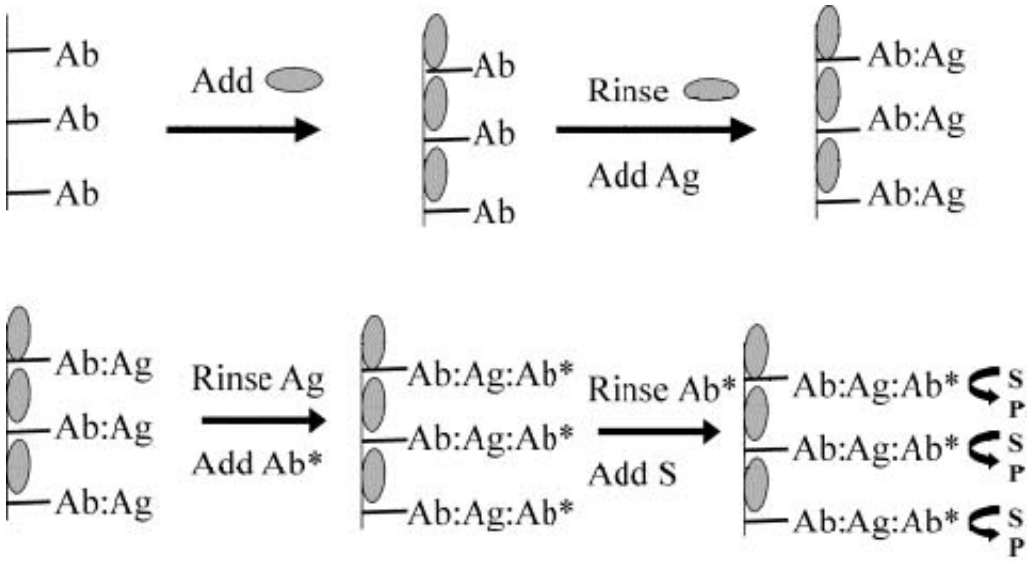

Figure 4. Enzyme labeled sandwich immunoassay. Ab, antibody; Ag, antigen; Ab*, enzyme-labeled secondary antibody; P, product; S, substrate; , blocker.

2.5.2 4-Aminophenol as a Reversible Analyte.

Alkaline phosphatase(ALP) is one of the most common enzyme label and is well-characterized in many ways. ALP hydrolyzes orthophosphate from a wide variety of phosphate esters under alkaline conditions[21]. The first substrate/product system used for electrochemical detection was phenyl phosphate/phenol[5]. Phenol is detected by oxidation at about 870 mV vs. Ag/AgCl, a potential at which the substrate is not oxidized. Although this system demonstrated an example of enzyme labeled electrochemical immunoassay, electrochemical detection of phenol was found to have three disadvantages. High concentrations of phenol from polymerization of its radical oxidation products foul the electrode surface, so assay conditions need to be carefully controlled to limit phenol production. Relatively high oxidation potential compromised detection limits for certain detection methods and the reaction was irreversible.

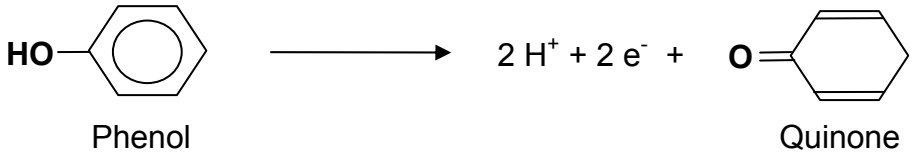

E° = 870 mV vs. Ag/AgCl

4-Aminophenyl phosphate (PAPP)/4-aminophenol (PAP) circumvented the problems of phenol oxidation[22]. The product, PAP, is electrochemically reversible, has an oxidation potential of 275 mV versus Ag/AgCl and shows no significant electrode fouling at glassy carbon electrode. However, drawbacks of this substrate/product couple are the decomposition of PAPP in alkaline solution and the susceptibility of PAP to air oxidation. Thus, the time of linear accumulation of product is limited. To alleviate this

problem, deaerated buffer was tried[23] and buffer condition was optimized[24] in other researches.

.

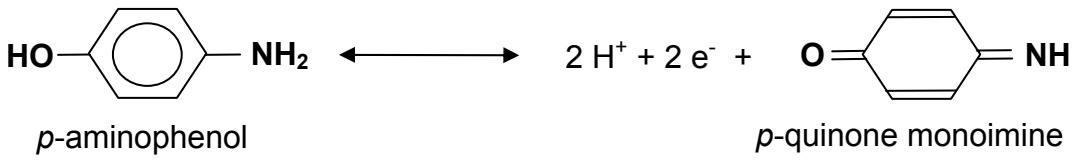

E° = 275 mV vs. Ag/AgCl

Electrochemical reversibility of PAP enabled to couple the enzyme labeling and more effective redox cycling for immunoassays[22]. Hence, PAP-generating enzymes such as ALP were widely used in electrochemical immunoassays with IDA electrodes where the signal was enhanced by enzyme reaction and redox cycling simultaneously.

2.5.3 Paramagnetic Beads as a Solid Phase

In many electrochemical biosensors, enzymes or antibodies are immobilized on the electrode by various surface-coating methods[25,26,27], and the longevity of the sensor is limited by the stability of the immobilized biomolecules. Redox cycling couples are affected by any kind of surface coating on the electrodes that retards the transportation of reduced or oxidized products to the opposite electrode and decreases the signal enhancement[4]. If, however, the biomolecules are immobilized on paramagnetic microbeads, then the enzymes can be positioned near electrodes, minimizing reagent diffusion distances without blocking the surface of the electrodes[28]. Also, microbeads can be collected in small volumes, which reduce the dilution of the electroactive enzyme product. Figure 5 shows the process of magnetic bead-based immunoassay[29].

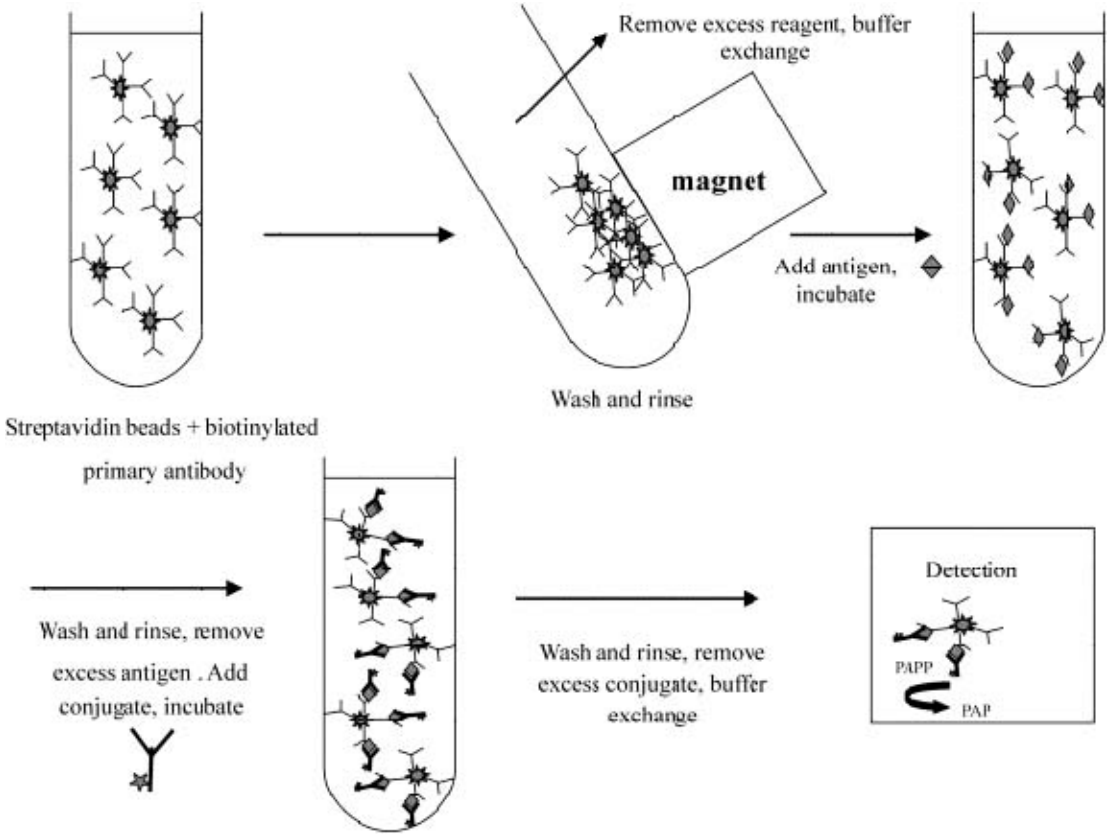

Figure 5. Procedure of Immunoassay with paramagnetic beads as a solid phase

2.6 Magnetic Collector in a Microfluidic System

A magnetic particle with a known species attached to it can be thought of as a micro container compared to the microtiter plate. However, magnetic actuation can move these species in a controlled way since the beads are mobile. Immunoassays on a single particle were carried out with specially designed fluorometers but it required well-experienced manpower since all the procedure need manual handling[30,31]. To get the utmost out of the magnetic bead as a mobile solid phase, the processes in figure 4 could be integrated on a Si-based microsystem[8]. This proof-of concept device contained various microfluidic components and the magnetic collector (or biofilter) and electrochemical sensor was considered as key components.

2.6.1 Superparamagnetic Microbeads: Dynabeads

The monosized, magnetizable polymer particles were prepared from monosized macroporous particles which are magnetized by an in situ formation of ferromagnetic material inside the pores. The macroporous particles are prepared by the activated swelling method[32]. Figure 6 shows the uniform sizes of the prepared magnetic particles intended to be 2.8 μm. $-NO_2$ groups are covalently coupled to the surface inside the pores of the particles and make the particles hydrophilic. When these particles are dispersed in an aqueous solution of Fe^{2+} salt, Fe^{2+} reacts with groups to iron hydroxides which precipitate inside the pores. Upon heating, small grains are evenly distributed through the pore volume of the particle.

$$-NO_2 + 6\ Fe(OH)_2 \rightarrow -NH_2 + 3\ \gamma Fe_2O_3 + 5\ H_2O$$

The iron is mainly present as γFe_2O_3 (maghemite) which may be considered as a fully oxidized magnetite (Fe_3O_4). Maghemite is almost as magnetic as magnetite, the saturation magnetizations at 20°C being 76 and 92 emu/g respectively. The magnetization curve of the particle shows no hysteresis, accordingly both retentivity and coercivity are zero. This behavior can be explained in terms of superparamagnetism[7].

Superparamagnetism is a phenomenon by which magnetic materials may exhibit a behavior similar to paramagnetism at temperatures below the Curie temperature[33]. Superparamagnetism occurs when the material is composed of very small crystallites (1-10 nm) such as the small grains of magnetic oxide within the polymer particles. In this case even though the temperature is below the Curie temperature and the thermal energy

is not sufficient to overcome the coupling forces between neighboring atoms, the thermal energy is sufficient to change the direction of magnetization of the entire crystallite. The resulting fluctuations in the direction of magnetization cause the magnetic field to average to zero. Because there is no longer any magnetic order, the material exhibits paramagnetic behavior. Paramagnetic materials attract and repel like normal magnets when subject to a magnetic field. However, the material exibits no permanent magnetization remained after the particles have been subject to an external magnetic field, which conforms with no hysteresis in the magnetization curve of the particle.

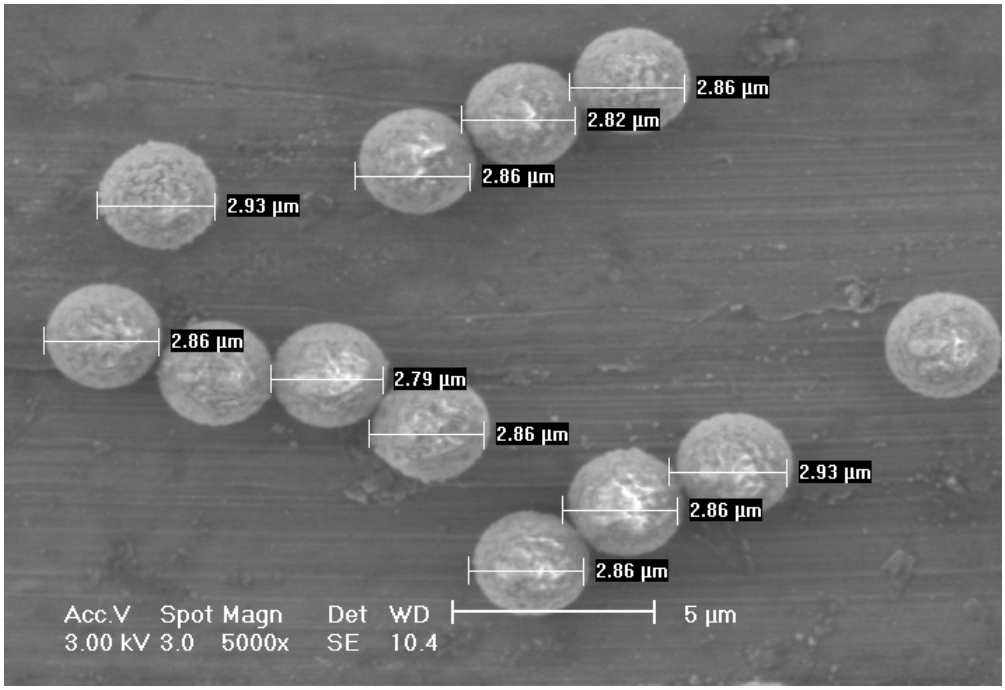

Figure 6. Dynabeads M-280; superparamagnetic beads with diameter of 2.8 µm

2.6.2 Permanent Magnet vs. Electromagnet

The paramagnetic beads are manipulated using magnetic field and fluid stream. The magnetic field can be generated with either a permanent magnet or a electromagnet. Electromagnet is depoloyed to generic microfluidic systems because it can be built inlaid with other bioMEMS components through microfabrication technologies. Planar inductors are encapsulated with electroplated permalloy to direct the magnetic flux path[34]. Thus, the electromagnet can be located very close to the microchannel (tens of μm) and the magnetic field strength is adjustible. However, stronger magnetic field can be built with a permanent magnet and various designs of microchannel can be tested since the microchannels are made separately from the magnet and assembled later.

Analytical solutions for the magnetic flux were found for electromagnets with simple structures but the microfabricated electromagnets have fairly complex structures and are simulate with numerical methods. The magnetic flux of permanent magnets can also be calculated with numerical methods. However, simple structure of permanent magnets can be equated to electromagnets with similar structure and the analytical solution is acquired. If the magnetic field is well-formulated, the behavior of magnetic particles can be easily predicted from a simple model. For example, a disk-shaped permanent magnet can be considered as a 1-turn coil which have the same diameter (r) and equivalent current (Ieq) flows through (figure 7). The magnetic flux density around the z-axis is expressed as

$$B(z) = (\mu_o I_{eq} r^2)/2(r^2+z^2)^{3/2}$$

where μ_o is the permeability of free space, I_{eq} is the equivalent current, and r is the diameter of the magnet. On the basis of this approximation, we could calculate the strength of the magnetic force on the paramagnetic beads.

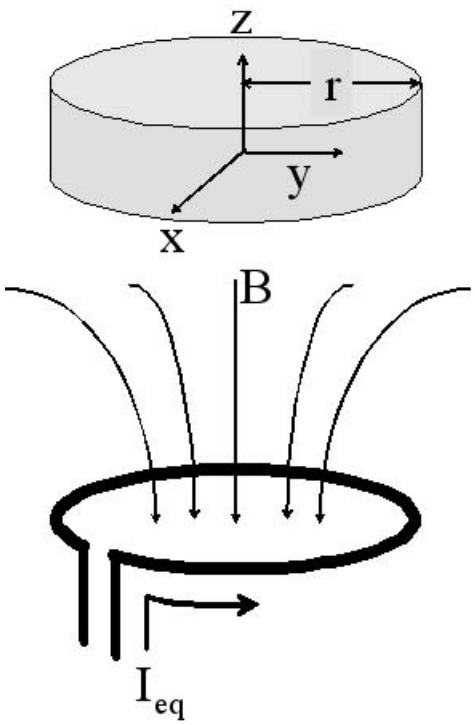

Figure 7. An equivalent electromagnet for a disk-shaped permanent magnet. B, magnetic flux; Ieq, equivalent current; r, radius of the magnet

2.7 Fluid Flow in a Microchannel

Flow field dictates the movement of microbeads in a microchannel. It is indispensable to understand the microscopic behavior of fluid to control the microbeads. The equation of motion for an incompressible Newtonian fluid can be expressed as follows when the viscous effect is considered.

$$\rho\left(\frac{\partial u}{\partial t}+u\frac{\partial u}{\partial x}+v\frac{\partial u}{\partial y}+w\frac{\partial u}{\partial z}\right)=-\frac{\partial P}{\partial x}+\rho g_x+\mu\left(\frac{\partial^2 u}{\partial x^2}+\frac{\partial^2 u}{\partial y^2}+\frac{\partial^2 u}{\partial z^2}\right) \quad \text{(x- direction)}$$

$$\rho\left(\frac{\partial v}{\partial t}+u\frac{\partial v}{\partial x}+v\frac{\partial v}{\partial y}+w\frac{\partial v}{\partial z}\right)=-\frac{\partial P}{\partial y}+\rho g_y+\mu\left(\frac{\partial^2 v}{\partial x^2}+\frac{\partial^2 v}{\partial y^2}+\frac{\partial^2 v}{\partial z^2}\right) \quad \text{(y- direction)}$$

$$\rho\left(\frac{\partial w}{\partial t}+u\frac{\partial w}{\partial x}+v\frac{\partial w}{\partial y}+w\frac{\partial w}{\partial z}\right)=-\frac{\partial P}{\partial z}+\rho g_z+\mu\left(\frac{\partial^2 w}{\partial x^2}+\frac{\partial^2 w}{\partial y^2}+\frac{\partial^2 w}{\partial z^2}\right) \quad \text{(z- direction)}$$

where ρ is density, P pressure, μ dynamic viscosity,

g_x, g_y, *and* g_z, *are the acceleration of gravity in* x, y, and z directions respectively.

u, v, and w are the velocity components in x, y, and z directions respectively.

The left sides of the equations represent the acceleration terms and the right sides the force terms. These equations are commonly called 'Navier-Stokes equations' and provide a complete mathematical description of the flow of incompressible Newtonian fluids when combined with the conservation of mass equation shown below.

$$\frac{\partial \rho}{\partial t}+\frac{\partial(\rho u)}{\partial x}+\frac{\partial(\rho v)}{\partial y}+\frac{\partial(\rho w)}{\partial z}=0$$

A principal difficulty in solving 'Navier-Stokes equations' arises from the non-linearity of the convective acceleration terms (i.e., $u\cdot\partial u/\partial x$, etc…). For most practical flow problems, fluid particles do have accelerated motion as they move in the flow field. However, there are a few cases for which the convective acceleration vanishes because of the nature of the geometry of the flow system. In these cases, exact solutions are possible.

Case 1: Fixed parallel plates

If we assume a steady laminar flow through fixed parallel plates, the volumetric flow rate per unit length of width can be obtained as follows by solving the above Navier-Stokes equation.

$$Q = \frac{2h^3}{3\mu}\left(-\frac{dP}{dx}\right) = \frac{2h^3}{3\mu}\cdot\frac{(P_o - P_i)}{L}$$

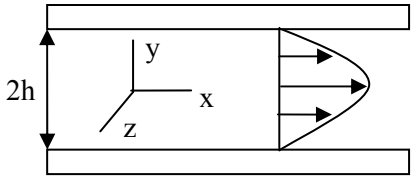

where Q is volumetric flow rate, μ is viscosity, $2h$ is the gap between the plates, L is the length of the plates, and P_i, P_o are the inlet, outlet pressure.

Flow rate strongly depends on the gap between the plates. The average flow velocity $\bar{u}$ and flow velocity distribution $u(r)$ can also be obtained as follows.

$$\bar{u} = \frac{h^2}{3\mu}\cdot\frac{(P_o - P_i)}{L} = \frac{3}{2}\cdot u_{\max}$$

$$u(y) = \frac{(P_o - P_i)}{2\mu L}\cdot(y^2 - h^2)$$

Case 2: Circular tube

Now lets consider a fluid flow through a straight circular tube whose radius is r_o. The flow rate vs. pressure drop relationship for incompressible, laminar, fully developed flow can be obtained as follows.

$$Q = \frac{\pi r_o^4}{8\mu}\left(-\frac{dP}{dx}\right) = \frac{\pi r_o^4}{8\mu}\cdot\frac{(P_o - P_i)}{L} = \frac{\pi d^4}{128\mu}\cdot\frac{(P_o - P_i)}{L}$$

The average flow velocity $\bar{u}$ and flow velocity distribution $u(r)$ can also be obtained as follows.

$$\bar{u} = \frac{r_o^2}{8\mu}\left(-\frac{dP}{dx}\right) = \frac{r_o^2}{8\mu}\cdot\frac{(P_o - P_i)}{L} = \frac{1}{2}u_{\max}$$

$$u(r) = \frac{(r_o^2 - r^2)}{4\mu}(-\frac{dP}{dx}) = \frac{(r_o^2 - r^2)}{4\mu} \cdot \frac{(P_o - P_i)}{L}$$

Case 3: Rectangular tube

Most of microfabricated fluidic channels have rectangular cross-sections. The flow is determined by the width and height of the channel. This case will be described in chapter 6 with an example of a real microchannel.

The above equations are based on a steady flow without any disturbance on the velocity of the flow. In reality, all flows are unsteady especially when the channel changes in some way, such as a change in dimensions, or the fluid flows through a bend, valve, or some other components. The region of flow near the change is termed the entrance region where the calculation of the velocity profile is quite complex. However, once the fluid reaches the end of the entrance region, the velocity can be described by the above formula. The length of the entrance region is given by

$L_e = 0.06\ D_h Re$ (for laminar flow)

$L_e = 4.4\ D_h (Re)^{1/6}$ (for turbulent flow)

$$\text{Re} = \frac{\rho V D_h}{\mu}$$

where is hydraulic diameter of the channel, Re is Reynolds number, ρ is density of the fluid, μ is dynamic viscosity and V is the volume flow rate. For the better understanding of a magnetic collector, it must be located after the length of entrance in a microchannel.

2.8 Stereolithography: Design and Fabrication of Microchannel

Microchannels were defined on a chip through photolithography by deep-etch X-ray source, electroforming and molding (LIGA), high viscosity photosensitive polymers such as PDMS[35] or SU-8[36]. Then, one has to design and order a mask and optimize the process through trial and error every time a different design of the channel is tried. For experimental evaluation of microchannel, more flexible tool is preferred for the design and fabrication.

Stereolithography can easily fabricate small and 3-dimensional structures with customized design. Stereolithography is a layer based manufacturing process (figure 8). Physical prototypes are built by fabricating cross sectional contours or layers, one on top of another. Each layer is formed by tracing 2-D contour in a vat of photopolymer resin with a laser while the focused laser cures the resin halfway. Proper solvent and agitating tools clear the undrained resin from the undercured structure and final curing by heat or light gives the structure desired strength and stability. Minimum feature size is about 50 μm and virtually any 3-D structures are possible. Recently developed micro-SL system enabled fabrication of sub-micron features using a 2-photon photo-polymerization approach[37].

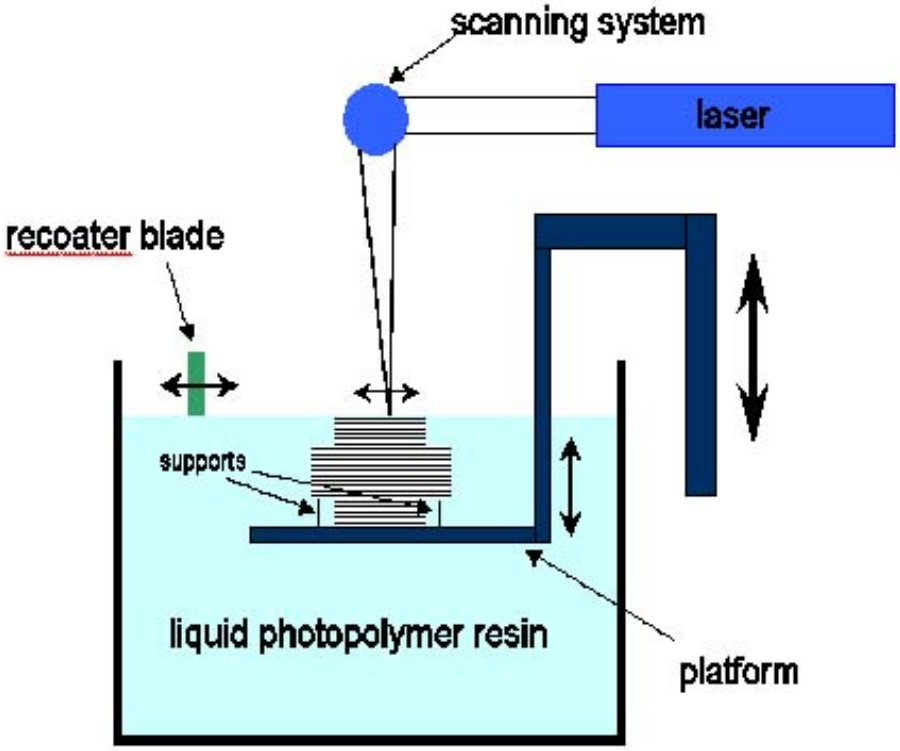

Figure 8. Schematic of SLA system. Arrows (↔) indicate the direction of movement.

3. FABRICATION OF IDA ELECTRODES

The IDA electrodes were built on p-type <100> 4” silicon wafers with the resistivity of 10 to 50 Ωcm. We have fabricated three different versions of IDA electrodes. First one was prevalent coplanar structure where the generating and collecting electrodes are on the same plane. Second design was a comb structure where the two electrodes are facing each other in a trench. Those two structures were compared in terms of redox cycling efficiency and advantage in magnetic bead-based assays. The last version was comb IDA electrodes built along with reference and auxiliary electrode on chip. The three electrode-integrated chip was designed to be used in a microfluidic system.

3.1 Fabrication of Coplanar IDA Electrodes

The basic fabrication process is depicted in Figure 9. Two 5-inch masks were used for the total fabrication. The finest features were fingers of IDA electrodes with gap of 2 μm and 3 μm in the first mask. The final gap between fingers was 1.6 μm and 2.4 μm as shown in figure 10.

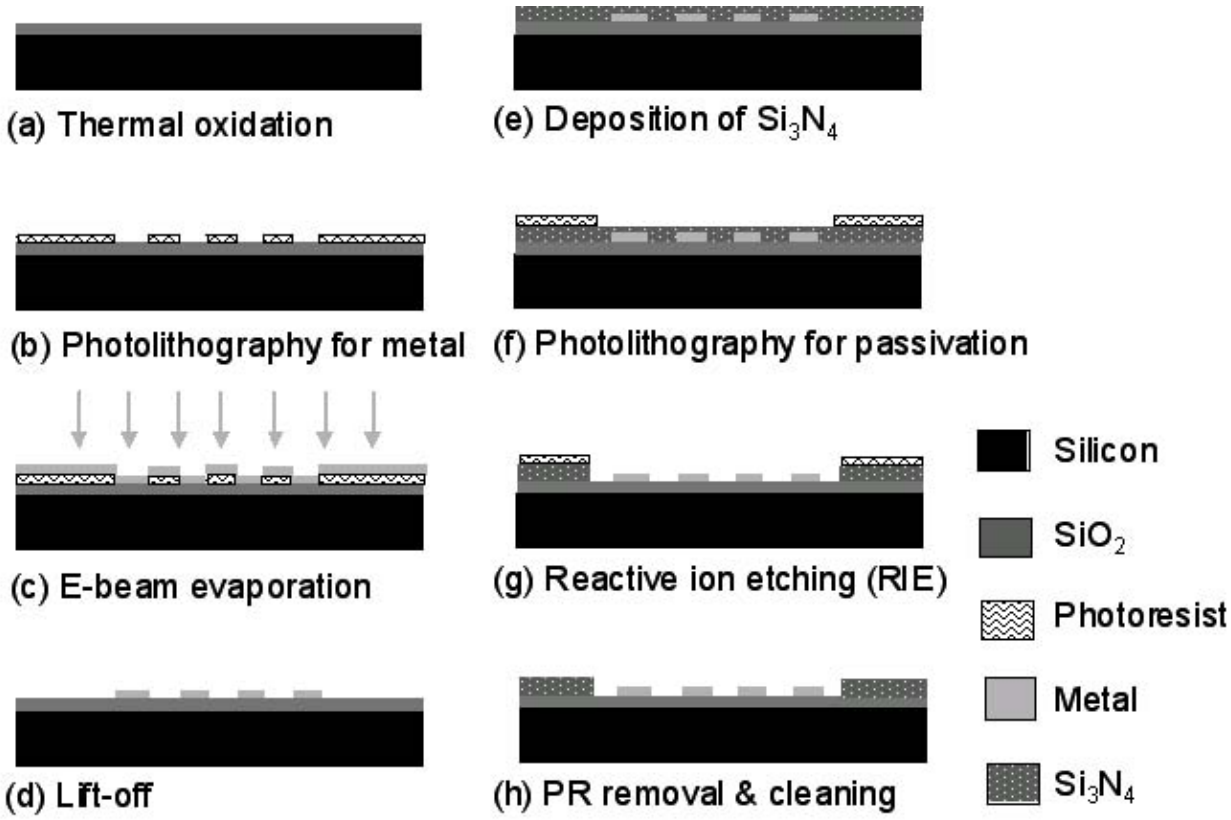

Figure 9. Fabrication process for coplanar IDA electrodes

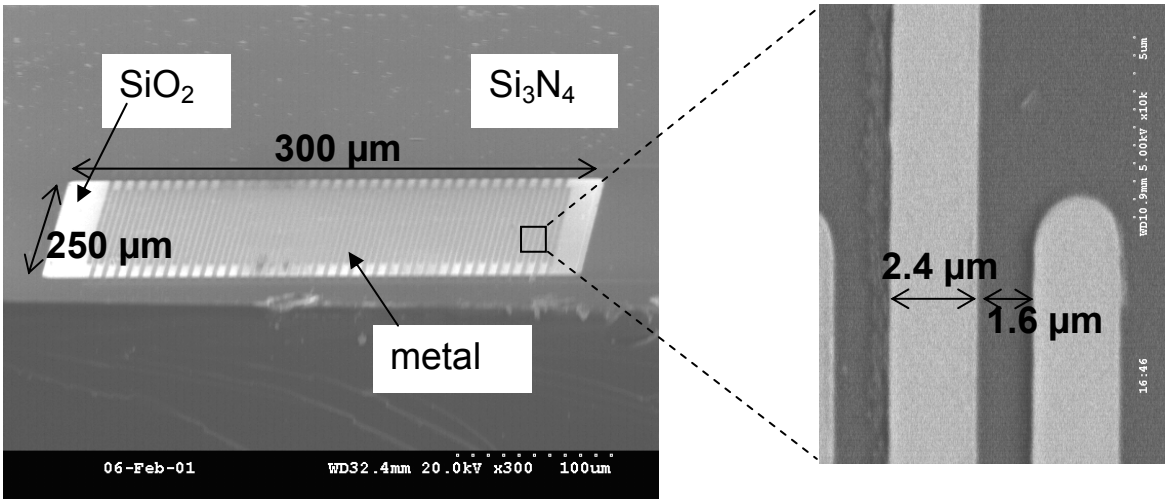

Figure 10. IDA electrode fabricated with a mask of 2 µm gap between fingers. The exact gap after final process was 1.6 µm.

3.1.1 Oxidation

Silicon dioxide layer is thermally grown to 0.5 μm in a dry ambient at 1150 °C in Lindberg furnace for 7 hours while O_2 flows at 5 L/min. Temperature is raised at 15 °C/min and cooled down by natural convection. This SiO_2 layer serves as an insulation layer between p-type silicon and the metal layers.

3.1.2 Photolithography

The mask is a 5 inch chrome mask. 2 photolithographic steps are the same; metal pattern and passivation layer (Si_3N_4) pattern.

(a) Photoresist spinning

For better adhesion of photoresist, wafers are baked on a hot plate at 150 °C for 3 minutes as a dehydration bake. Shipley 1813 photoresist, then was spun for 1 minute at 3000 rpm. Resulted thickness of photoresist is 1 μm.

(b) Pre-bake

Photoresist is prebaked on a hot plate for 1 minute at 100°C.

(c) Exposure

Photoresist was exposed to UV light using Karl Suss MA-6 mask aligner (Waterbay, CT) in a vacuum contact mode. Proper dose is 70 mJ/cm2 in constant intensity mode at CI-1 which was initially calibrated for 6mW/cm2 at 365nm.

(d) Developing

Photoresist is developed in 1:4 solution of Shipley Microposit 351 developer concentrate and DI water for 1 minute. Wafers are then rinsed with DI water, dried with nitrogen and inspected with microscope.

(e) Post-bake

Wafers were baked again on a hot plate at 120°C for 1 minute. It makes the defined features of photoresist hardened and preserved during the reactive ion etching (RIE). Before lift-off, this step is skipped since post-baked photoresist is dissolved in acetone slowly and makes lift-off defective.

3.1.3 Metal Deposition

Evaporation process is preferred for metal deposition on a planar structure due to the easiness of its lift-off. Faster lift-off of evaporate metal compared to a sputtered one owes to the characteristics of evaporation mentioned in chapter 2. Platinum and gold are used as materials for electrode.

The films occasionally peeled off the surface during the subsequent processes and exhibited poor adhesion to SiO_2. Therefore, evaporation needs to be carried out immediately after preceding photolithography to avoid potential contamination. Adhesion layer also helped to resolve the problem. The adhesion layer has to meet a few requirements. First, it has to be chemically inert with reagents used in the electrochemical detection of biological samples. Second, the layer has to be electrochemically inert under the experimental condition of detection. Thirdly, it has to be compatible with the fabrication procedure. Traditional metals such as chromium and titanium, therefore, were considered for this purpose because they both are well-known to adhere to SiO_2. Chromium was ruled out since it has high reactivity with liquids particularly when an electrical voltage is applied. In case of Ti, titanium oxide forms on the surface at room temperature which is good since it acts as a passivating layer and a chemically inert material[38]. Thus, titanium is used as the adhesion layer in this paper.

Platinum or gold for metal electrodes is deposited by electron-beam evaporation in CVC system at the base pressure equal to or lower than 3×10^{-7} Torr. A 50 angstrom Ti was deposited then 400 angstrom of platinum or gold is deposited. Both metal sources are soaked for 5 minutes before actual deposition to avoid cross-contamination. Deposition rate for titanium is 5 angstrom/second. Platinum and gold are deposited at 3

angstrom/second. Deposition rate and thickness are measured by frequency shift of a quartz crystal thickness monitor (Inficon XTC, from Leybold Inficon, East Syracuse, NY). The key limitation for the thickness of metal layer depends on subsequent lift-off process. Thicker deposition of platinum heats up the wafer above critical temperature and transforms underlying photoresist, which makes photoresist insoluble in acetone. Thus, a thermal mass is required for a thicker layer of platinum.

3.1.4 Lift-Off

After evaporation, wafers submerge in a beaker with acetone and with ultrasonic agitation for 1 min at room temperature. Acetone solution is changed accordingly to make sure there is not too much of metal flakes, already lifted off, which can adhere to the wafer and make shorts between two fingers of IDA electrode. Before the Si_3N_4 deposition, the wafers are cleaned with warm pirana solution (H_2O_2: H_2SO_4 = 3:7) for 1 minute to make sure that the entire organic layer is removed. Then the wafers are rinsed with flowing DI water for 1 minute and blow dried with nitrogen.

3.1.5 PECVD of Si_3N_4

To define the IDA electrode, the interconnecting metal between the IDAs and contact pads has to be unexposed. A layer of photopolymer such as photoresist is the simplest process since no etching step is required. However, those polymers are not compatible with the subsequent cleaning steps. Thus, we have to build inorganic layer which is tolerant to most cleaning.

The passivation layer can be built using plasma enhanced chemical vapor deposition (PECVD), which can grow dielectric layer at a high deposition rate. SiO_2 and Si_3N_4 are popular insulating layer used in microfabricaion technology. To avoid damage to the bottom layer, SiO_2, during the subsequent RIE, we selected Si_3N_4 as a top layer for passivation.

Silicon nitride layer is deposited up to 0.5 μm in the Plasma Them PECVD with a deposition rate of 700 angstrom/min. Gas flow rates are SiH4,200 SCCM; NH3, 5 SCCM, N2, 900 SCCM and average power is 300 W. The process goes under the pressure of 900 mTorr at 300 °C.

3.1.6 Reactive Ion Etching of Silicon Nitride Layer

The process condition for silicon nitride etching is carefully selected so that it does not damage the underlying silicon oxide layer. SF_6-based RIE can exclusively etch silicon nitride. Chamber pressure is 100 mTorr and SF_6 flows at 13.9 SCCM with a RF power of 140 W. The resulted etch rate was about 600 angstrom/min.

3.1.7 Photoresist Removal & Cleaning

After RIE, most of the photoresist is dissolved out with acetone. Then, some chemically or thermally transformed photoresist is removed in pirana solution. Complete cleaning of electrode surface is critical in the electrochemical performance of electrodes. Very thin organic contamination, even one molecular layer, can impede the catalytic property of electrode significantly.

3.1.8 Dicing and Wiring

Every sensor must be diced from the whole wafer. Wafers are scribed with substrate scriber. The individual dice are aligned to the [110] directions of the (001) wafer so that a light scribes was enough to break the wafer into individual pieces.

Gold plated copper wires are attached to the contact electrodes by epo-tek H27D silver epoxy from Epoxy Technology, Inc. (Billerica, Massachusetts). Part A (epoxy) and part B (hardener) are mixed in 1:1 ratio. After application, it was cured at room temperature for 3 hours. Thermal curing was avoided due to possible organic contamination of surface. The resulted resistance of the connection was under 10 Ω which is negligible compared to the resistance of metal thin film.

3.2 Fabrication of Comb IDA Electrodes

Unlike the coplanar IDA electrodes, a pair of fingers can be positioned facing each other in a trench. This geometry of IDA is termed as comb structure.

The whole fabrication composed of 3 masks. First, trenches with aspect ratio over 1 are etched under a precise control. Then, metals are evaporated on the walls of the trenches using a tilted support for wafers. The last photolithography passivates the interconnecting metal between the IDA electrodes and contact pads. The basic process is illustrated in figure 11. The recipes for the first photolithogaraphy, photpresist removal & cleaning, PECVD and RIE of Si_3N_4 are the same as mentioned in the fabrication of coplanar IDAs electrodes. In this chapter, the process conditions are described only for the steps different from the previous chapter.

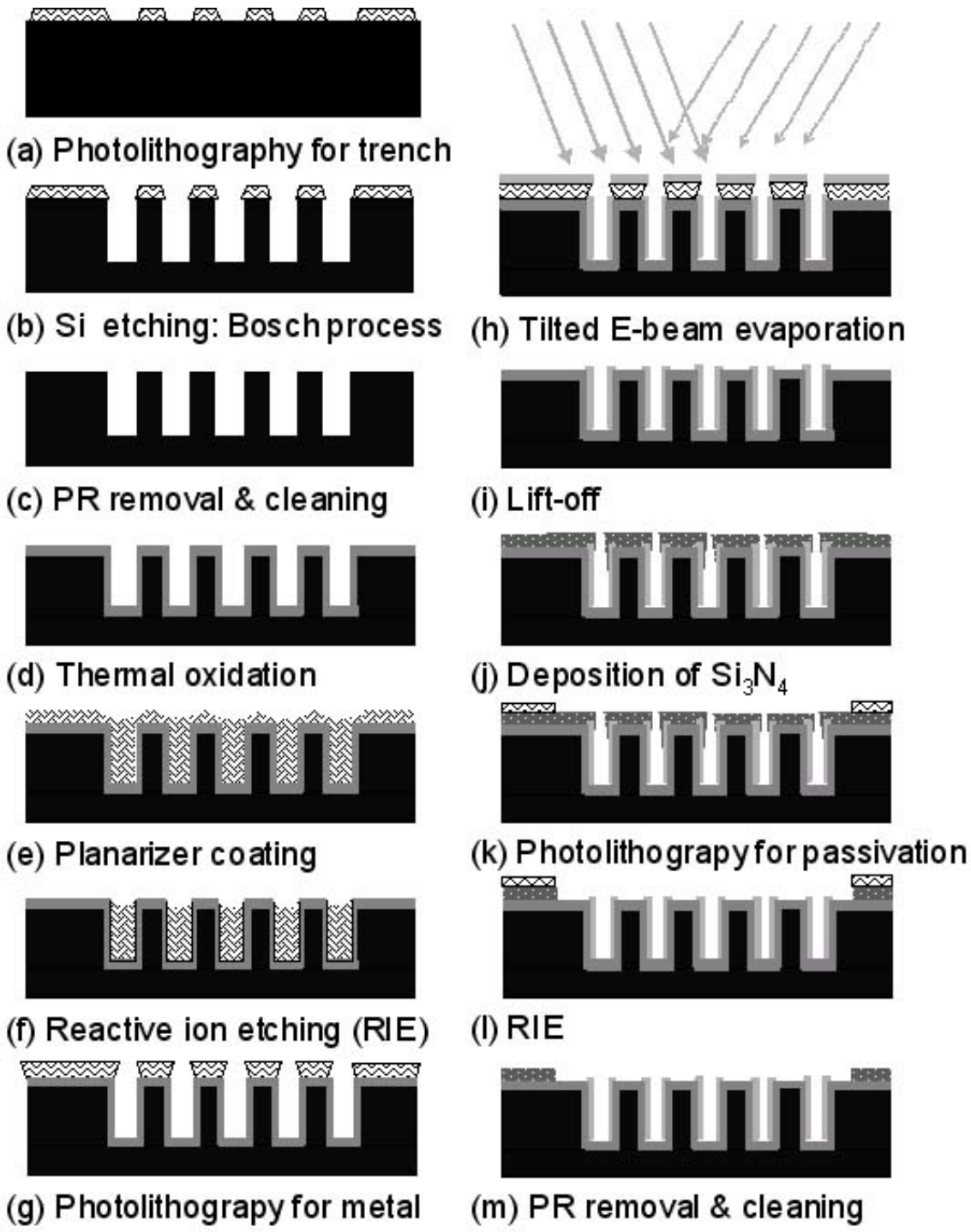

Figure 11. Fabrication process for comb IDA electrodes

3.2.1 Si Etching: Bosch Process

After the photolithography, micro-trenches are made through an etching process for silicon substrate. Si can be etched anisotropically through dry or wet process. KOH etching is a representative anisotropic process. The simplest structures that can be formed using KOH are V shaped groves, or pits with right angled corners and sloping side walls with crystal orientation (100). The angle of the slope is 54.7°. Using wafers with different crystal orientations can produce grooves or pits with vertical walls. This is preferred as a bulk process since the etch rate is relatively high. Thus, the control of etch rate is more complicated and a etch stopper is recommended.

In our work, the desired size of trenches is in the range of a few micrometers so that a dry etching is considered as a proper method. The Bosch process is a Deep Reactive Ion Etching (DRIE) related technology[39]. This technique involves repeated exposure of a photoresist-masked silicon wafer to an etchant (SF_6) plasma in alternation with a passivant (C_4F_8) plasma. So the etching process cycles between etching and deposition steps several times to achieve a deep etching with a quite vertical profile. The etch rate, profile and selectivity to the mask can be controlled by adjusting etch and passivation steps efficiency or the time ratio of the two steps.

Trenches with a depth of 5 μm are etched in Plasma-Therm ICP(inductively coupled plasma) etcher. The parameters are set for a vertically right angled etching and the etch rate is 0.5 μm/cycle. Figure 12 shows the vertical cut of trenches after 20 cycles of standard Bosch process. One can find scalloping on the walls of trenches due to the cycles of deposition and etching. Since it could cause an undesirable effect in the subsequent evaporation of metal, the surface was inspected with an AFM (atomic force

microscope). The image was taken in contact mode with Nanoscope III SPM (scanning probe microscope) from Digital Instruments (Woodbury, NY). Figure 13 shows the wall of trench has waviness with smooth grooves (50 nm deep and 500 nm wide). These shallow waves do not result significant shadow effect in the next metal deposition. We have probed the effect of process parameters on the waviness of sidewall. Shorter etching in the cycles left shallower waves with shorter period but the plasma became unstable and black silicon was lumped on the bottom of trenches. Therefore, the original condition was resumed and maintained consistently.

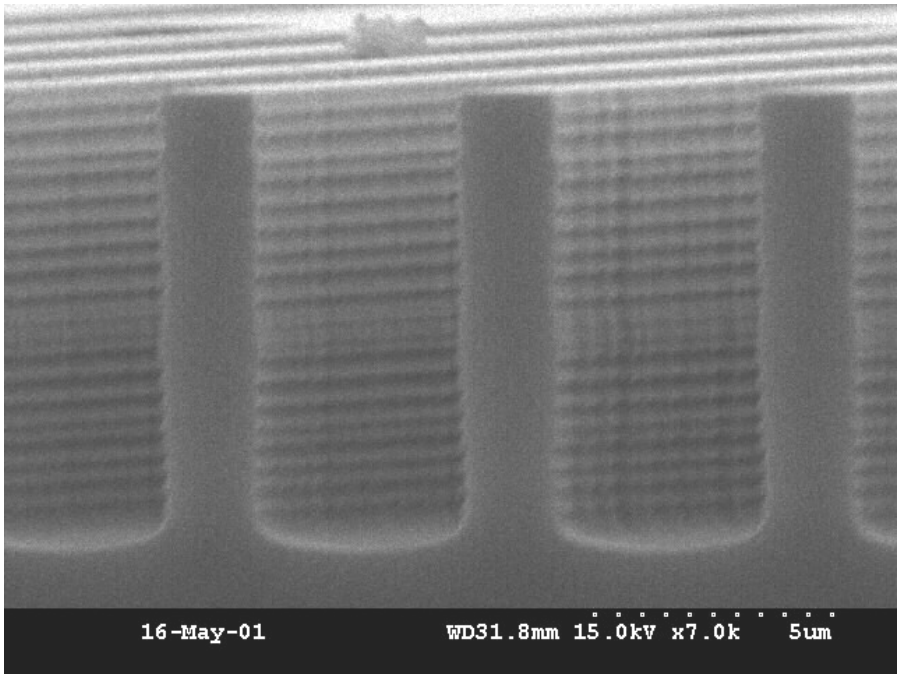

Figure 12. SEM image of trenches after 20 cycles of standard Bosch process

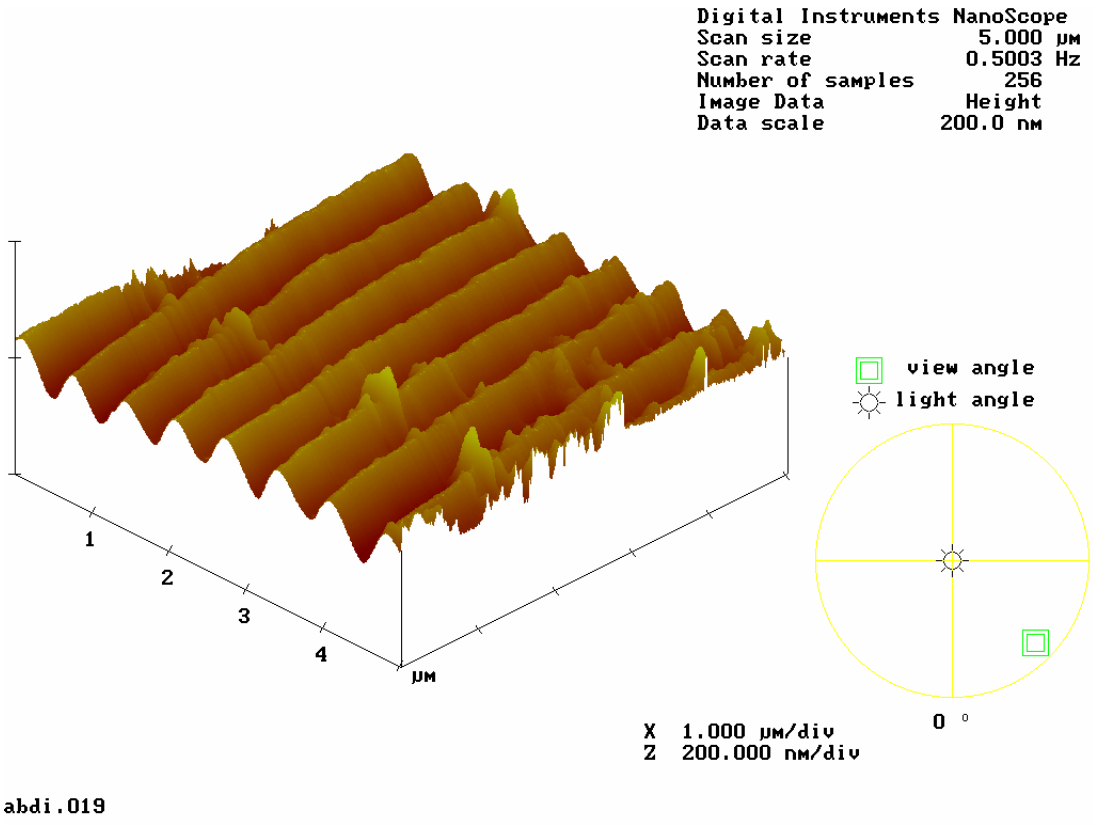

Figure 13. AFM image of a sidewall of a trench

3.2.2 Thermal Oxidation

Silicon oxide layer for insulation covers the surface of wafers where trenches were defined. When a wafer was exposed to photolithographic processes the wafer possibly contains some organic contamination. Then, thermal oxidation is not preferred since very little organic stains could contaminate the whole chamber at the extremely high temperature.

The simplest way to build SiO_2 is PECVD which can easily deposit 0.5 μm of SiO_2 within an hour. Figure 14 is the SiO_2 deposited through PECVD at 300°C for 10 min. The thickness of silicon oxide layer is not uniform in the trenches, which means that the reaction rate is faster than the diffusion of chemical vapor. Thickness of silicon oxide is 0.6 μm on top of the trenches but oxide in the trenches is hard to recognize. Whereupon, PECVD oxide is not proper as an insulating layer.

Unlike the PECVD, thermal oxide makes well-built conformal layer through a dry oxidation. Slow reaction rate of dry oxidation limit the growth rate of oxide so that the different diffusion of oxygen cannot affect the thickness of the layer. The contamination of the chamber, however, is a remaining problem. The wafers are cleaned with hot pirana solution at 80°C and rinsed very carefully with deionized water. The recipe for thermal oxidation is the same as written in the fabrication of coplanar IDA electrodes.

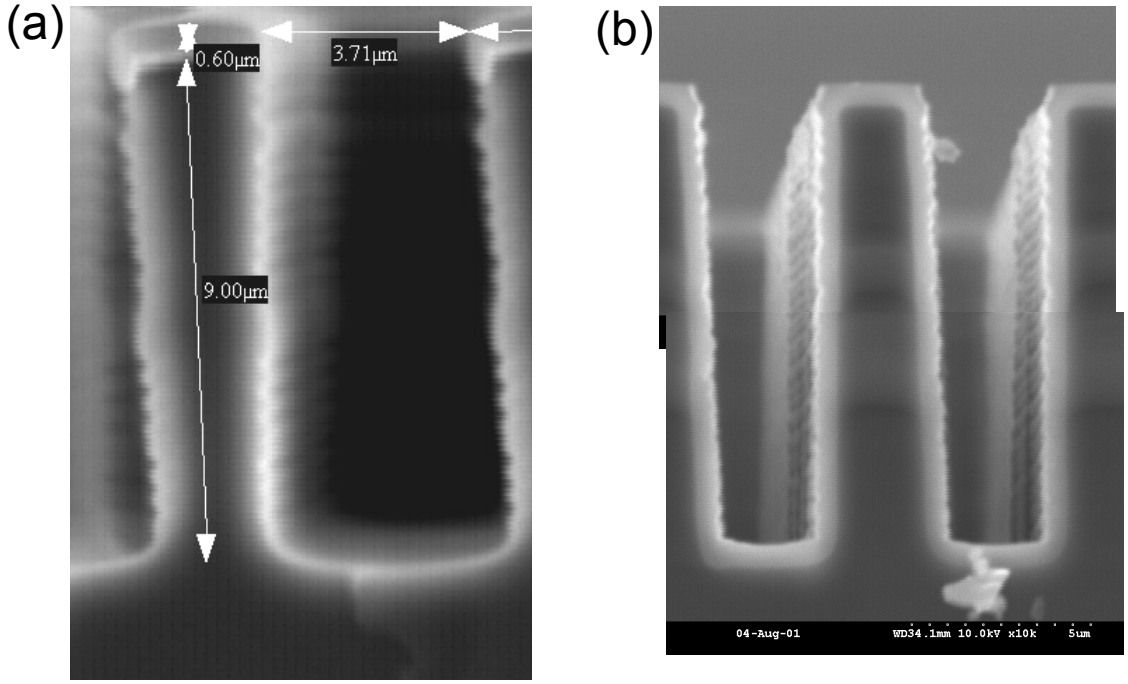

Figure 14. (a) PECVD oxide (b)Thermal oxide

3.2.3 Planarization of The Surface

For successful patterning photoresist need to be evenly coated on a substrate. However, there are trenches with 5 μm in depth arrayed with minimum gap of 2.3 μm on the wafer. One resolution is to use a thick photoresist to fill out the trenches. In our case, the feature size defined is about 2 μm so that the photoresist had better be thinner than 2 μm to make sure that the small features are transferred. Due to the dilemma, a planarizing agent is addressed before the photoresist is coated.

PC3-6000 is a planarizing polymer from Futurrex (Franklin, NJ). It is spin-coated on the wafer at 2000 rpm for 40 seconds and cured on a hot plate at 200 °C for 1 minute. The consequential thickness of the polymer is 6 μm on the flat region. The trenches are infilled and the concaves above trenches are about 0.3 μm in depth. Then, the 6 μm of polymer is removed by oxygen plasma. The wafer was processed in the Plasma-Therm RIE chamber with etch rate of 0.4 μm/min. The polymer is slightly overetched for 17 minutes and the final depth of the recess on the trench is about 0.7 μm which is tolerable in the next photolithography. All of the depth profile for the polymer was checked with Alpa Step 500 profilometer from KLA-Tencor (Milpitas, Ca).

3.2.4 Photolithography for Metal Pattern

(a) Photoresist spinning

For better adhesion of photoresist, wafers are baked on a hot plate at 150 °C for 3 minutes as a dehydration bake. Negative photoresist was selected for this process because the photoresist in the trenches need to be removed. In case of positive photoresist, the UV-exposed part is removed and, then, the photoresist in the trench is exposed. However, photoresist in the trenches is more complicated so that it is more difficult to find the exact condition of exposure. NR7-1500p photoresist, then was spun for 30 seconds at 2800 rpm, which makes 1.5 μm thick photoresist coated. This photoresist is designed to be stable at fairly high temperature (up to 150 °C) and gives vertical profile after development.

(b) Pre-bake

Photoresist is prebaked on a hot plate for 100 seconds at 150°C.

(c) Exposure

Photoresist was exposed to UV light using Karl Suss MA-6 mask aligner (Waterbay, CT) in a vacuum contact mode. Proper dose is 95 mJ/cm2 in constant intensity mode.

(d) Post-exposure cure

The wafer is cured at 100 °C for 90 seconds on a hotplate to get the exposed part of photoresist cross-linked.

(e) Developing

Photoresist is developed in RD6 for 20 seconds. The planarizing polymer is simultaneously dissolved out from the trenches in RD6 solution. Wafers are then rinsed with DI water, dried with nitrogen and inspected with microscope.

3.2.5 Tilted E-Beam Evaporation

Metal layer is deposited on the two sidewalls of trenches by evaporating it twice at the angle of 45°. A 100 angstrom Ti was deposited as an adhesion layer then 800 angstrom of platinum is deposited. Since platinum has a high melting point, the wafer becomes hot as the deposition proceeds and the photoresist might be thermally transformed. To alleviate the heat accumulation around the photoresist, aluminum thermal mass is attached to the back of the wafer. Monitored temperature of the wafer did not exceed 120 °C during the five minutes of platinum evaporation, which is permissible since the photoresist, NR7 series, is designed to endure temperature up to 150 °C. A J-type thermocouple (iron/constantan) was used to measure the surface temperature of the wafer. Figure 15 is an SEM image of a sidewall of trench after evaporation of metal. The shadow effect of evaporation defines the metal layer on the upper part of the sidewall and ensures the separation of one side of an IDA electrode from the counterpart.

Subsequent lift-off and PECVD for Si3N4 is the same as described in the fabrication of coplanar IDA electrodes.

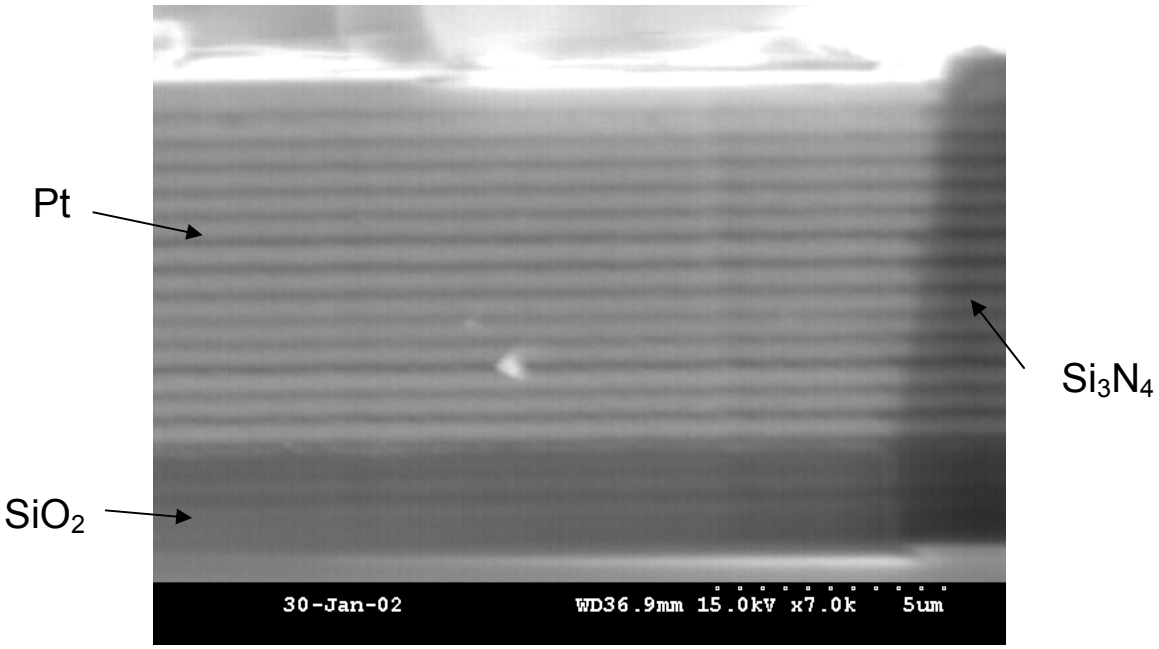

Figure 15. Evaporated platinum layer on the sidewall of trench.

3.2.6 Photplithography for Passivation.

Thick photoresist, AZP 4620, is applied for the patterning of silicon nitride due to the presence of trenches.

(a) Photoresist spinning

For better adhesion of photoresist, wafers are baked on a hot plate at 150 °C for 3 minutes as a dehydration bake. AZP 4620 photoresist, then was spun for 20 seconds at 700 rpm. Resulted thickness of photoresist is 20 μm, which compensates the depth of trenches.

(b) Pre-bake

Photoresist is prebaked on a hot plate for 15 minute at 100°C.

(c) Exposure

Photoresist was exposed to UV light using Karl Suss MA-6 mask aligner (Waterbay, CT) in a vacuum contact mode. Proper dose is 1200 mJ/cm2 in constant intensity mode at CI-1 which was initially calibrated for 6mW/cm2 at 365nm.

(d) Developing

Photoresist is developed in 1:3 solution of AZ 400K developer concentrate and DI water for 3 minute. Wafers are then rinsed with DI water, dried with nitrogen and inspected with microscope.

(e) Post-bake

Wafers were baked again on a hot plate at 100°C for 3 minute. It makes the defined features of photoresist hardened and preserved during the reactive ion etching (RIE).

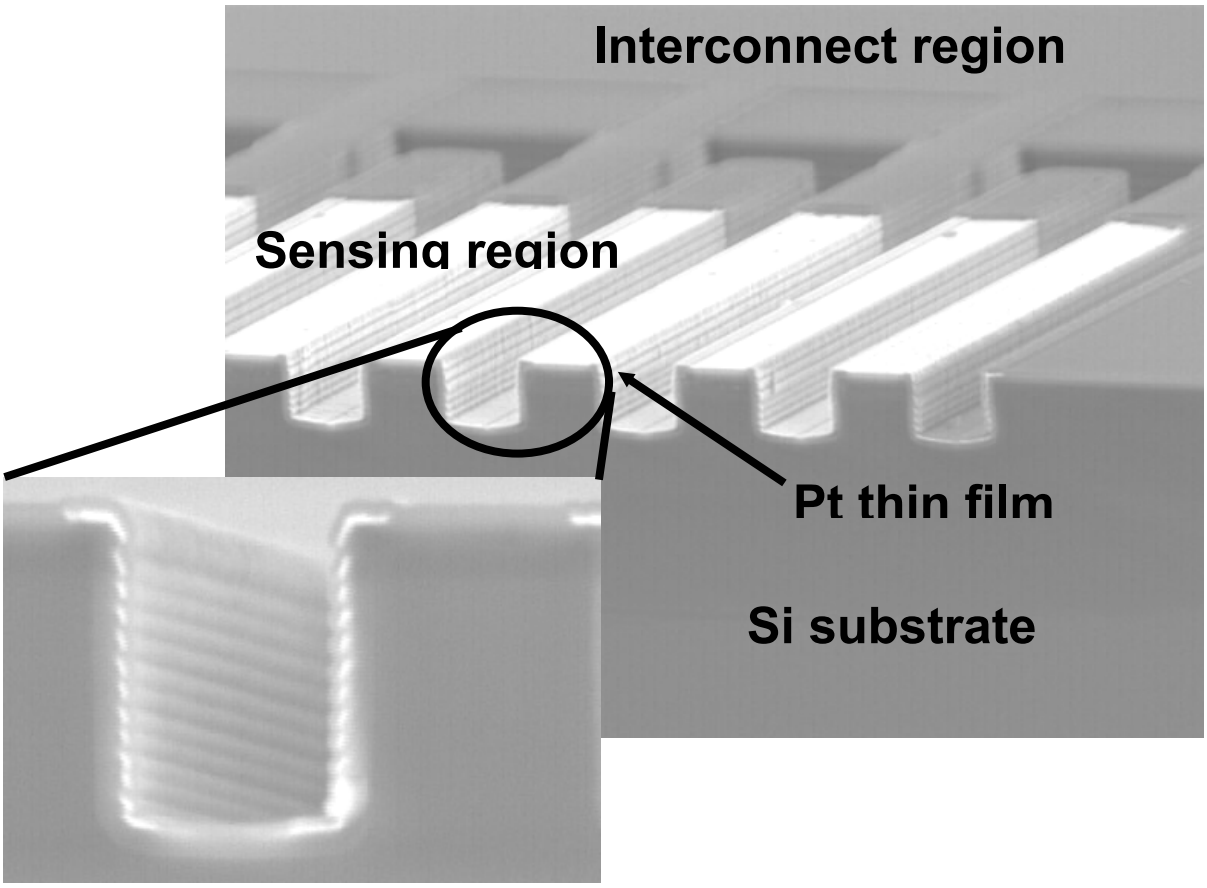

Figure 16. Cross-section of a comb IDA electrode. The chip was vertically cut across the center after completion of fabrication. Dark surface is passivated with silicon nitride layer.

3.3 Fabrication of Comb IDA Electrodes for a Microfluidic System.

For an electrochemical measurement, such as cyclic voltammetry of chronoamperometry, three electrodes are required; working, reference and auxillary electrode. Those three electrodes can be integrated in a microchannel built on a chip. IDA electrodes are working electrodes in the three electrode system.

Generally Pt mesh is used as an auxiliary electrode in a macroscale experiment since the area of auxiliary electrode is more than 10 times bigger than the working electrode's. 3 × 0.5 mm thin film of Pt, 20 times larger than working electrode(0.3 × 0.25 mm), is used a as an auxiliary electrode in our chip, which can be built with IDA electrode without additional process.

Saturated calomel electrode and Ag/AgCl electrode are the most common reference electrodes in macrosystems. A liquid junction Ag/AgCl electrode was fabricated using microfabrication technology and showed no dependence on pH and KCl concentration[40]. It is not applicable to the IDA electrode system due to its complex fabrication process and relatively bulky size. Since all of our experiments are done in a buffer solution there is no perceptible changes in pH or Cl- concentration. Thus, chlorinated silver wire functions as a substitutional reference electrode in the experiments in a microdrop, which will be described later in chapter 5. For a microfluidic system, chlorinated silver film was fabricated through an electroplating and electroless chlorination, which can be accomplished without additional photolithographic process.

Another modification in process was the dicing of wafers. Since the chip is assembled with a microchannel, irregular shape of the chip from scribing was unallowable. The wafer was diced with dicing saw with tolerance of 50 μm.

Figure 17 is the completed IDA electrode chip ready for the assembly with a microchannel. The final size of the chip is 10 × 20 mm.

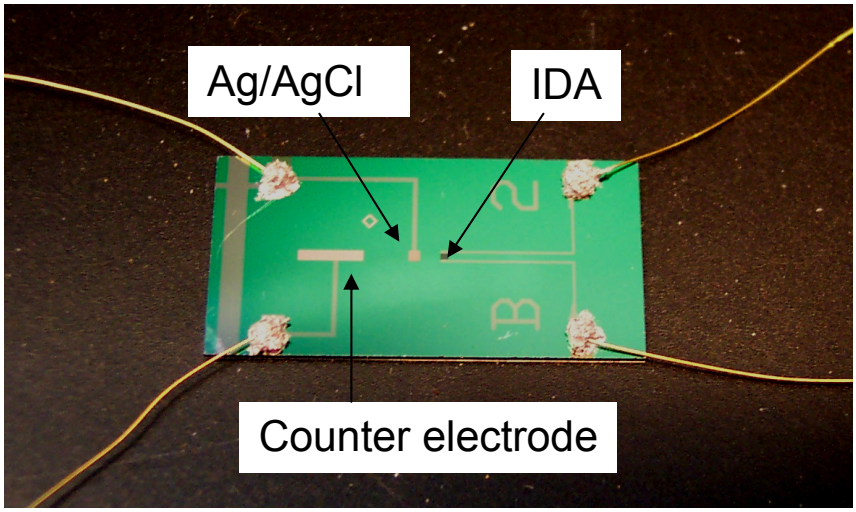

Figure 17. The IDA chip for integration to a microfluidic system.

3.3.1 Electroplating of Ag

All of the fabrication process was carried out with a wafer as described in fabrication of comb IDA electrodes. Before dicing the wafer, reference electrodes are completed by electroplating silver on the rectangles of Pt thin film designated to reference electrodes. These rectangles are electrically connected to a large contact pad on the edge of the wafer.

The plating bath is filled with Techni-white Silver from Technic Inc, (Cranston, RI) which is a cyanide-based electroplating solution for Ag. The expected Ag consuming rate is 4 g/A·hr. The wafer was connected to the (-) of a power supply and soaked in the plating solution. (+) of the power supply was connected to a Pt mesh working as a counter electrode. The plating bath was agitated vividly while the electroplating proceeded. Silver electroplating was performed in a constant current mode with a current of 5 mA and the Ag deposition rate was 4 ± 0.4 μm/ hr where the variation was due to the resistance between the contact pad and each pattern. The most distant pattern showed 200 Ω from the contact pad. The Ag was deposited for 1 hour on Pt rectangles (500 × 500 μm) designated to reference electrodes resulting in a white mat thin film with a thickness of 4 μm on average. Thickness of Ag film was limited by the adhesion to the underlying Pt layer since thicker Ag films came off while dicing the wafer.

The electroplating solution did not leave any deposition or adsorption of Ag on the non-potentiated Pt surface which is IDA electrode or auxiliary electrode. After rinsing the wafer with deionized water, sweeping potential at -0.6~1.0 V vs. SCE was applied to the Pt electrode in a clean buffer solution. No recognizable peaks appeared in the current response which means there is no contamination of Ag on the electrode.

3.3.2 Electroless Chlorination of Ag

Ag can be chlorinated electrochemically in a Cl^- abundant solution. KCl solution is commonly used in a constant current mode. The alternative method is electroless chlorination with strong oxidant, $FeCl_3$.

$$Ag + FeCl_3 \rightarrow AgCl + FeCl_2$$

After electroplating Ag, the wafer was soaked in 1 % ferric chloride aqueous solution for 20 minutes. As chlorination proceeded the color turned from white into dark grey.

Figure 18 is the cross section of electroplated silver layer whose surface is chlorinated. Ag was deposited to the thickness of 25 μm and soaked in the ferric chloride solution for 40 minutes. The silver film was separated from the substrate and settled in a polymer which was exothermically hardened. The top of polymer was ground with fine alumina powder until the cross-section of Ag film unclosed. The interface between AgCl and Ag was erratic due to non-uniform growth of Ag grain. Average depth of chlorination was 3.7 μm.

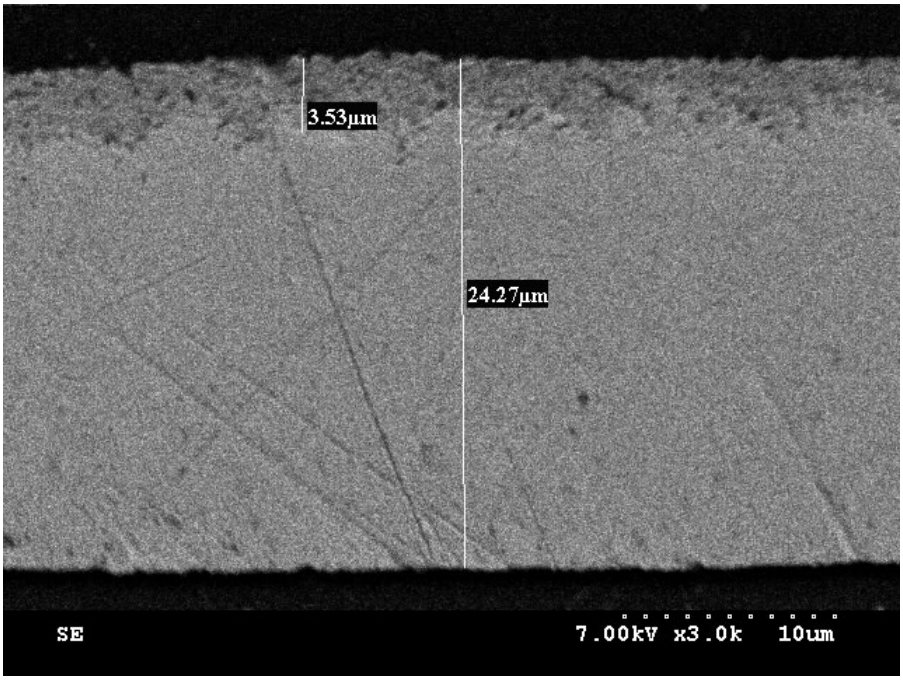

Figure 18. The surface of electroplated Ag is chlorinated to form a AgCl layer

3.3.3 Stability of Ag/AgCl Reference Electrode

The stability of the thin film reference electrode is worth investigated since it is very important to apply potentials in a reproducible manner. Since it is not a liquid junction electrode, the electrode potential is off from the conventional macroscopic electrode potential. The deviation owing to a varied concentration of Cl^- is tolerable if the experiments are carried out in the same buffer solutions and the potential is stable in the solution. It is well-known that the solubility of AgCl is non-negligible in solutions of high Cl^- concentrations[41]. This problem, although trivial for macroscopic electrodes, can become critical when only a few micrometers of AgCl are present.

The potential of Ag/AgCl thin film electrode and chlorinated Ag electrode were measured versus SCE in 0.1 M phosphate buffer at pH 7.5. The stabilities can be compared in Figure 19. Potentials for thin film electrodes started to drift after 16 hours while the potential of wire electrode stayed stable. In actual assays, one measurement takes about 10 minutes for detection and cleaning. Thus, 16 hours corresponds to over 100 measurements which is sufficient for one set of immunoassay. The electrode potentials of Ag/AgCl electrodes were 205 mV for both thin film and wire electrodes.

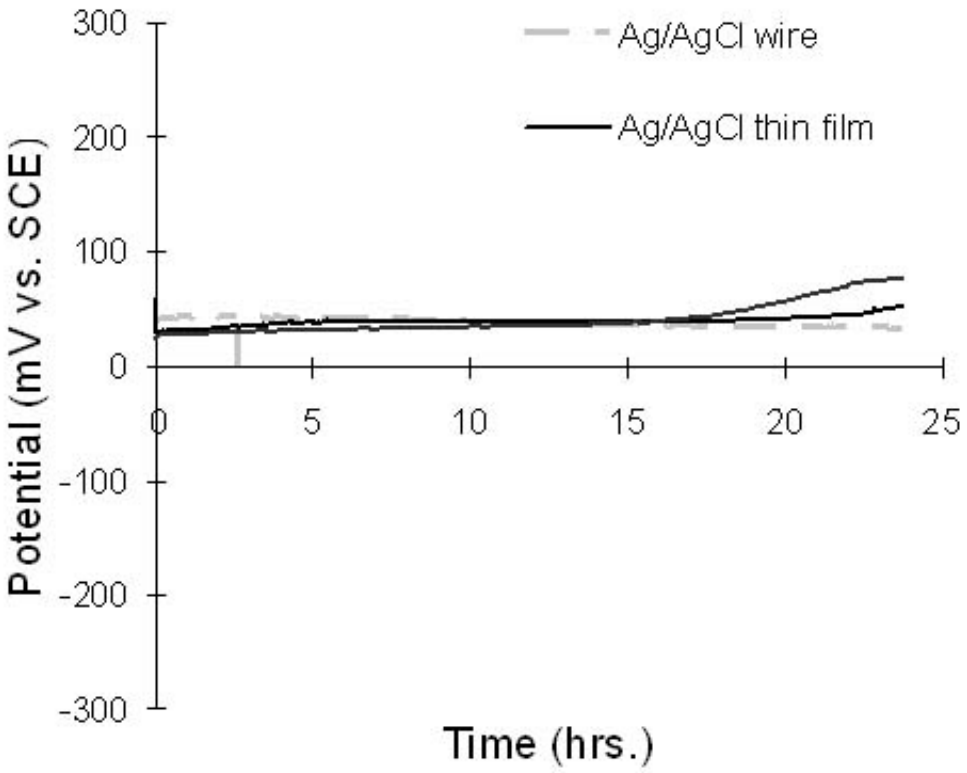

Figure 19. Potentials of Ag/AgCl reference electrodes vs. time

4. CHARACTERIZATION OF IDA ELECTRODES

The fabricated IDA electrodes were electrochemically characterized using an example of redox couple, ferri/ferro cyanide ion.

$$Fe(CN)_6^{3-} + e^- \leftrightarrow Fe(CN)_6^{4-} \qquad E° = 0.361 \text{ (vs. NHE)}$$

The above reaction is a well-known example used to test electrochemical systems due to its slightly positive redox potential and reversibility. However, ferricyanide slowly reacts with photon and degrades in aqueous solutions so that fresh solution has to be prepared every time the experiments are practiced.

Considering the MiRC cleanroom facilities at GA Tech, coplanar IDA electrodes were designed with 2 μm and 3 μm gap; comb IDA electrodes were designed with 3 μm and 5 μm gap. Actual size of the gap was reduced by about 0.5 μm after fabrication due to the dispersion of light during exposure.

4.1 Materials and Methods

$K_3Fe(CN)_6$ was purchased from J.T. Baker Chemical Co. (Phillipsburg, NJ). NaH_2PO_4, Na_2HPO_4, KCl, NaN_3, and NaOH were purchased from Fisher Scientific (Fair Lawn, NJ). Buffer was made with 0.044 M NaH_2PO_4, 0.056 Na_2HPO_4, 0.1 M KCl, and 0.003 M NaN_3 dissolved in deionized water. Both buffers were adjusted to pH 7.4 with concentrated NaOH.

For the IDA electrode experiments, the 2 contact pads were covered with glue and sealed with epoxy to keep them off from the solution. The IDA region of the chip and a reference electrode were soaked in 10 mL of buffer solution. A saturated calomel reference electrode (SCE) from Bioanalytical Systems, Inc. (West Lafayette, IN) or a 0.015" diameter Ag/AgCl wire from A-M Systems, Inc. (Carlsborg, WA) was used as a reference electrode. A platinum wire auxiliary electrode completed the electrochemical cell.

The two wires from the IDA chip were connected to a potentiostat. The potential was cycled between 500 and -200 mV vs. SCE at 50 mV/s for cyclic voltammetry (CV) experiments. For dual mode CV, one of IDA (collector) was potentiated at 500 mV while the potential at the other side (generator) was cycled as in the single mode CV. A CH Instruments 832A Electrochemical Analyzer was used as the bipotentiostat for IDA experiments.

4.2 Comparison of Pt and Au Electrodes

Coplanar IDA electrodes were fabricated with gold and platinum as mentioned in chapter 3. Pt is the most common material for electrodes due to their chemical inertness. The potential range for Pt electrodes in a neutral aqueous solution is from -0.6 to 1.0 vs. SCE. Au was frequently used as a thin film electrode too. Au is favorable especially in terms of easiness in microfabrication due to the relatively low melting point. Standard wire bonding process helps instrumentation of Au electrodes with other components such as a potentiostat.

Potential was swept 100 cycles on Au and Pt IDA electrodes in a buffer solution of 10 mM $K_3Fe(CN)_6$. Figure 20 shows the surface of IDA electrodes after the test. Pt electrode looks intact while the surface of Au electrode has many cracks and small lumps. The damage is presumed to be a result of reactions between the potentiated Au and chloride ion in the solution. Thus, Au was ruled out and Pt was used for the experiments with IDA electrodes.

(a)

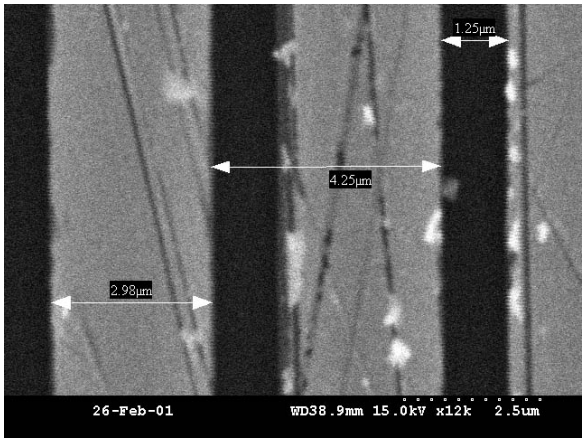

(b)

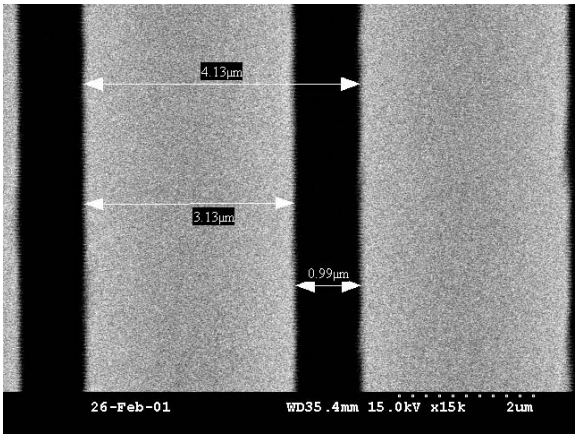

Figure 20. Surface of IDA electrodes after 100 cyclic voltammetry (a) Gold electrode (b) platinum electrode

4.3 Stability of Pt Thin Film Electrodes

The catalytic property of Pt was investigated with a disk electrode and thin film electrodes with different thickness; 400 angstrom and 1000 angstrom. It is believed that thicker film of Pt keeps its bulk property better than a thinner one. In reality, ultra-thin Pt deposition builds islands of Pt and conducts electricity in a different physical mechanism from the metallic conduction. However, deposition of thick Pt layer makes the process of lift-off complicated as described in chanter 3 not to mention that Pt target is very expensive. We need to know the proper thickness Pt layer which keeps the conducting and catalytic functions as is the Pt disk electrodes.

Figure 21 is cyclic voltammogram(CV) for a disk electrode and thin film electrode (400 angstrom thick) in a phosphate buffer solution at pH 7. At each electrode, potential from -1.2 to 1 V was scanned with a scan rate of 50 mV/sec versus an Ag/AgCl reference electrode. The current range is quite different since the area of disk electrode is almost 10 times bigger than the thin film electrode's. For comparison, left and right axis for current scale were adjusted to overlap the two curves. We could ascertain that the shapes are identical; location of peaks and the ratio of peak height. It means that the thin film electrode with a thickness of 400 angstrom is enough to keep the catalytic property of bulk Pt. Besides, Ti used as an adhesion layer is confirmed to be oxidized and caused no undesirable effects.

It was probed if the thickness of thin film affects the stability of electrodes. The performance of each electrode was monitored for 3 days with multiple CVs for 10 mM ferricyanide buffer solution. Electrodes with thickness of 400 angstrom and 1000 angstrom show the same behavior which means the stability of Pt thin film electrodes is

not affected significantly by their thickness when Pt is thicker than 400 angstrom. Curves in Figure 22 illustrates that the performance of a Pt thin film electrode is maintained after 3 days of multiple uses. The first CVs of the day tends to be a little off from the rest of curves but the electrode resumed the condition after couple of CVs. Thus, it is desirable to practice at least 5 times of CVs in buffer solution as an initiating process when the electrode was resting for a while.

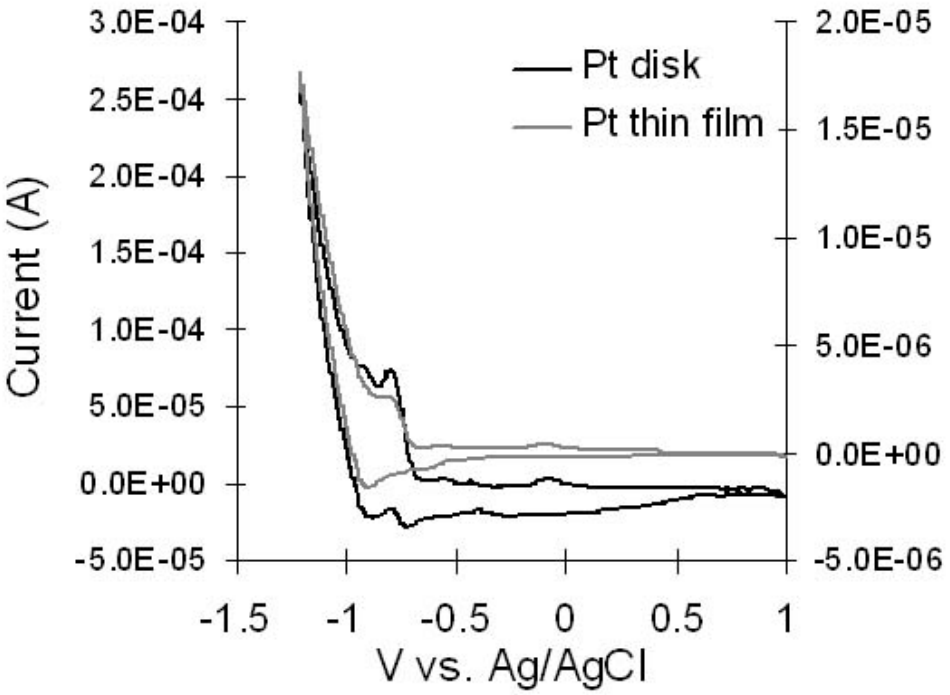

Figure 21. Cyclic voltammogram for Pt disk and thin film electrodes in PBS buffer (pH 7). Left axis for disk electrode, right axis for thin film electrode

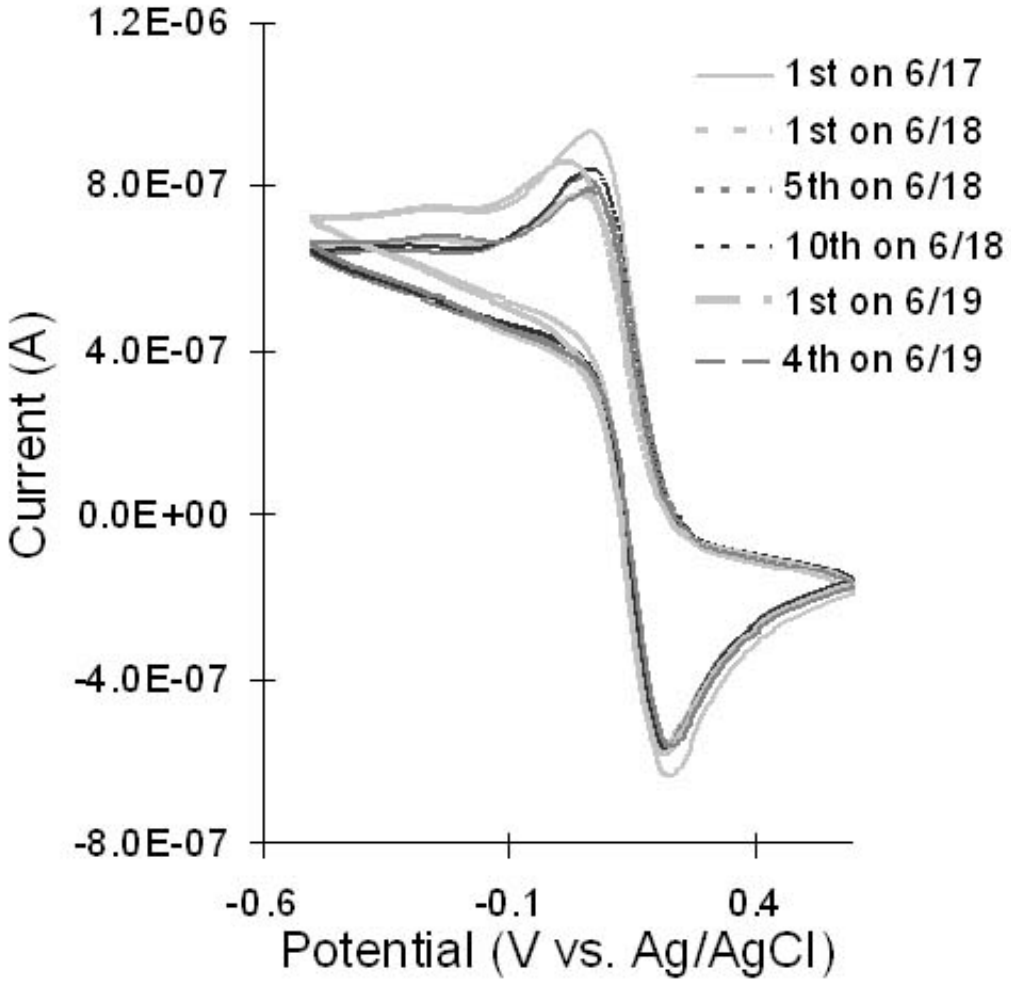

Figure 22. CVs for a Pt IDA electrode for the stability test

4.4 Dual Mode CV for Redox Cycling

The standard electrode potential for ferri/ferro cyanide is known to be 0.12 V versus SCE whose reference potential is 0.24 V. The electrode potential of Ag/AgCl wire, a quasi-reference electrode, was -0.04 V measured versus SCE. Thus, the peaks in a normal (or single) mode CV for ferri/ferro cyanide appear around 0.16 V with Ag/AgCl wire reference electrode.

The shape of the curve changes when redox cycling occurs on the IDA electrode. Since the generator electrode supplies the consumed species by the collector electrode, the current does not decrease but approaches to a plateau. Figure 23 illustrates CV in single mode and dual mode of a coplanar IDA electrode with 2.5 μm gaps. Limiting current, the converged value, is 3.42 μA.

For comparison, the diffusion-controlled limiting current was calculated for the IDA by the equation in chapter 2. Number of band electrode pairs is 20, the number of electrons is 1, the band length is 250 μm, the bandwidth is 3.5 μm, the gap is 2.5 μm, and the diffusion coefficient 0.76 x 10^{-5} cm^2/s. When the concentration of $Fe(CN)_6^{3-}$ is 10 mM, the limiting current is computed to be 3.82 μA. The observed limiting current is 90 % of the theoretical value, which means (1) the redox reaction is reversible, (2) the reaction rate is limited by the diffusion of ferri/ferro cyanide ions, and (3) the collecting efficiency is close to 1. According to the CV, the proper potential for the redox couple was determined where the current equilibrates. In chronoamperometric(CA) measurements, the generator and collector were potentiated at -0.2 and 0.5 V versus Ag/AgCl wire respectively.

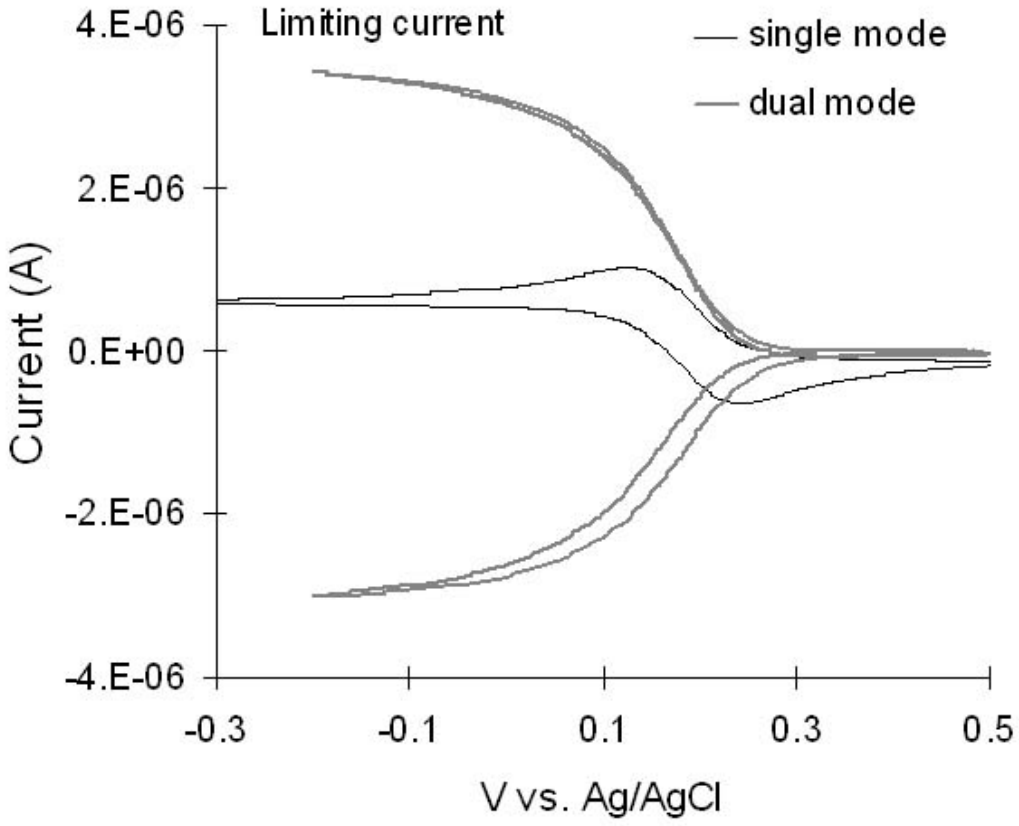

Figure 23. Cyclic voltammograms with and without redox cycling

4.5 Simulation of Redox Current on Coplanar and Comb IDA Electrodes

The limiting current of comb IDA electrodes cannot be estimated by an equation since the structure is entirely different from the planar ones. Thus, finite element method was adopted in modeling redox cycling current as described in chapter 2. Figure 2 illustrated the different path of diffusion on coplanar and comb IDA electrodes.

The limiting current was calculated by integrating the flux over the surface of the electrodes. Improved integration was obtained by using a much finer geometric grid in the FEA analysis at the surface of the electrodes compared to in the solution. C_{Bulk} was set to 1 to produce a normalized concentration profile. Figure 24 is the relationship between the limiting current and the size of gaps. The redox cycling current is linearly proportional to 1/gap, which agrees with the expectation of the equation on coplanar IDA electrodes. The comb electrode has 3 times more current than coplanar IDA for the same size gaps. This current increase is because the effective electrode surface area was increased by using the walls of the trenches, and the diffusion distance between generator and collecting electrodes was decreased as mentioned previously.

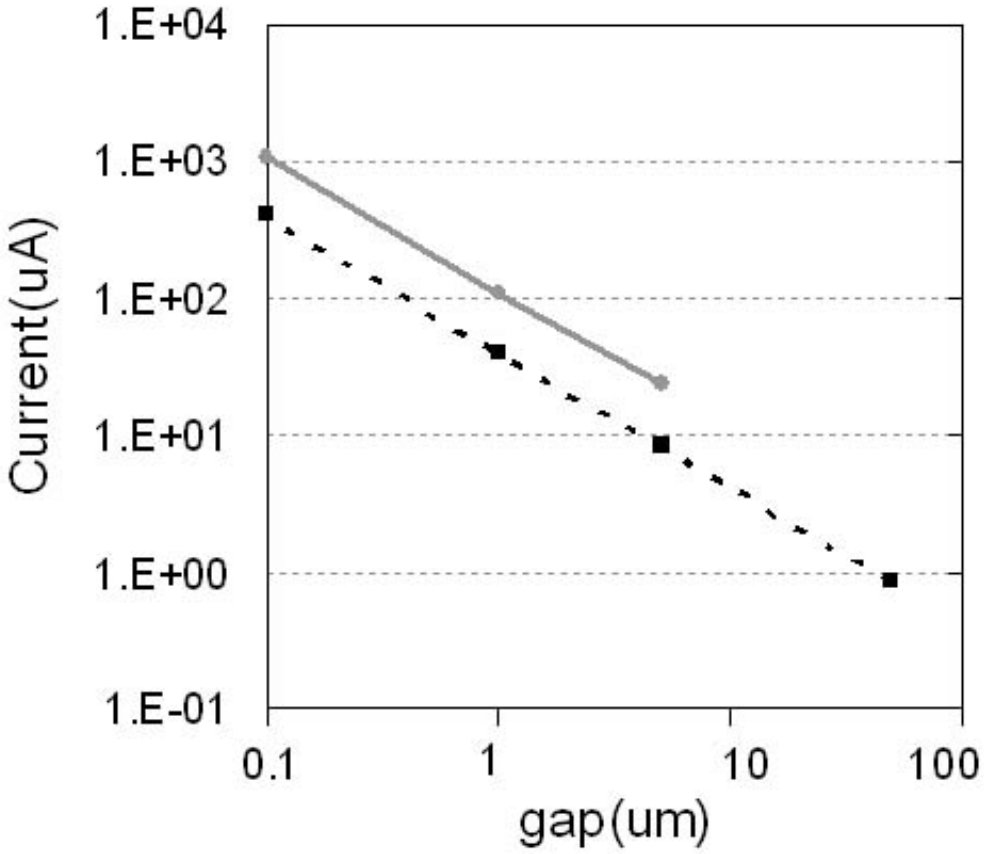

Figure 24. The calculated limiting current vs. size of gap for coplanar (dotted black) and comb (solid grey) electrodes

4.6 Comparison of Coplanar and Comb Electrodes

The actual redox cycling currents were compared on the coplanar and comb IDA electrodes. Figure 25 shows the typical CVs for the two electrodes with the same size of gaps. The size of gap is 2.4 μm and the buffer solution contains 10mM of $K_3Fe(CN)_6$. Even though the structures are different, the shapes of curves are identical; the current of comb IDA electrode converges to a limiting value.

In chronoamperometry (CA), the currents were measured while fixed potentials were applied; generator at -0.2 V and collector at 0.5 V. The currents in dual mode CA were stabilized in a few seconds while the current kept decreasing in CA with single electrode. The steady state currents correspond to the limiting currents of dual mode CV.

Table 1 represents the steady state currents of IDA electrodes with different dimension and structure. Analyte solution was phosphate buffer (pH 7) with 0.1 mM $K_3Fe(CN)_6$ and currents at the generator electrode are indicated. The redox cycling current is evidently proportional to the reciprocal of the gap. It agrees with the result of FEM modeling. The measured current for the comb IDA electrodes was 3 times higher than coplanar ones when the gap is 2.4 μm as presumed in the simulation. The effect of area increase is 2 by utilizing sidewalls of trenches. Thus, we ascertained that the more distributed flux and the straight diffusion path of comb IDA electrodes improved the redox cycling by 50 %.

.

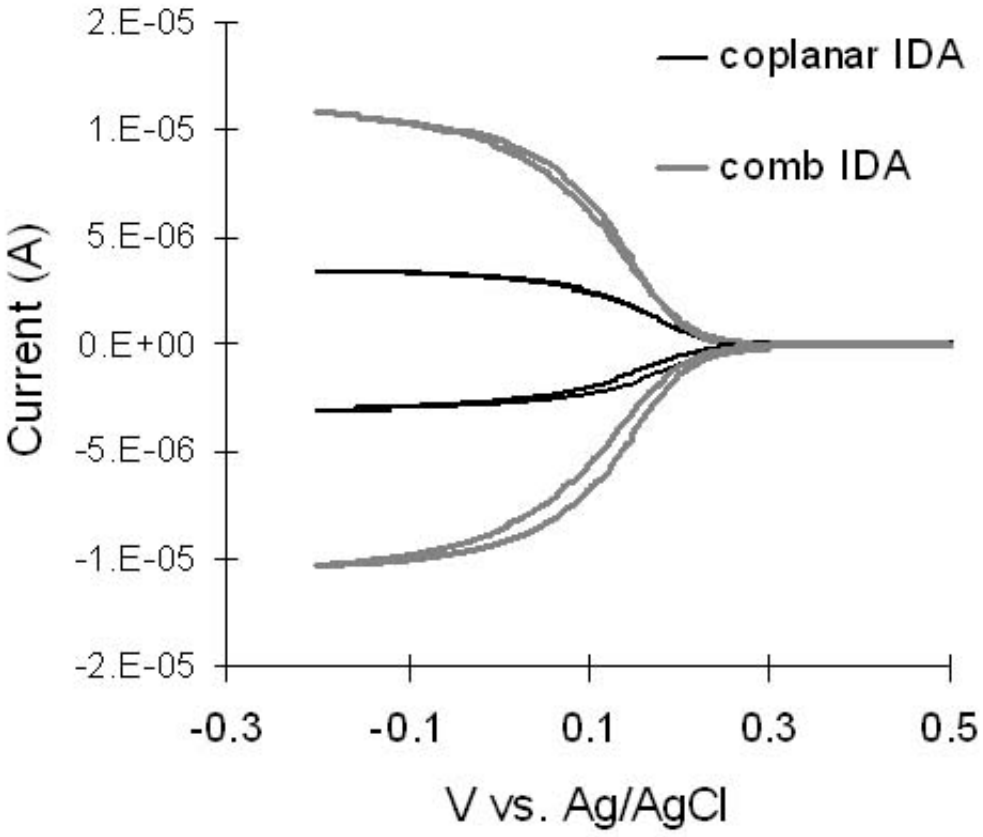

Figure 25. Dual mode cyclic voltammograms for coplanar and comb IDA electrodes

Table 1. Steady state current for different IDA electrodes during CA.

Unit: nA

Gap	Coplanar IDA	Comb IDA
1.6 μm	60	
2.4 μm	36	152
4.5 μm		80

5. IMMUNOASSAY WITH IDA ELECTRODES

Various IDA electrodes were examined with the popular reversible redox couple, ferri/ferro cyanide in the previous chapter. As the redox reaction was optimized with IDA electrodes, it played an role in confirming the performance of electrodes in this chapter. In this chapter, the redox cycling is applied to a practicable detection of biological target combined with an enzyme labeling method.

PAP/PQI redox couple is a popular choice to mediate the redox cycling and catalytic reaction of enzyme labels. To implement the scheme, electrochemical conditions were optimized for redox reaction of PAP/PQI on IDA electrodes. For rapid redox cycling of PAP/PQI, surface of the electrode was kept clean and the enzyme was immobilized on microbeads. Binding of the enzyme to the microbeads was characterized with fluorescence measurements. Then, an electrochemical immunoassay using IDA electrode was demonstrated with mouse IgG. Finally, coplanar and comb IDA electrodes with different experimental configurations were compared with regard to their performance in an immunoassay.

5.1 PAP/ PQI Redox Couple

5.1.1 Cyclic Votammetry of PAP/PQI in Alkaline Conditions.

In an ideal redox cycling format, the reactions are reversible on the electrodes and the potentials are properly adjusted to satisfy diffusion-limited condition. It requires an appropriate combination of electrode, buffer solution, pH, potential range, and so on. The related information can be gathered through cyclic voltammetry (CV).

The buffer condition for the experiments was determined by experiments with the substrate under different conditions for enzyme reaction. Alkaline phosphatase (ALP) was assumed as the enzyme label generating PAP. The enzyme is the most frequently used since it is stable and the catalytic reaction is fast. This enzyme generates PAP through a dephosphorylation of 4-aminophenylphosphate (PAPP) in alkaline conditions. 0.1 M Tris buffer was used for the enzyme reaction.

Even though the standard electrode potential for PAP/PQI couple is 260 mV vs. SCE, its redox potential migrated to around 0.1 V vs. SCE under pH 9[22] on a glassy carbon electrode. Thus, the range of potential scan was set from -0.3 V to 0.3 V vs. SCE at a scan rate of 50 mV/sec. The positive limit of potential was restricted to 0.3 V since PAPP, the substrate of enzyme reaction, begins to be oxidized and interfere the reaction of PAP thenceforth.

Figure 26 is CVs for 1 mM PAP in alkaline Tris buffer solution. PAP is known to degrade in contact with oxygen so that the CVs were performed with a fresh PAP solution. In the first and 50th scan, oxidation peak appeared at 0.09 V and reduction peak does at -1.4 V. The oxidation peak is distinct but one can hardly appreciate the presence

of reduction peak. The peaks in 50th scan wanes significantly compared to the first scan's. The current kept decreasing during multiple scans performed for the same solution with the same IDA electrode. The gradual decrease of current and disproportion between oxidation and reduction might due to the degradation of PAP or nonreversible redox reaction.

We have investigated if different electrolytes in the buffer solution affect the redox reaction. Hepis and phosphate buffers were used for CVs of PAP under the same pH. Those buffers could not alleviate the problem.

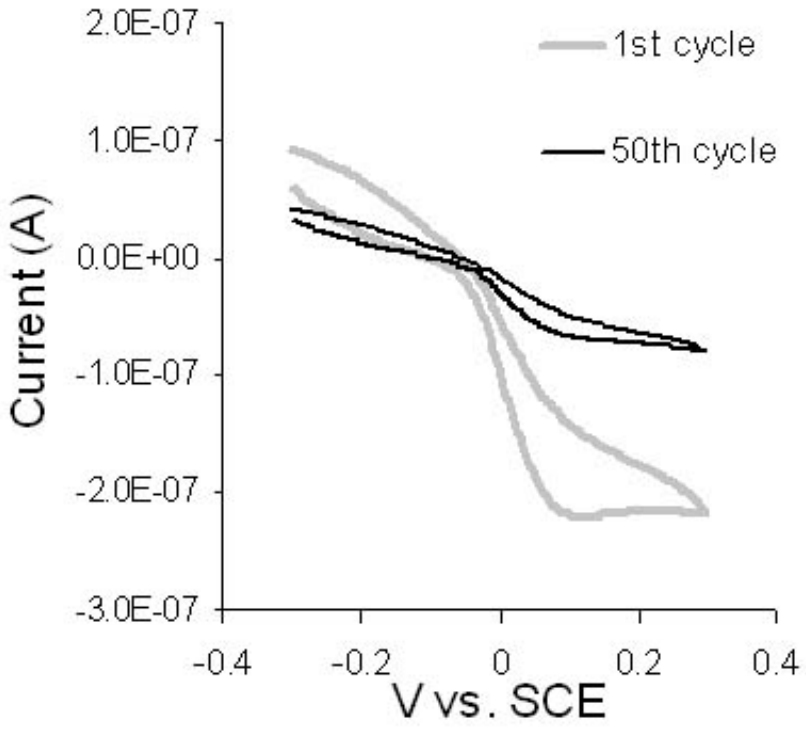

Figure 26. Cyclic voltammograms of 1 mM PAP in tris buffer (pH 9.0)

5.1.2 Electrode Contamination and Cleaning

After experiments with PAP, the status of the IDA electrodes was checked with CVs for 10 mM ferricyanide ion in a phosphate buffer (pH 7) as in chapter 4. Figure 27 compares the CVs of an electrode before and after the 3 CVs with 1 mM PAP in a tris buffer (pH 9). One can tell the shift of the wave caused by the experiment with PAP. It can be interpreted that the surface of the electrode was fouled by the redox reaction of PAP. To remove a possible contamination, the electrode was soaked in a clean phosphate buffer and potential scan at -0.6 ~ 1.0 V vs. SCE was carried out for 3 times. Then, the performance of the electrode was recovered, which means the contamination was cleared off.

To verify the contamination of electrode surface and cleaning, concentrated PAP was addressed for a longer period of time. Generator and collector were potentiated respectively at 0.3 and -0.1 V vs. Ag/AgCl wire in 30 mM PAP solution for 10 minutes. Then, the electrode was rinsed with deionized water and soaked in a clean phosphate buffer (pH 7). CVs were performed on the generator and collector electrode respectively. The collector electrode, where PQI was reduced, exhibited no recognizable change on the background. Figure 28 illustrates the result on the generator electrode where PAP was oxidized. The peaks in the dark curve are similar to typical peaks in stripping analysis. It means the material on the electrode is electrochemically dissolved into the solution. The decreasing heights of the peaks with multiple scans are due to the dissolved material diffusing out to the bulk solution. The grey line in figure 28 is obtained after the cleaning procedure of potential scan at -0.6 ~ 1.0 V vs. SCE for 10 times in a clean tris buffer. The flat curve means that the deposited material is dissolved out to the bulk solution.

The possible passivation of electrode surface necessitated periodic cleaning of the IDA electrode to keep its catalytic function. Cycling the potentials 3 times between 1.5 V and -1.2 V at 50 mV/sec in a clean phosphate buffer is enough to clean the surface in less than 4 min. The cleaning was performed between any experiments with PAP to avoid potential contamination. CV for ferricyanide ion was used to monitor changes on the electrode after the cleaning procedure. During the electrochemical cleaning, evolution of hydrogen, formed platinum oxide, striped the platinum oxide, and oxidized organic contaminants[42],[43]. A similar cleaning procedure for platinum IDA electrodes was reported that cycled potential in 1M H_2SO_4[44].

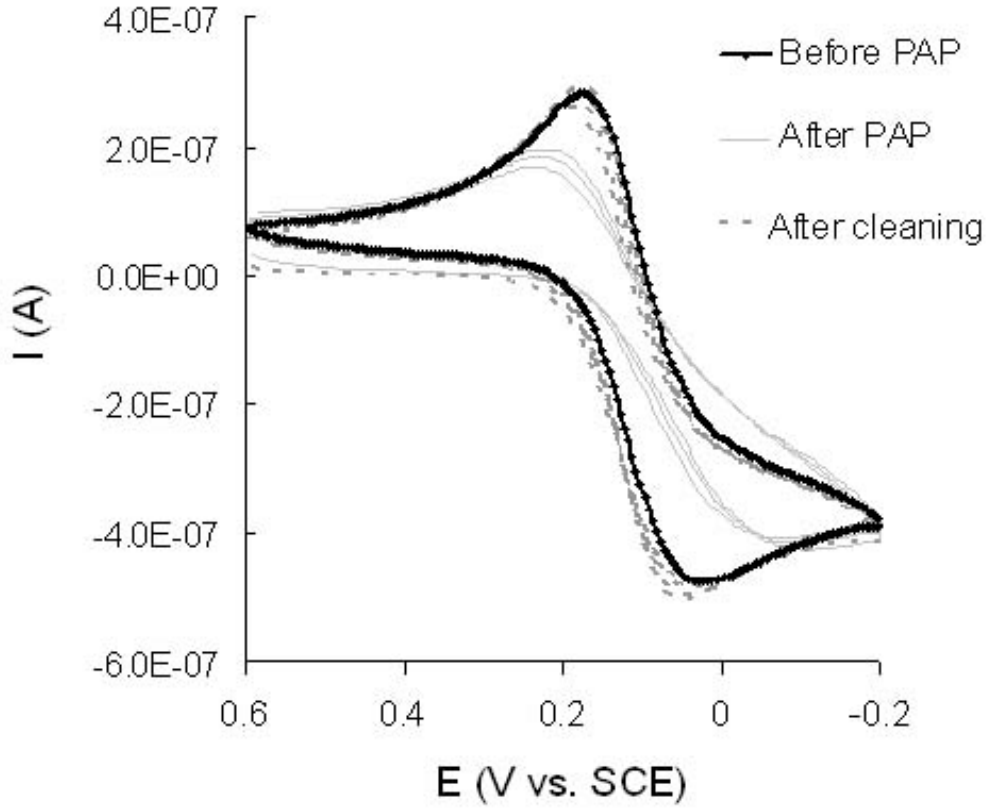

Figure 27. Cyclic voltammograms of 10 mM $Fe(CN)_6^{3-}$ in phosphate buffer (pH 7) before and after experiments with PAP at pH 9

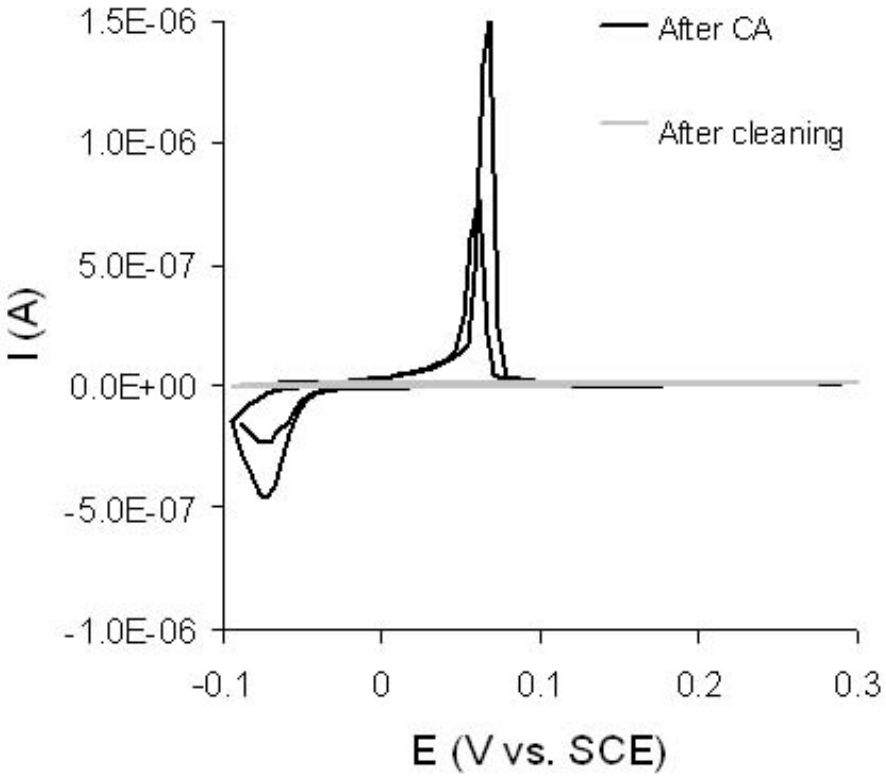

Figure 28. Cyclic voltammograms of clean tris buffer (pH 9) after fixed potential was applied in concentrated PAP solution

5.1.3 The Effect of pH

The reversibility of the PAP/PQI redox couple was measured in phosphate buffer under pHs between 6.5 to 9.0. Reversibility is calculated by dividing the cathodic peak current by the anodic peak current. Figure 29 shows the pH-dependency of PAP/PQI reaction obtained by CVs of PAP at a conventional platinum disk electrode. In more acidic solutions, PQI reacts with hydrogen ion disrupting the electrochemical reversibility of the redox couple[45]. The reversibility peaks at 95% ± 0.4% with a buffer of pH 7.5 and then decreases to 89% ± 0.3% at pH 9.0. This decrease could be attributed to electrodeposition upon oxidation of PAP in basic solutions.

The result of experiments with disk electrode was confirmed with IDA electrodes. Figure 30 is the CV for 1 mM PAP in a phosphate buffer solution at pH 7.5 on an IDA electrode. The peak potentials for the CV are approximately 0.06 V for oxidation and -0.02 V for reduction, which gives an E°' = 0.02 V vs. Ag/AgCl. The peaks for oxidation and reduction show that the reaction is reversible or quasi-reversible because they are balance with similar heights.

Figure 31 contains the CVs of ferricyanide ion before and after experiments with 1 mM PAP solution under pH 7.5. The two curves are identical and the electrode maintained its performance. It can be presumed that perceibable electrodeposition does not occur in neutral condition. Thus, PAP/PQI redox couple is believed to have favorable redox cycling efficiency at pH 7.5.

In addition to increased redox cycling efficiency, PAP is more stable under neutral pH than alkaline pH, because PAP undergoes autoxidation in alkaline condition[46].

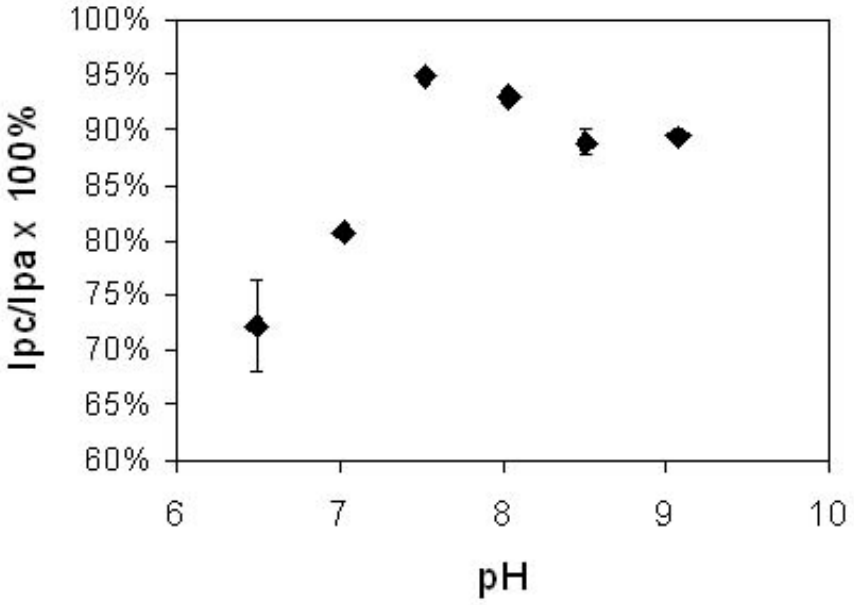

Figure 29. pH dependency of PAP/PQI reversibility

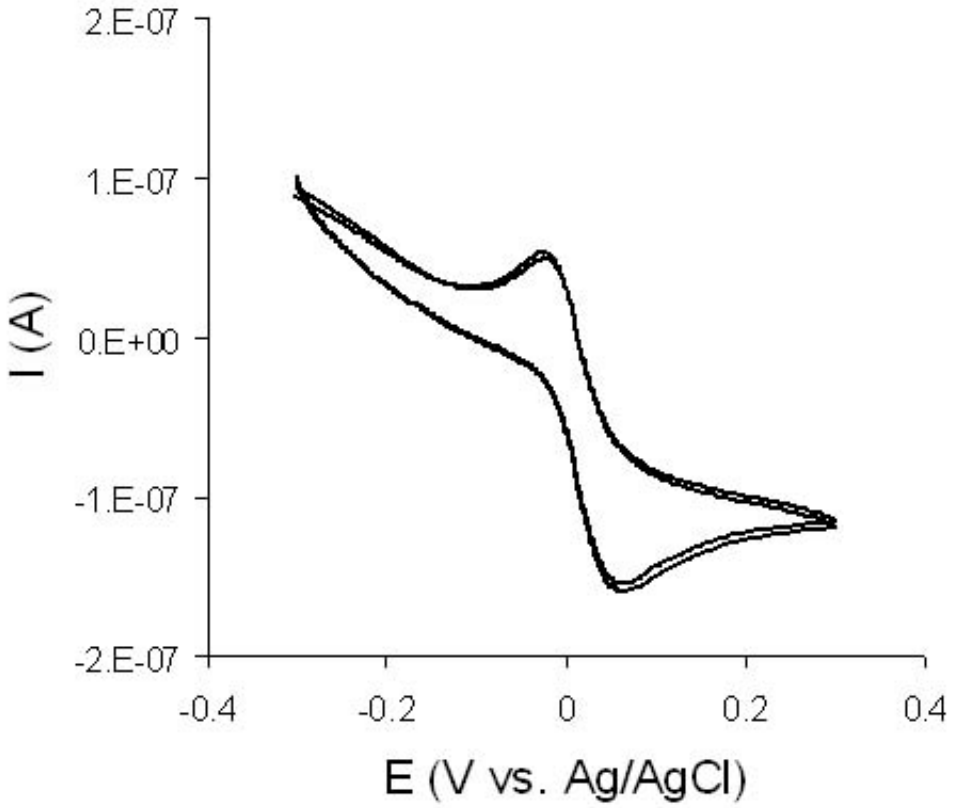

Figure 30. Cyclic voltammograms of 1 mM PAP in phosphate buffer (pH 7.5)

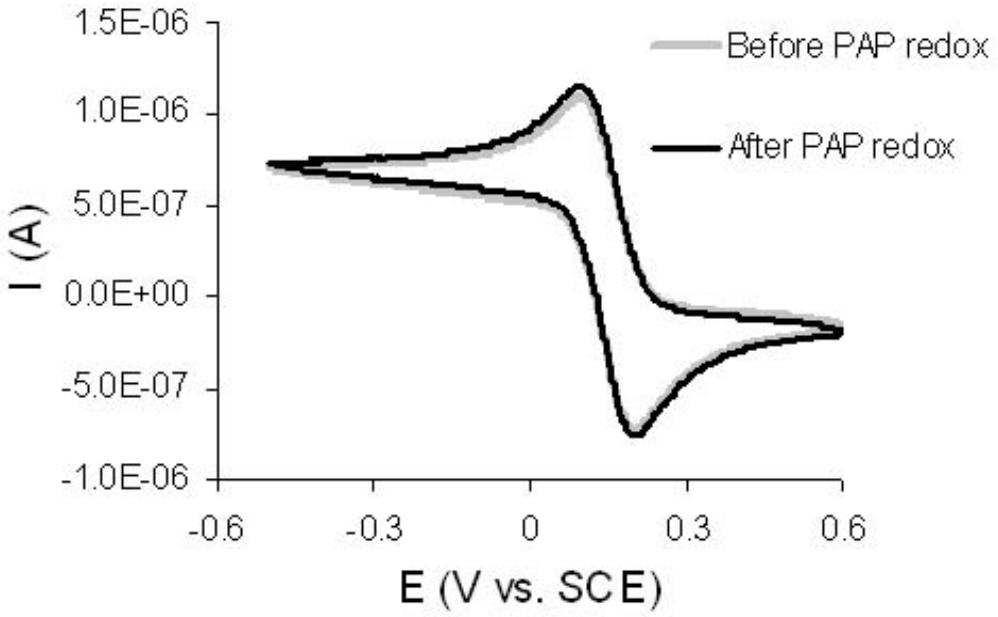

Figure 31. Cyclic voltammograms of 10 mM $Fe(CN)_6^{3-}$ in phosphate buffer (pH 7.5) Before and after experiments with PAP at pH 7.5

5.1.4 Dual Mode CV and CA

CV and CA for PAP were performed at pH 7.5 in dual mode with coplanar IDA electrodes whose gap between fingers was 1.6 μm. First, dual mode CV was used to optimize the potential for the collecting electrode, Ec. Potential of generator, Eg, was cycled between -0.2 V and 0.4 V while Ec was held at –0.1, -0.2, and -0.3 V, as seen in figure 32. The generator's limiting current, measured at +0.4 V, increased as more negative potential were applied to Ec.

The collection efficiency is the ratio of the collecting current for PQI reduction to the generating current for PAP oxidation current. As the collection efficiency gets close to 1, the redox format approaches to an ideal one. The collecting efficiency of figure improved from 70 % and Ec = -0.1 V to 87 % and Ec = -0.3 V. The percentages are calculated by dividing the collector's limiting current by the generator's limiting current.

The single mode CV for PAP showed that E°' = 0.02 V vs. Ag/AgCl at pH 7.5. For a completely reversible system, it would be expected that the maximum limiting current would occur with applied potentials beyond 0.11V and -0.07 V, as governed by the Nernst equation for a 2-electron system and for 99.9% conversion to either the reduced or oxidized specie (i.e. E°' ± 90 mV). Real electrodes required more polarization than theory would predict for a reversible couple. This can be explained by an incompletely reversible redox couple.

The background signal interfered significantly at potentials more negative than -300 mV as dissolved $O_{2(g)}$ was reduced on Pt electrodes. Eg cannot go beyond 0.3 V due the interference of enzyme substrates. Thus, Ec was held at -0.3 V and Eg was maintained at 0.29 V. For dual mode chronoamperometry (CA) experiments

The current was stabilized in a few seconds in dual mode CA attaining a steady state. It can be compared to a theoretical diffusion-controlled limiting current as done in chapter 4 for ferri/ferro cyanide couple. The band width is 2.4 μm, the gap is 1.6 μm, and the diffusion constant is 1.1×10^{-5} cm^2/s on this occasion. The theoretical current for a solution of 1 mM PAP was 1.6 μA and the observed current was 1.0 μA. Thus, the experimental limiting current is 63 % of the theoretical limiting current for PAP whereas the ratio was 90 % for ferricyanide ion. It is interpreted that the experiments of PAP are not carried out under a rigorous diffusion-limited condition due to the incomplete reversibility of PAP/PQI couple.

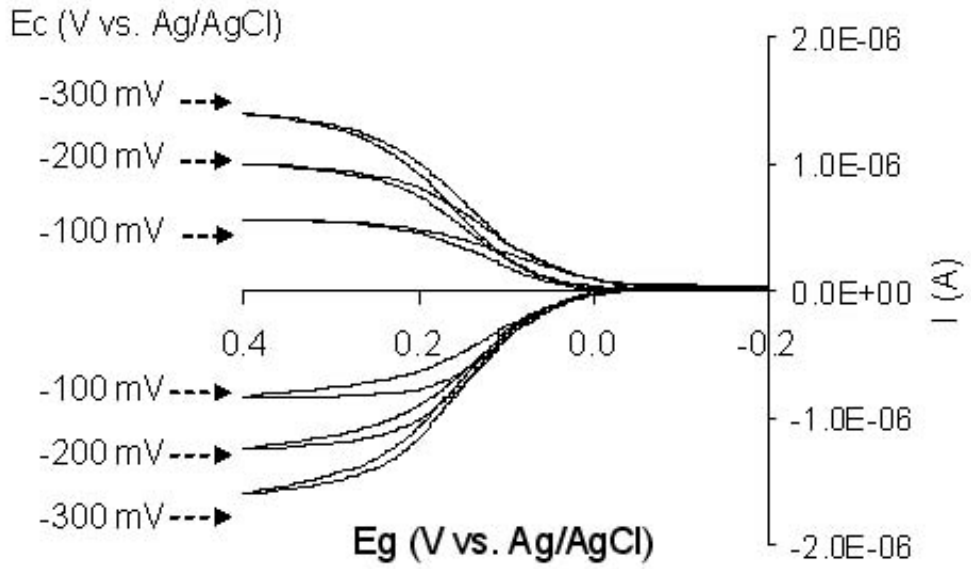

Figure 32. Dual mode cyclic voltammogram for 1 mM PAP in a phosphate buffer at pH 7.5 with varied collecting electrode potential.

5.1.5 PAP Calibration Curve

Chronoamperometry was used for calibration because the continuous oxidation of PAP generated by the enzyme on the immunoassay sandwich was monitored with chronoamperometry. It was also possible to use CV, however, CV would measure the limiting current at much wider time intervals. Figure 33 compares the single mode and dual mode of IDA electrodes. The limit of detections was calculated for each mode using 3 times standard deviation of background current; for single mode, 1.04×10^{-5} M; for dual mode (generator), 1.91×10^{-6} M; for dual mode (collector), 1.38×10^{-5} M. In terms of analytical capability, dual mode is about 6 times better than single mode. A calibration curve of log [PAP concentration] versus log [generating current] produced a linear relationship, $y = (1.01 \pm 0.03)\ x\ - (2.88 \pm 0.20)$, $R^2 = 0.984$, between 10^{-3} M PAP and 10^{-6} M PAP. The limit of detection for collector electrode is fairly high since the collecting current has high background current resulted from O_2 reduction.

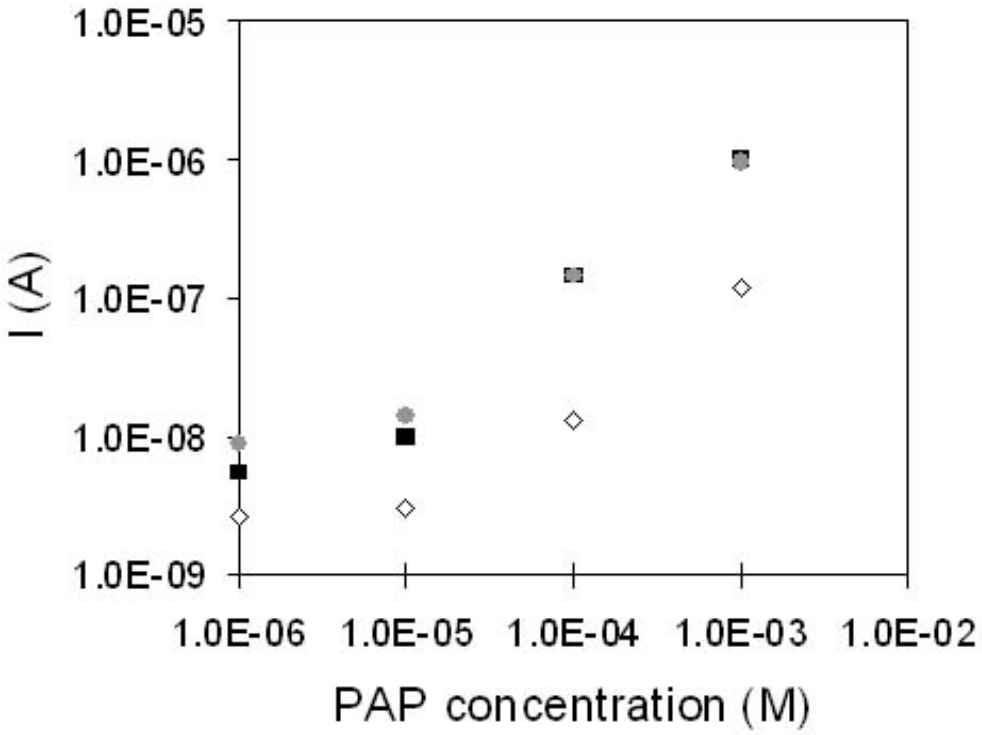

Figure 33. Calibration curves of PAP with single mode (◇), dual mode at the generator (■), and dual mode at the collector (●).

5.2 β-Galactosidase as an Enzyme Label

Formerly, we used alkaline phosphatase (ALP) as the enzyme label which used PAPP as the enzyme substrate. This enzyme generates PAP at pH 9.0, which is not proper for redox cycling with an IDA electrode. Therefore, β-galactosidase (β-gal) was substituted as the enzyme label as it shows maximum catalytic function under neutral pH. 4-aminophenyl β-D-galactopyranoside (PAPG) is the enzyme substrate from which β-gal produces PAP. β-Gal (M.W. = 460 kD) is bigger than ALP (M.W. = 140 kD) in size but has a comparable turnover number and stability. Figure 35 illustrates the concept of electrochemical immunoassay with β-Gal. The enzyme was bound to the surface of microbeads not the electrodes to facilitate redox cycling.

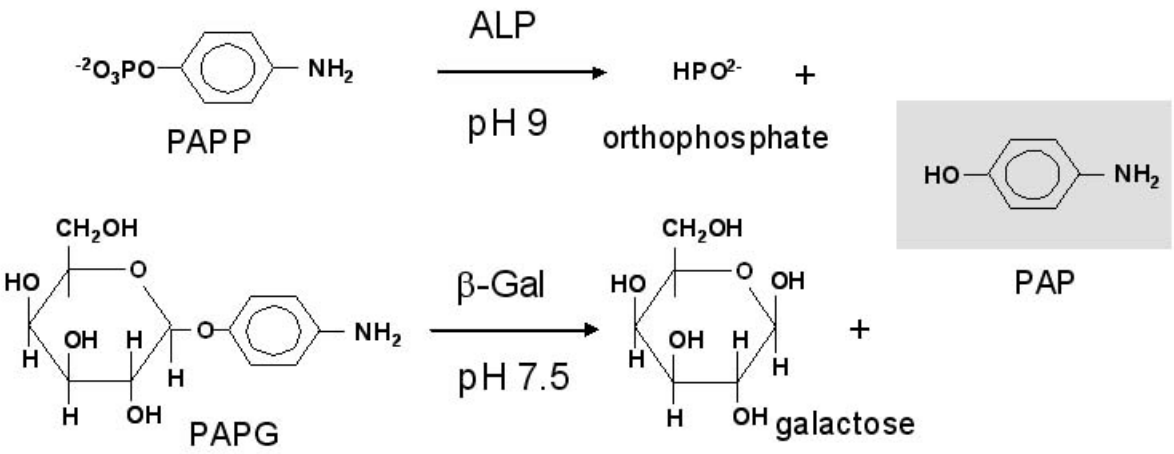

Figure 34. Enzyme reactions of alkaline phosphate (ALP) and β-galactosidase (β-Gal) generating PAP

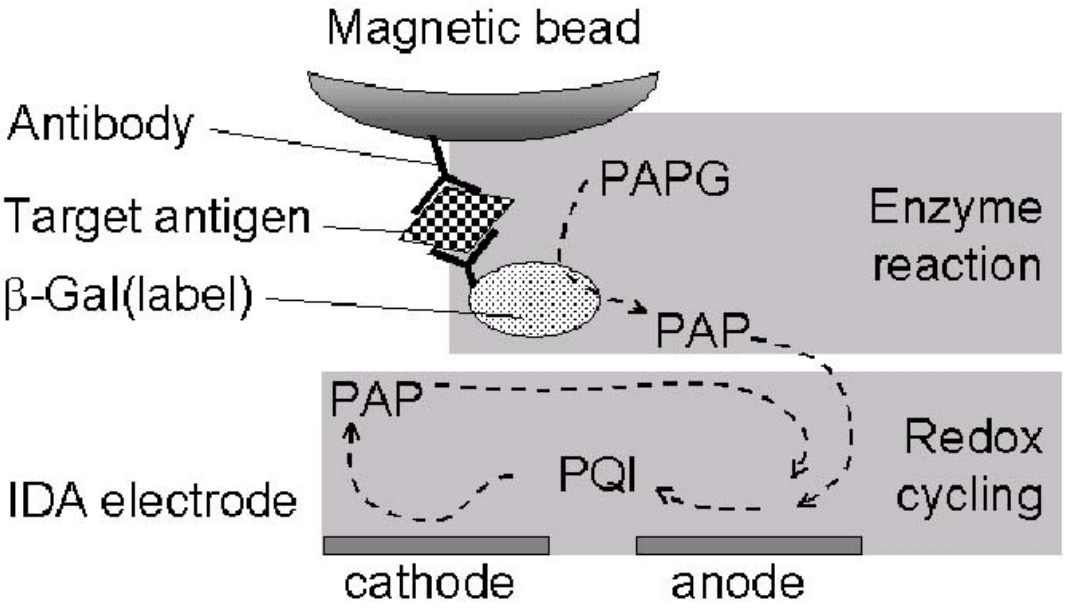

Figure 35. Analytical concept of the electrochemical immunoassay with β-galactosidase

5.2.1 Immobilization of β-Galactosidase on Microbeads

The paramagnetic microbeads, Dynabeads M-280 streptavidine, hold approximately 7×10^5 streptavidin molecules per bead[47]. Streptavidine (M.W. = 60 kD) has four biotin binding sites per molecule. The surface is readily functionalized with biotinylated molecules by the biotin-avidin coupling. Biotinylated β-galactosidase (β-Gal) was used to immobilize the enzyme on the surface of microbeads.

Quantitative analysis of immobilization was carried out through fluorescence measurements of 4-methylumbelliferone (4-MU). Esters of 4-MU do not fluoresce unless cleaved to release the fluorophore. Cleavage of 4-methylumbelliferyl galactoside (4-MUG) by β-Gal enzyme yields the fluorescent molecule 4-MU that emits light at 460 nm when excited by 365 nm light.

A bead suspension solution of 2.5 μL (1.7×10^6 beads) was incubated with different amount of β-Gal (more details of incubation will be described later) while the biotinylated enzymes bind to the streptavidine on the beads. The enzyme bound beads were injected to the vial containing substrate solution (3.4 mM 4-MUG at pH 7) and the enzyme reaction proceeded for 3 minutes. The reaction was stopped by adding alkaline buffer to the reaction vial. The solution after the enzyme reaction was transferred to a cuvette and the fluorescence was measured with PTI Model C60 Steady-State Spectrofluorometer using a xenon arc lamp source and a photomultiplier. Figure 36 is a fluorescence spectrum for a solution of enzyme reaction, which shows maximum emission at 450 nm. The background signal was obtained with 3.4 mM 4-MUG solution which shows no fluorescence around 450 nm.

The fluorescence was proportional to the amount of enzyme added to the bead and, at a juncture, the signal stopped increasing with additional enzyme, as seen in figure 37. It means that the beads were saturated with the enzyme and could not carry more enzyme to the reaction vial. The point of change was 2 pmoles of β-Gal for 1.7×10^6 beads which corresponds to 1.0 enzyme/streptavidin. Since a streptavidine has 4 biotin binding sites, 25 % of available sites are presumed to be occupied with β-Gal. This is most likely due to the steric hindrance between enzymes. The molecular weight of β-Gal is 465 kD which is about 7.5 times larger than streptavidine's.

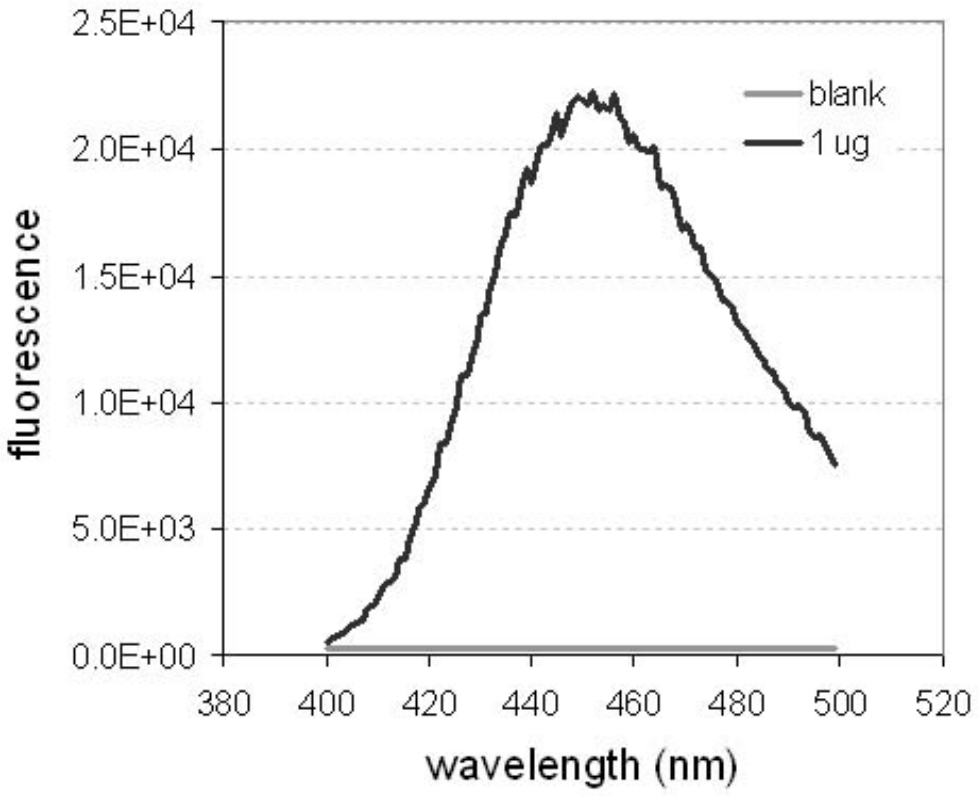

Figure 36. Fluorescence spectrum of 4-MU produced by enzyme reaction of β-Gal. Grey line is background signal.

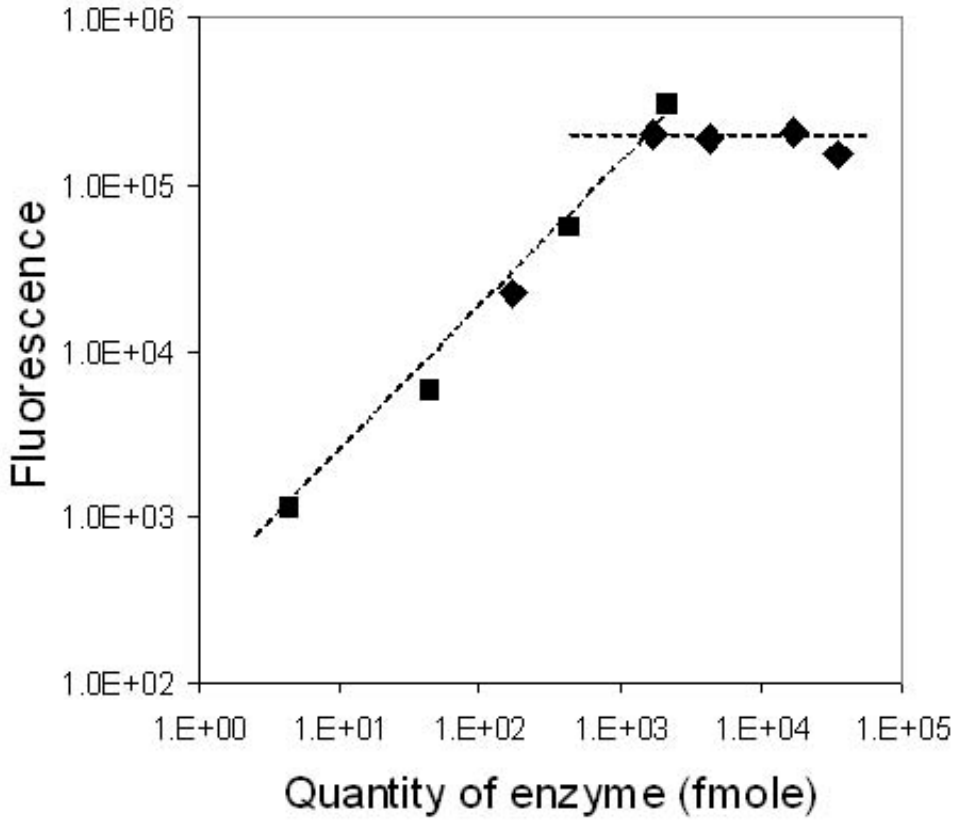

Figure 37. Saturation curve of enzyme binding by the fluorescence measurement. 2.5 μL of bead suspension (1.7×10^6 beads) was used

5.2.2 Experiments with a Rotating Disk Electrode

The binding characteristics of β-Gal was verified with electrochemical experiments using a rotating disk electrode (details are given in Section 5.2.1). PAP was generated from PAPG with varied amount of enzyme bound to microbeads which were prepared as in the fluorescence experiment.

The experiments were done with an MF-2067 3 mm diameter platinum electrode from Bioanayltical Systems, Inc., a saturated Miniature Teflon® Ag/AgCl reference electrode (Cypress Systems, Inc., Lawrence, KS), and a platinum wire auxiliary. Amperometric detection was done at an applied potential of +290 mV vs. Ag/AgCl and a rotation rate of 3000 rpm. A 30 μL drop of 5.3 mM PAPG in phosphate buffer (pH 7.5) was laid and the potential was applied to the electrode spinning at 3000 rpm. After a 15 second's quiet time, the current measured to establish a background slope. At 30 second, 10 μL of enzyme bound bead suspension were added to the drop. The run terminated after 70 seconds. The slope between 50 and 70 seconds was corrected by subtracting the background slope, taken between 15 and 25 seconds, to give the average slope.

Figure 38 shows that enzyme bound to beads increases proportionally with added enzyme during incubation before the saturation point. The point of saturation in figure corresponds to 21 % occupation by β-Gal which agrees with the result of fluorescence measurement.

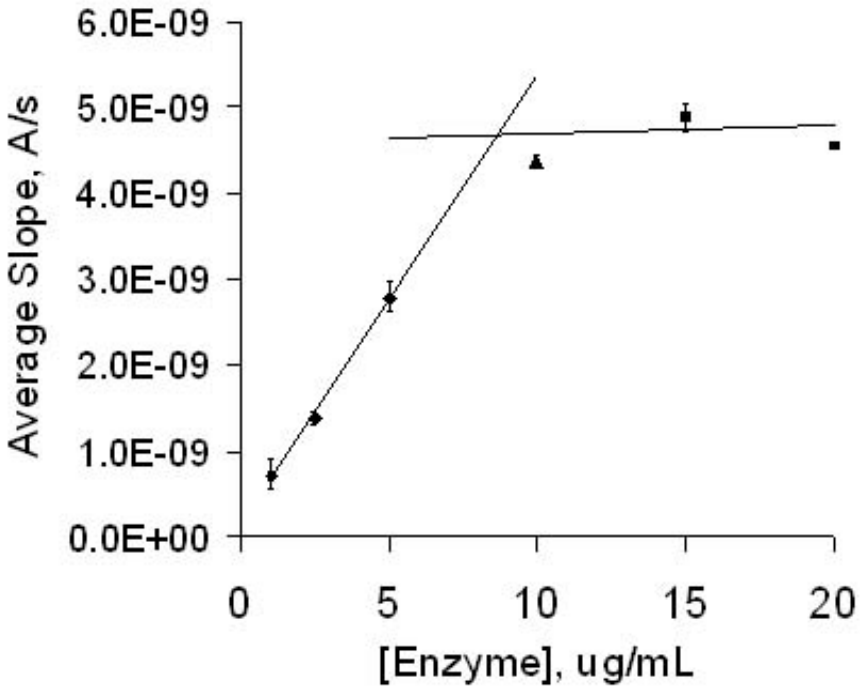

Figure 38. Saturation curve from the experiment with a rotating disk electrode

5.3 Immunoassay with Coplanar IDA Electrodes

5.3.1 Materials and Methods

$K_3Fe(CN)_6$ was from J.T. Baker Chemical Co. (Phillipsburg, NJ). Biotinylated β-galactosidase, 4-aminophenol (PAP), and 4-aminophenyl β-D-galactopyranoside (PAPG) were from Sigma-Aldrich (St. Louis, MO). Tween-20, NaH_2PO_4, Na_2HPO_4, KCl, $MgCl_2$, NaN_3, and NaOH were from Fisher Scientific (Fair Lawn, NJ). Bovine serum albumin (BSA) fraction V powder (98+% pure) was from Boehringer Mannheim (Indianapolis, IN). Streptavidin-coated M-280 Dyanbeads, 6.7 x 10^8 beads/ ml, with 2.8 μm diameter were from Dynal (Great Neck, NY). Biotinylated sheep anti-mouse IgG $F(ab')_2$ and Chrompure mouse IgG, whole molecule, were from Jackson Immunoresearch Laboratories, Inc. (West Grove, PA). Rabbit anti-mouse IgG (H+L) conjugated to β-galactosidase was from American Qualex Antibodies (San Clemente, CA). Neodymium-Iron-Boron rare earth magnets were from Radio Shack (Fort Worth, TX).

Buffer A consisted of 0.044 M NaH_2PO_4, 0.056 M Na_2HPO_4, 0.1 M KCl, 0.003 M NaN_3, 1% BSA and 0.5% (v/v) Tween-20 in deionized water. Buffer B consisted of 0.044 M NaH_2PO_4, 0.056 Na_2HPO_4, 0.1 M KCl, 0.01 M $MgCl_2$, and 0.003 M NaN_3 dissolved in deionized water. Both buffers were adjusted to pH 7.4 with concentrated NaOH.

The platinum electrodes of the IDA have 1.6 μm gaps between 2.4 μm wide legs were used for the immunoassay. The IDA electrode experiments included a 0.015 in. diameter Ag/AgCl wire from A-M Systems, Inc. (Carlsborg, WA) as the reference electrode and a platinum wire as the auxiliary electrode. A small polystyrene Pour-Boat

Weighing Boat from VWR Scientific, Inc. (West Chester, PA) contained the electrochemical cell. A CH Instruments 832A Electrochemical Analyzer was used as the bipotentiostat for IDA experiments.

5.3.2 Experimental Setup

To monitor the enzyme product PAP as it was produced with maximum sensitivity, it was necessary to minimize its dilution by minimizing the volume of the reaction solution. In order to do this, we made measurements on a single drop of solution. The experimental setup is illustrated in Figure 39. The IDA electrode was held upright in a polystyrene weighing boat with a ring stand and clamp. Then, 10 – 20 μL of reaction solution were pipetted at the base of the electrode, forming a drop as a result of the hydrophobic surface of the weighing boat and the surface tension of the buffer. The drop was sufficiently tall to cover the electrode sensing area, 2 mm above the bottom of the boat. Then, a magnet was positioned beneath the boat and in front of the electrode to hold the protein-coated microbeads in a mound slightly away from the electrode surface. Bead distance from the IDA ranged from 1.7 mm to 3 mm. Positioning the beads immediately adjacent to the electrode surface could have reduced the diffusional distance for PAP generated at the beads to travel to the electrode. Under this configuration, however, the electrode signal was reduced considerably by the protein on the beads sticking to the IDA electrodes.

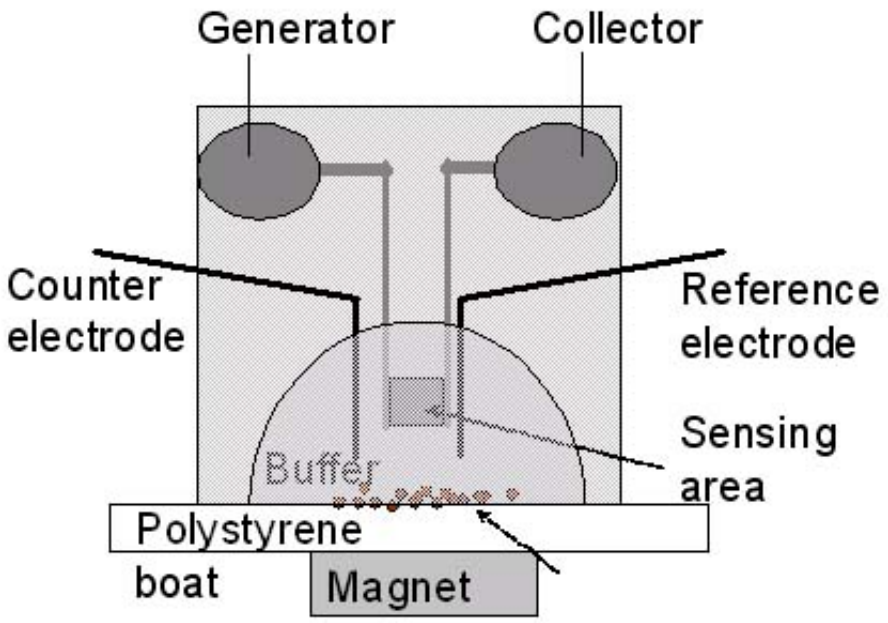

Figure 39. Experimental setup for immunoassay with a coplanar IDA electrode

5.3.3 Minimum Detectable Number of Beads

Dynabeads were modified in a glass test tube by mixing 30 μL of beads with 150 μL of biotinylated β-galactosidase diluted to 60 μg/mL with Buffer A. The amount of β-galactosidase is about 10 times of the quantity required for saturation of microbeads used. The mixture was shaken gently on a vortex for 30 min. Unreacted biotinylated β-galactosidase was removed with 3 washes each of 100 μL Buffer A followed by 3 washes each of 100 μL Buffer B. Wash steps involved placing a magnet beneath the test tube to hold the beads against the test tube wall before removing fluid with a pipet. The enzyme saturated beads were resuspended in 320 μL of Buffer B.

Dual electrode chronoamperometry was used to detect the production of PAP. One set of electrode fingers was held at E = +290 mV and the other at E = -300 mV. At 0 s, a 10 μL drop of 8 mM PAPG was placed on the electrode surface. At 30 s, 10 μL of bead solution was added to the drop.

Figure 40 shows the change in current with time with a varying number of beads in the microdrop. The potentials were applied at 0 s, the background signal for PAPG in buffer stabilized, and then the beads were added at 30 s. When PAP reached a detectable concentration, increasing anodic current was observed. A linear range was established in a 20 μL drop for log [number of beads], between $6.3x10^2$ and $6.3x10^5$ beads, and log [change in generator current with time] between 300 and 330 s with $R^2 = 0.995$. The limit of detection was determined by 3 times the standard deviation of the blank signal, and it was 1000 beads in the 20 μL drop or 50,000 beads per mL.

With high number of beads, the slope decreases approximately 150 s after the observable signal appears. After 300 sec of 6.3×10^5 beads incubating with PAPG, the

PAPG concentration decreases by only 0.5 mM leaving a concentration that is still 10 times the Km value. However, substrate can be locally depleted to change the kinetics of the enzyme reaction, which might explain the change in slope. This process did not interfere with the results as they were obtained before the change of slope occurs.

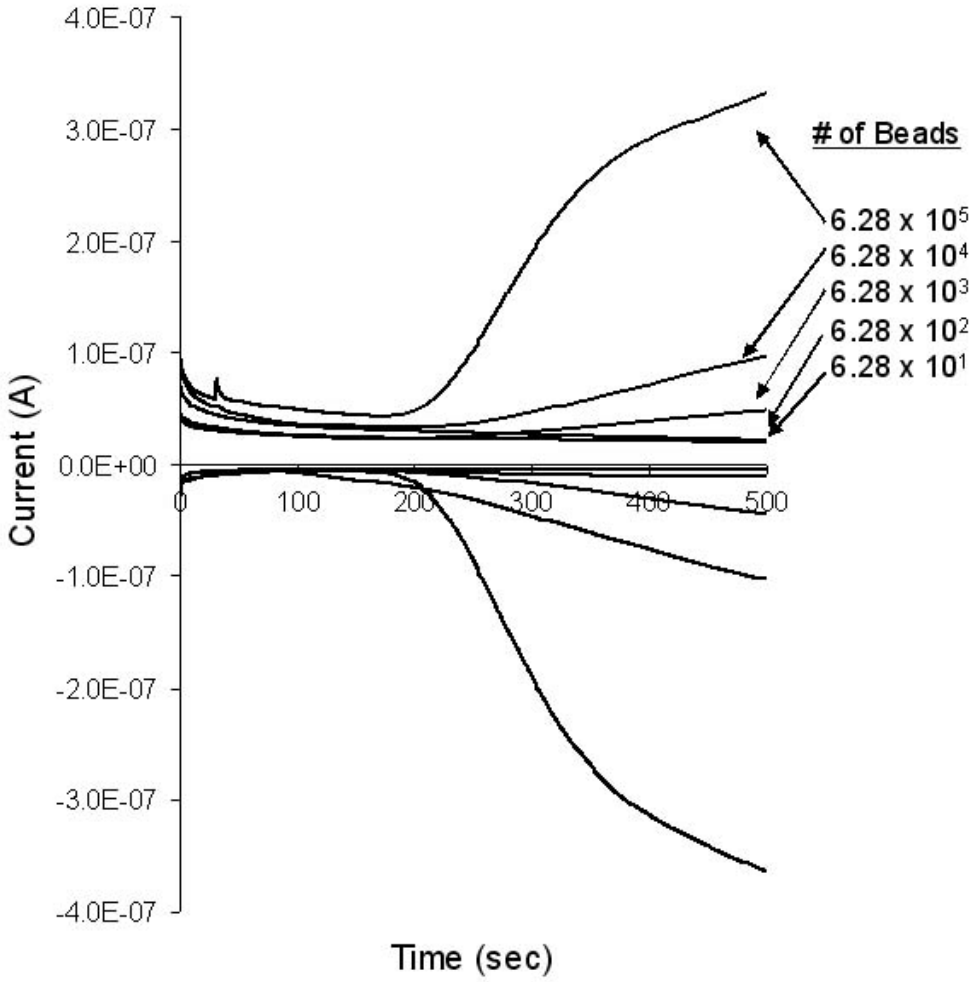

Figure 40. Current vs. time for varied number of beads with coplanar IDA electrode

5.3.4 Mouse IgG Immunoassay

A practical ECIA with IDA electrodes was demonstrated with mouse IgG. Beads were functionalized with the immunoassay sandwich in a vessel separate from the electrochemical cell.

Dynabeads of in 50 μL suspension ($3.4x10^7$ beads) were mixed with 50 μL of biotinylated sheep anti-mouse IgG diluted to 40 μg/mL with Buffer A in a glass test tube. The mixture was incubated for 30 min with gentle shaking to facilitate binding of biotinylated antibody to the beads. Excess biotinylated sheep anti-mouse IgG was removed with 3 washes each of 100 μL Buffer A. A magnet helped to keep the beads in the tube when the washing buffer was drained. Then, beads were resuspended in 100 μL Buffer A and 10 μL aliquots were transferred into 8 fresh test tubes. Varying concentrations of mouse IgG in Buffer A were added to each test tube to make 20 μL of final mouse IgG concentrations between 10 and 1000 ng/mL. A blank sample consisted of 10 μL of Buffer A instead of mouse IgG to determine the extent of non-specific adsorption. The tubes were shaken gently for 30 min. Buffer A washed the beads 3 times as previously described and then resuspended in 10 μL Buffer A. Then, 10 μL of rabbit anti-mouse IgG conjugated to β-galactosidase diluted to 40 μg/mL with Buffer A were added to each test tube and shaken gently for 20 min. Beads were washed 3 times with Buffer A, washed 3 times with Buffer B, and then resuspended in 40 μL of Buffer B.

Dual electrode chronoamperometry was used for detection. One set of electrode fingers was held at E = +290 mV and the other at E = -300 mV. At 0 s, a 10 μL drop of 8 mM PAPG was placed on the electrode surface, and 10 μL of bead solution was added

to the drop at 200 s. Each mouse IgG standard was done in duplicate and the average response was used for the immunoassay calibration curve.

The increasing anodic current reflected PAP production from the immunoassay sandwich, as seen in Figure 41. A log-log calibration curve of change in current with time (between 450 and 500 s) versus mouse IgG concentration gave a linear relationship, $y = 0.96x - 1.87$, $R^2 = 0.987$, between 50 and 1000 ng/mL mouse IgG. The theoretical detection limit of the assay was 26 ng/mL mouse IgG or 3.5×10^{-15} mol mouse IgG, as determined by three times the standard deviation of the signal obtained with beads exposed to all reagents except mouse IgG. The 50 ng/mL mouse IgG sample was the lowest concentration detected. The theoretical detection limit of the electrochemical setup, as determined by three times the standard deviation of the signal for PAPG, was 0.6 ng/mL mouse IgG or 7.2×10^{-16} mol mouse IgG, indicating that the detection limit of the immunoassay is limited by non-specific adsorption rather than by the IDA detection limit for PAP.

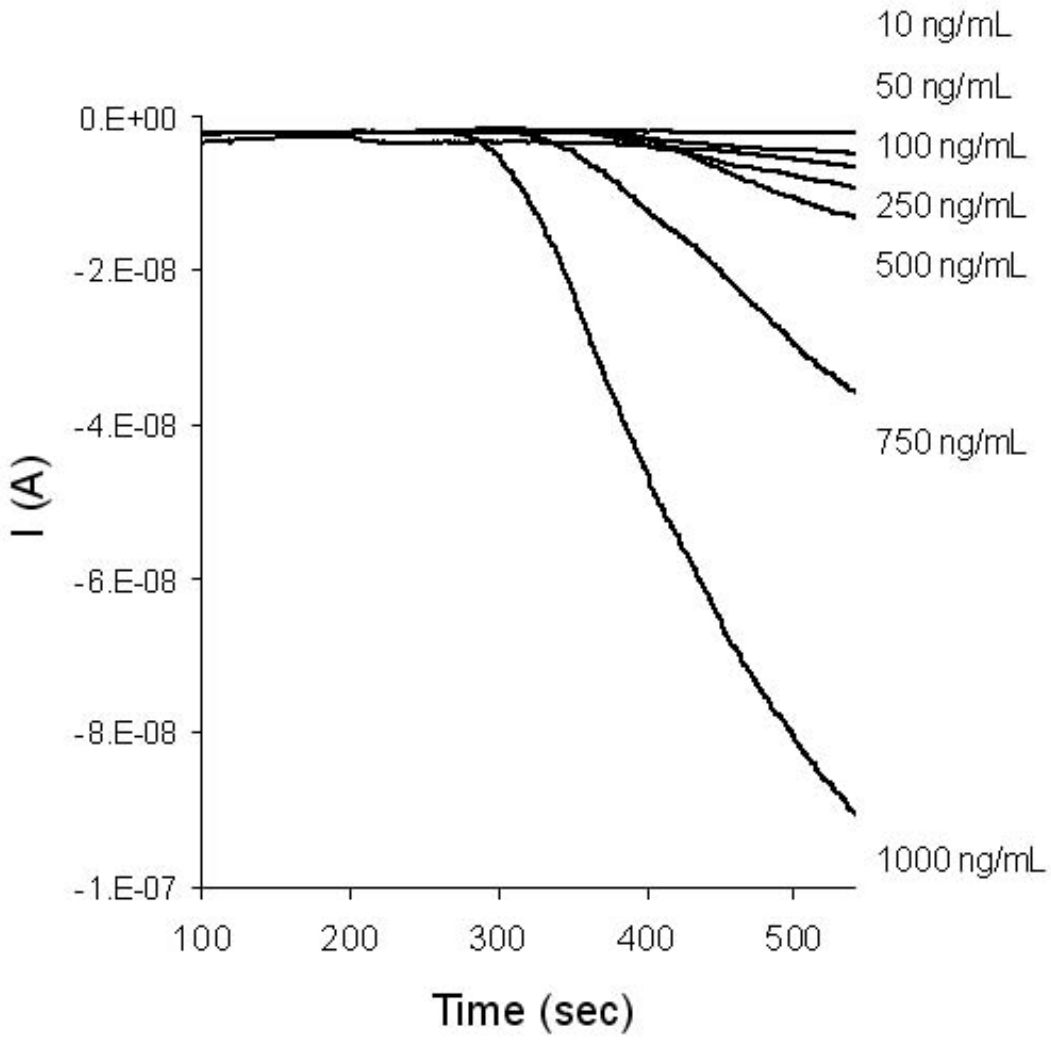

Figure 41. Chronoamperometry with mouse IgG standards

5.4 Comb IDA Electrodes for Microbead-Based Immunoassay

5.4.1 Horizontal Configuration of the Experiment

In the assays with coplanar IDA electrodes the current started increasing about 3 minutes after the enzyme injected into the run. It is due to the time consuming diffusion of PAP from the beads to the sensing area. One can generate a mechanical convection in the drop to shorten the lag time. Micro-rotating disk electrode was investigated for this reason[48]. However, the system is complicated to miniaturize and the sensitivity was worse than the coplanar IDA electrode.

An alternate experimental configuration is to place enzyme-coated beads on the electrode surface. This horizontal configuration was avoided due to the possibility of electrode fouling from the proteins coated on the beads[49]. However, the surface of the electrode is buried inside the trenches in comb IDA electrodes. When the width of trenches is smaller than the size of microbeads, most of the electrode surface is kept intact during the assay.

The horizontal configuration with comb IDA electrode is illustrated in figure 42. Using a smaller magnet (diameter 1.5 mm) the microbeads sat on the sensing area of the comb IDA electrodes. Since most of the electrode surface is inside the trenches, the beads were placed near the electrode but not in direct contact. The diameter of the magnetic beads (2.8 μm) was slightly bigger than the width of trenches (2.4 μm) so that most of the microbeads were positioned on top of the trenches rather than inside them. As a result, the distance between the beads and the electrode surface could be reduced to a

few micrometers, which is important in a quiescent solution since the proximity of the enzyme and electrode has a significant effect on response time and sensitivity.

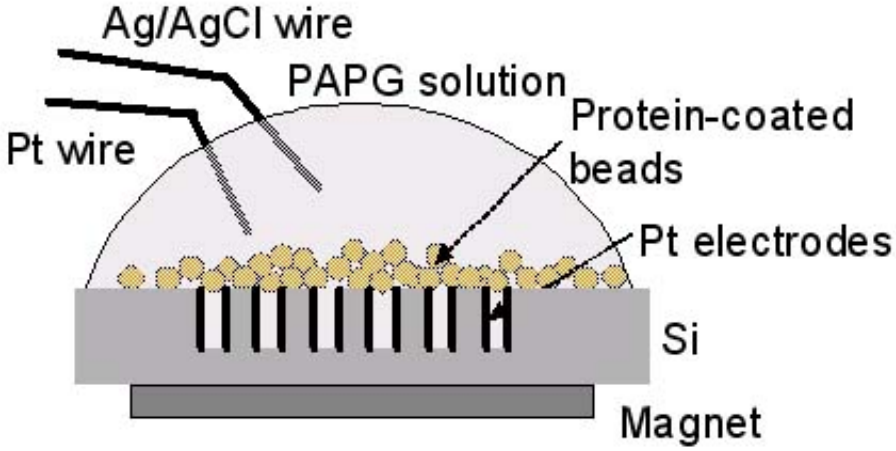

Figure 42. Experimental setup for immunoassay with a comb IDA electrode

5.4.2 Current Response vs. Time

In order to compare the performance, minimum detectable number of beads was obtained using a comb IDA electrode with 2.5 μm gap. The experimental procedure was the same as described previously for the coplanar IDA electrodes.

The responses are compared in Figure 43. A change in current was not observed with coplanar IDAs until 200 seconds into the run, which is attributed to the time for PAP, generated at the beads' surfaces, to diffuse to the electrode sensing area and be accumulated to a detectable concentration. In this case, we measured the concentration change of the PAP in the bulk solution. However, in the bead-on-electrode format, the current increased much faster after adding the beads, increasing very rapidly at first, and then slowing down to a plateau in 100 sec. Since the distance between the beads and the electrode is only a few micrometers, the enzyme product (PAP) was detected essentially instantaneously. As the concentration of PAP increases at the sensor, PAP diffuses out to the bulk and this loss is balanced by PAP generated by the enzyme reaction. Both increasing rate and steady-state current were proportional to the quantity of enzyme (i.e. # of beads). A current increase, I, of 2 nA was clearly detected, with 140 beads in 60 sec.

The plot of log [slope of generator current] and log [current increase] were constructed versus log [number of beads], as seen in figure 44. Here, the background current for the experimental solution was stabilized at 4.5 nA and standard deviation of current increasing rate was 7.7×10^{-11} A/s. The minimum number of detectable beads that was estimated based upon 3 times of STD of the baseline noise in the system was 60. The quantity of enzyme is determined as follows:

$$C_{enzyme} = 60 \times 7.1 \times 10^{5} / 6.02 \times 10^{23} = 70 \text{ amole}$$

A detection limit of 70 amole of β-galactosidase is about 1/20 of the detection limit in the previous experimental setup.

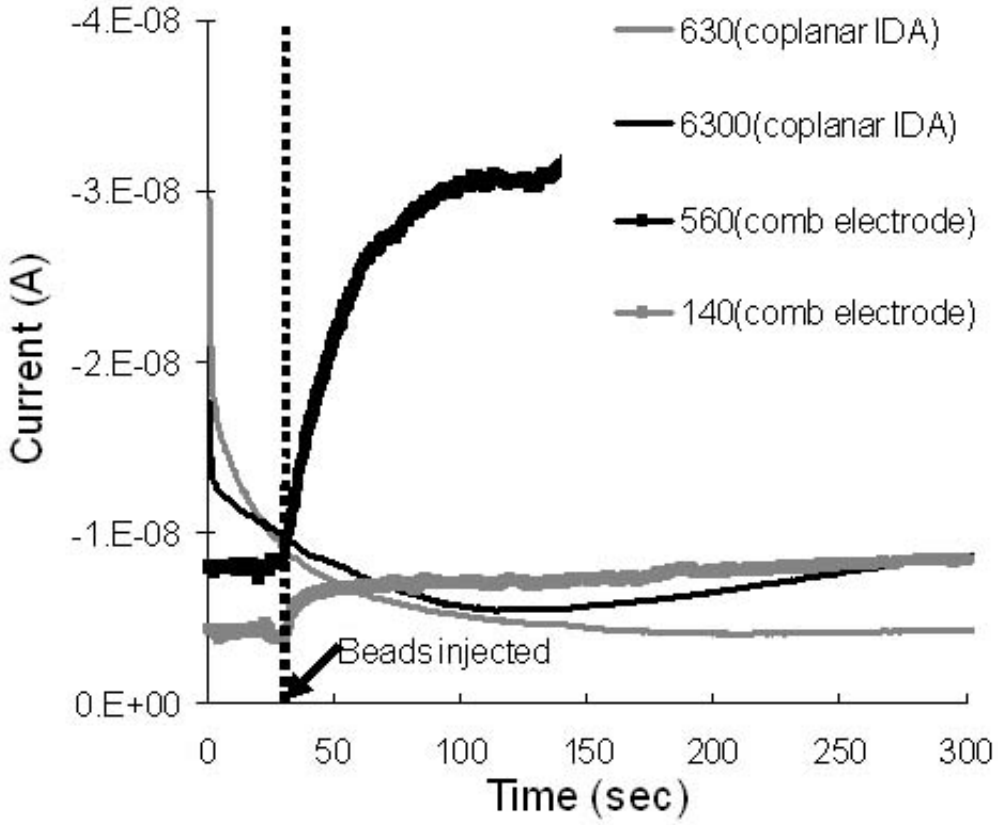

Figure 43. Comparison of coplanar and comb IDA electrodes in terms of response time and sensitivity.

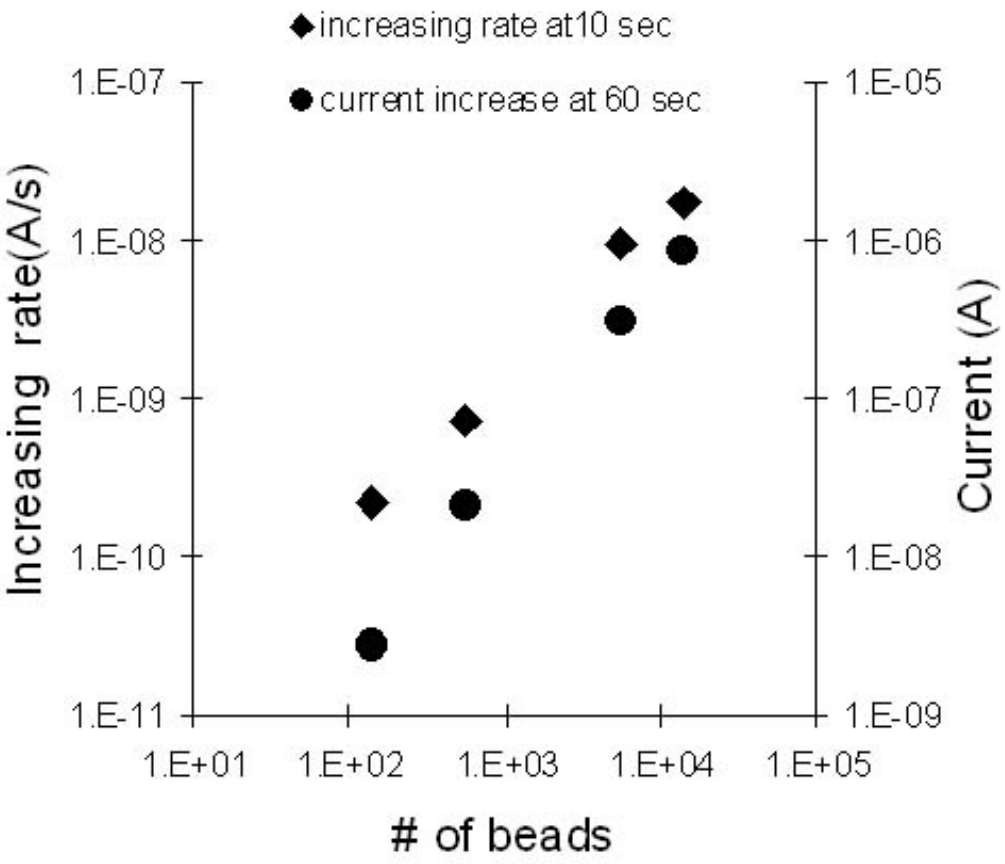

Figure 44. Response vs. number of beads with comb IDA electrode

5.5 Reproducibility

The 50 ng/mL mouse IgG standard was run in triplicate with a coplanar IDA electrode, and the relative standard deviation was 10%. In case of comb IDA, 130 enzyme-saturated beads were measured three times and the relative standard deviation was 9 %. However, some points in the calibration curves were obtained after several runs due to their significant error range. With the current experimental design, there are several issues that affect reproducibility.

First, functionalized beads are transferred manually from the reaction vessel to the detection solution. The density of the beads exceeds significantly that of the buffer, and they tend to settle out of solution. Therefore, transferring a reproducible number of beads into the detection solution depends on how homogeneously the beads are dispersed throughout the solution in the reaction vessel.

Second, variability in the position of the electrode with respect to the magnet alters the time within which the enzyme reaction is detected. In experiments with coplanar IDA electrodes, the electrode's position dictates the distance that PAP generated on the beads' surfaces must diffuse to the electrode surface. At a maximum, the beads were 3 mm away from the electrode sensing area, considering the distance from the far edge of the magnet to the top of the electrode sensing area. A signal started within 200 seconds of injecting beads into the enzyme substrate solution. With a diffusion coefficient for PAP of 1.1×10^{-5} cm^2/s, this corresponds to beads being only 670 μm from the electrode sensing area, as determined by the Einstein equation:

$$t = l^2/2D$$

where D is diffusion coefficient, l is length, and t is time. The discrepancy in distance can be explained partially by the enzymatic production of PAP occurring as the beads traversed the microdrop before settling over the magnet. Non-recognizable agitation caused by the environmental vibration will expedite the migration of PAP too.

Then, manually pipetting the beads into the detection drop introduces variability. PAP generation begins as soon as functionalized beads are exposed to the enzyme substrate. Beads floating through the drop rather than lying on the magnet are more accessible to substrate, and, therefore, more PAP can be generated.

Finally, the distribution of beads over the magnet varies. Occasionally, beads would clump over the magnet, minimizing the exposed surface area. At other times, beads would spread out over the circumference of the magnet, which increased the exposed surface area of the bead. With clumps of beads, the substrate around the beads are depleted quickly and the enzyme can produce less amount of PAP. Especially with comb IDA electrodes, slight variation of injection resulted in significant changes since the size of magnet is smaller.

None of both experimental setups, vertical and horizontal configurations, are ideal in terms of reproducibility. Incorporating the IDA electrode into an automated fluidic system would improve the procedure by removing the variability associated with manual pipetting and with positioning the beads relative to electrode. Next two chapters are on a bead-based immunoassay with the IDA sensors in a fluidic channel.

6. MAGNETIC COLLECTOR

Previously, enzyme labeled magnetic bead suspensions were manually pipetted into a substrate solution and subjected to a magnetic field. The repeatability of positioning magnetic beads was left as an issue. A magnetic collector is the most practical solution as previously mentioned. Through a microfluidic channel the functionalized magnetic particles can be delivered in a controlled manner. An integrated magnet applies a magnetic field gradient to the microchannel structure, and the magnetic particles can thus be entrapped at a desired position in the flow stream. Another advantage of this microfabricated device is the possibility of automation and miniaturization of the total assay procedure.

A model for the magnetic field and flow field acting on a magnetic bead was constructed by assuming a uniform magnetic field. The collecting efficiency of a magnetic collector was calculated and compared with a real system.

6.1 Model for a Magnetic Collector

6.1.1 Model for a Magnetic Collector

Considering the force on a magnetic bead, the following equation is obtained from Maxwell equation.

$$\overrightarrow{F_{\text{mag}}} = V\chi_{\text{m}} m(\vec{H}\cdot\nabla)\vec{B}$$

where F_{mag} is the magnetic force on the particle, V is the volume of the particle, χ_{m} is its magnetic susceptibility per unit volume, H is the magnetic field intensity, and B is the magnetic flux density. Since the interactions between the particles are negligible, the z directional magnetic force of attraction from the field on the particle is

$$F_z = V\chi_{\text{m}}\left(H_x\frac{\partial B_z}{\partial x} + H_y\frac{\partial B_z}{\partial y} + H_z\frac{\partial B_z}{\partial z}\right)$$

When the magnet is bigger than the width of channel, the gradient term in z direction ($\partial Bz/\partial z$) dominates others and the equation is simplified into

$$F_z = V\chi_{\text{m}}\frac{B_z}{\mu_o}\frac{\partial B_z}{\partial z} \tag{1}$$

A disk permanent magnet can be considered as an electromagnet with single turn of coil and the corresponding field component is

$$B_z = \frac{\mu_o}{2}(Ia^2)\frac{a^2}{(a^2+z^2)^{\frac{3}{2}}} \tag{2}$$

for the center of the magnet where μ_o is the permeability of free space, I is the equivalent current, and a is the diameter of the coil(ie. magnet).

The magnetic acceleration is balanced with a hydrodynamic drag force in the opposite direction.

$$\overrightarrow{F_{drag}} = 3\pi\eta D\vec{v} \tag{3}$$

where F_{drag} is the drag force on a particle, η is the viscosity of the fluid, D is the diameter of the particle, and v is the relative velocity of the particle. Then, the equation describing the movement in z-direction is

$$\overrightarrow{F_{mag}}(z) + \overrightarrow{F_{drag}}(z) = m\frac{d^2z}{dt^2} \tag{4}$$

While the particle moves to the magnet in z-direction, fluid flow in x-direction carries the particle passing the magnetic field. The particles attracted to the surface in the effective magnetic field can be captured and detected by the sensor. Figure 45 illustrates the forces and movement of the magnetic beads.

The velocity of particles in x-direction is governed by the velocity distribution of viscous flow of the fluid. For steady-state parallel flow through a rectangular tube as shown below (-a≤y≤a, -b≤z≤b), the Navier-Stokes equations becomes

$$\frac{\partial^2 u}{\partial y^2} + \frac{\partial^2 u}{\partial z^2} = \frac{1}{\mu}\cdot\frac{\partial P}{\partial x}$$

From this equation and boundary conditions, the exact flow rate vs. pressure drop relationship, the average flow velocity and the velocity distribution can be obtained as follows.

$$Q = \frac{4ba^3}{3\eta}\left(-\frac{dP}{dx}\right)\left[1 - \frac{192a}{\pi^5 b}\sum_{i=1,3,5\ldots}^{\infty}\frac{\tanh(i\pi b/2a)}{i^5}\right]$$

$$\bar{u} = \frac{4a^2}{3\eta}\left(-\frac{dP}{dx}\right)\left[1 - \frac{192a}{\pi^5 b}\sum_{i=1,3,5\ldots}^{\infty}\frac{\tanh(i\pi b/2a)}{i^5}\right]$$

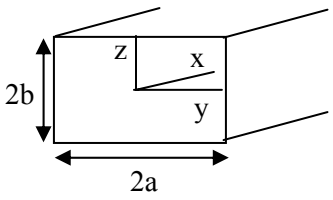

$$u(y,z)=\frac{16a^2}{\eta\pi^3}(-\frac{dP}{dx})\sum_{i=1,3,5...}^{\infty}(-1)^{(i-1)/2}\cdot[1-\frac{\cosh(i\pi z/2a)}{\cosh(i\pi b/2a)}]\cdot\frac{\cos(i\pi y/2a)}{i^3} \qquad (5)$$

where Q is volumetric flow rate, η is viscosity, $\bar{u}$ is the average flow velocity and $u(y,z)$ is the flow velocity distribution.

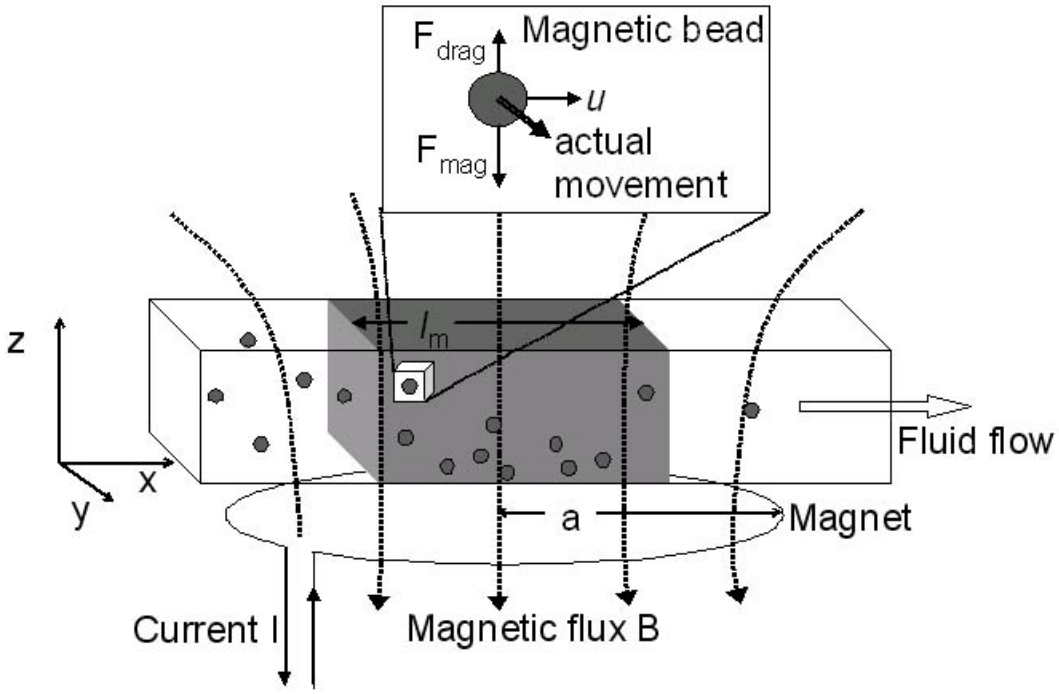

Figure 45. A model for paramagnetic beads in a magnetic and flow field. The microchannel and magnetic beads are placed on a coil and magnetic beads settle down in the center. Grey region of channel experiences uniform field in xy-plane and flux functions mainly in z-direction. In other region, the z-field intensity is much lower and, therefore, neglected.

6.1.2 Calculation of the Equations

First, the z-directional movement was calculated. The magnetic flux density for disk Neodymium magnet (diameter of1.6 mm) was 1250 Gauss at the surface (z=0) which was measured by magnetic flux meter. The equivalent current (I) for the disk magnet was 160 A, calculated from equation 2. When equation 1, 2, and 3 are inserted and rearranged, equation 4 becomes

$$k\frac{z}{(a^2+z^2)}+l\frac{dz}{dt}=m\frac{d^2z}{dt^2}$$
$$k=-\frac{3}{4}V\chi_m\mu_o(Ia^2)^2=-8.2*10^{-32}m^7N \qquad (6)$$
$$l=3\pi\eta D=2.64*10^{-8}Kg/s$$

where D is 2.8 μm, V is 1.15 * 10^{-17} m^3, m is 1.5 * 10^{-11} g and χ_m is 0.72 for M-280 Dynabeads that were used for the enzyme labeled assays.

The ordinary differential equation 6 was solved with 4th Runga-Kutta methods. Solution of the equation appears in figure 46 where z(t) for magnetic beads with different initial z-positions(zi). The beads are slightly accelerated as they approach to the magnet and the mean value for settling time is 0.0613 sec. The distance between the magnet and channel is assumed as 600 μm which is the thickness of the wafer.

Movement of the beads along x-axis can be represented by the velocity profile of fully developed laminar flow since x-directional movement of the bead is considered independent of the applied magnetic field. In a real system, x-component of magnetic field (B_x) on the edge of the magnet has meaningful value. Thus, the beads are accelerated when they enter the magnetic field and decelerated when they exit from the magnetic field. However, it could be assumed that the accelerating and decelerating

effects are compensated each other since B_x is symmetric across the center of the magnetic field and. For the sake of simplicity of the model, B_x was not included in the calculation. The velocity profile, u(y,z), is resulted from the equation 5 for the flow of 100 μL/min. aqueous solution. The dimension of the channel is 300×500 μm. Each line of figure 47 illustrates the velocity of liquid and magnetic beads in x- direction for a y-value varying z from 0 to 300 μm. The maximum velocity is 22.7 mm/sec for the bead located at the center of the channel (y = 0, z = 150 μm).

Now, we can calculate the length of the magnetic field needed for a bead to settle down at the bottom of channel. Once a bead enters into the magnetic field, z changes as a function of time while y is constant (B_y is ignored in this model since the width of channel is much smaller than the diameter of magnet). Thus, velocity in x-direction, u, is a function of time. The distance for settling is

$$d_x = \int_0^{t_s} u(y, z(t))dt$$

The integral of the above equation is calculated by finite difference method for 100 initial positions in yz-plane (Figure 48) with Δy of 25 μm and Δz of 30 μm. Figure 48 illustrates results only for the half of the channel since it is symmetric across xz-plane. The maximum distance of settling is 2.5 mm for the bead of which the initial position, (yi,zi), is (0, 300). All of the magnetic beads can be captured by the magnetic field if the length of the uniform field region is longer than 2.5 mm.

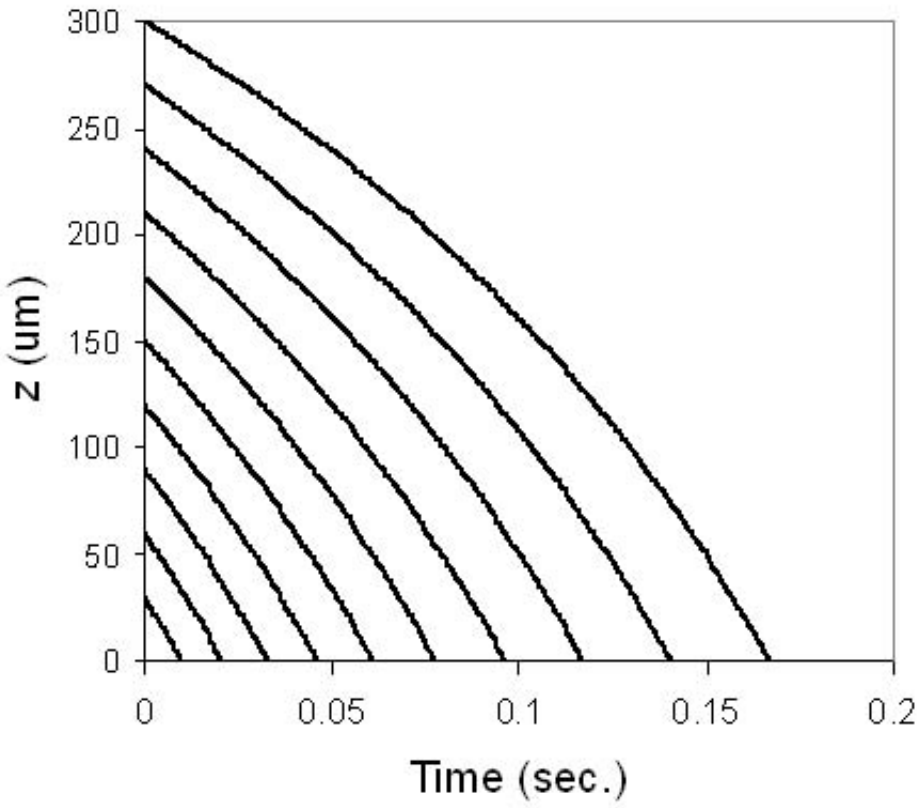

Figure 46. Vertical movement, z(t), of M-280 Dyna beads after they enter the magnetic field of a disk permanent magnet (1250 Gauss). Each line represents different position of the bead at the entrance.

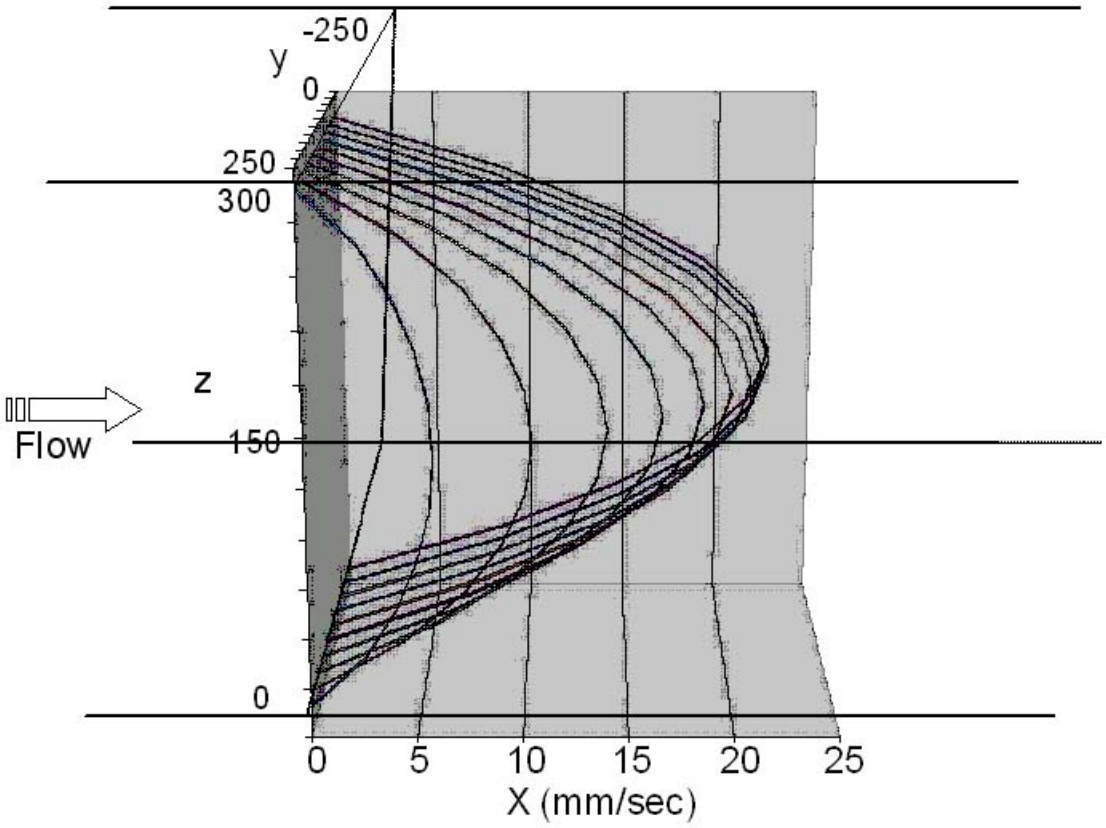

Figure 47. The velocity profile of fully developed laminar flow (100 µL/min) in the microfluidic channel (500 µm × 300 µm) x direction movement of magnetic beads is only due to this flowfield.

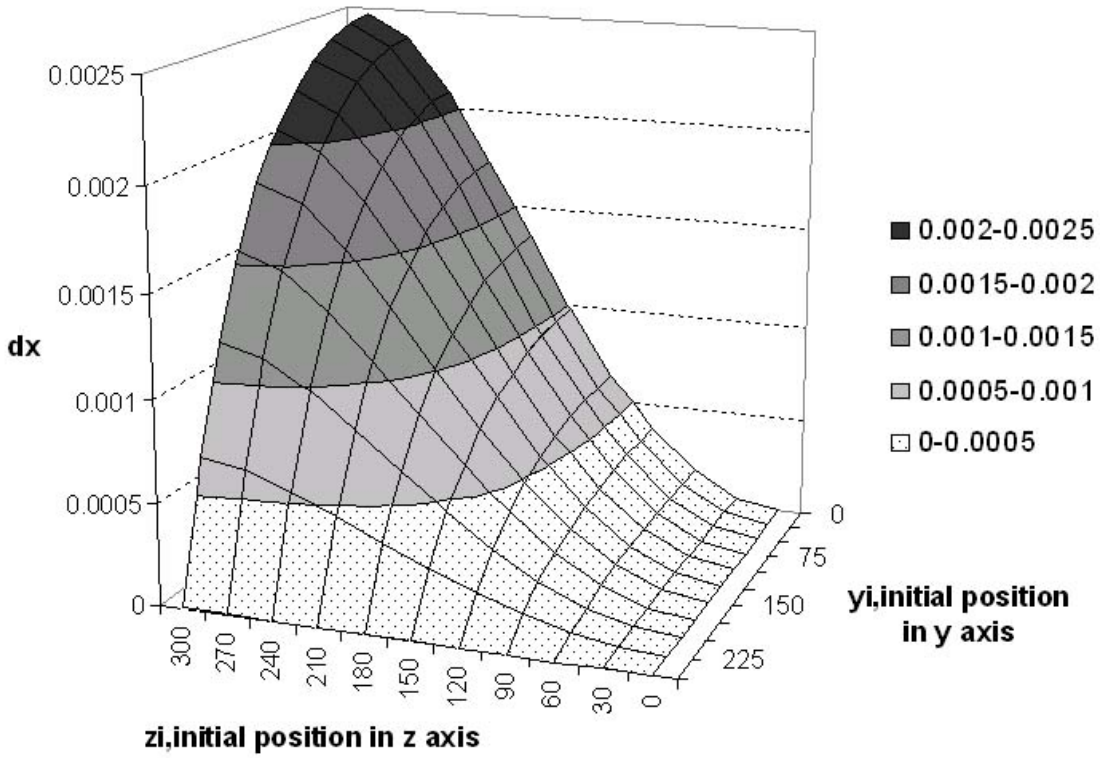

Figure 48. The distribution of magnetic beads in x direction settled on the bottom of the cannel in the uniform field model.

6.2 Distribution of Magnetic Beads in the Model

6.2.1 Interpretation of D_x (Distance of Settling)

If we assume that the beads are well distributed when they enter the magnetic field, the portion of beads entrapped on x-axis can be estimated by counting the grid point in Figure 48. Since the yz-plane has 100 grid points each grid point represents 1% of magnetic beads injected into the microchannel.

Let's assume that the length of the effective magnetic field is 0.5 mm and calculate the collecting efficiency of the magnetic collector. Magnetic beads settled in 0 ~ 0.5 mm are held by the magnetic field but the beads approaching to the bottom and not yet settled are swept with flow when they exit the magnetic field since the magnetic force pulling the beads is no longer acting on the beads. 36.5 out of 95 grid points are located in 0 ~ 0.5 mm on x-axis in figure 48. Then, 38.4 % of the injected beads are captured while 61.6 % of the beads pass the magnetic collector with a flow rate of 100 μL/min. The efficiency of the magnetic collector mentioned above is calculated as 38.4 % for Dynabeads M-280.

6.2.2 The Length of Effective Magnetic Field.

For a simple simulation model, I assumed a uniform z-directional magnetic field which is represented by the grey region of the channel in figure 45. This model not only helped to show the qualitative characteristics of a magnetic collector but also enables one to calculate the collecting efficiency. To estimate the collecting efficiency, the length of the effective magnetic field (l_m in figure 45) is a variable that has to be extracted empirically for the magnetic collector. In case of a disk magnet (diameter 1.6 mm) used in the previous experiments, the length of effective magnetic field (l_m) is assumed to 0.8 mm where the actual direction of magnetic flux is 45º from z axis.

6.2.3 Collecting Efficiency vs. Flow Rate

The portions of captured beads were calculated for different fluid flow rates from 25 ~ 200 μL/min. The magnetic beads are assumed to be well distributed before they enter the magnetic field since they are small enough. The number of captured beads is obtained by repeating the calculation with varied velocity profile for each flow rate (table 2).

Calculated collecting efficiency for 100 μL/min is 50 % which means half of the injected magnetic beads are captured and can be detected. It is slightly better than the example described at the beginning of this chapter because l_m is 0.8 mm now. The collecting efficiency becomes 100 % for 25 μL/min. Then, the magnetic force overrides the flow field slower than 25 μL/min.

Table 2. Calculated collecting efficiency of Dynabead M-280 for different flow rates (25 ~ 200 μL/min). The beads were collected with a permanent magnet (1250 gauss) in a microfluidic channel (300 μm × 500 μm).

Flow rate(μL/min)	Collecting efficiency (%)
25	100
50	76.8
100	50.5
150	38.4
200	34.2

6.3 Magnetic Beads Entrapped in a Real System.

The efficiency of magnetic collector was calculated with a simple model in the previous chapter. The result was compared with a real system's by investigating a transparent magnetic collector under a microscope.

Microfluidic channels with width of 500 μm, height of 300 μm and length of 14 mm were fabricated with polydimethlysiloxane (PDMS) and a disk magnet with diameter of 1.6 mm was mounted on the channel. The detailed design and fabrication process will be described in the next chapter. The gap between the bottom of the channel and the surface of the magnet was 0.6 mm which is the thickness of a Si wafer.

6.3.1 Methods

M-280 Dynabead suspension was diluted to a concentration of 6000 beads/mL in PBS-D and 1 mL of the solution was passed through the magnetic collector. Syringe pump pulled the diluted suspension at each speed (25 ~ 200 μL/min) and intermitted to get the images of collected beads. Each time after measurements, microchannel was initialized by liquidating with PBS-D for 30 seconds at 2 mL/min.

Figure 49 is the images taken with the microscope. (a) is the low magnification image of the permanent magnet and microchannel located on the center. The width of magnet is more than 3 times of the microchannel's so that the y-directional component of magnetic field is negligible. (b) (c) and (d) are images of microbeads settled in the channel. Since PDMS is transparent and surface of magnet is rough, the images are not very sharp but each bead is distinguishable (small black dots). Number of captured beads was counted in 1 cm × 1 cm cubic multiple times and averaged. This value was multiplied by area and makes the total number of captured beads at each flow rate.

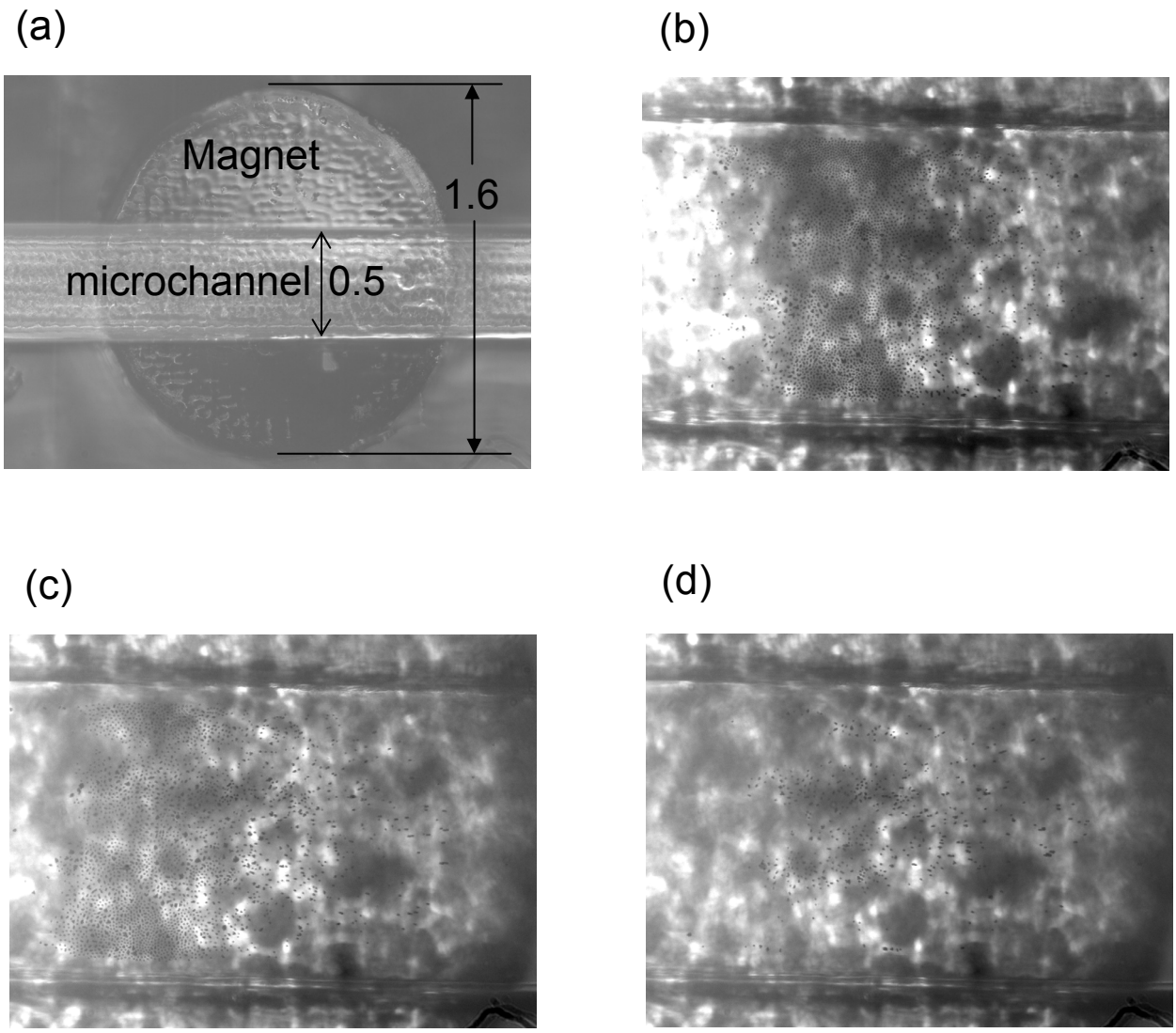

Figure 49. Microchannel on the permanent magnet (a) and captured magnetic beads (b, c, d) 1 mL of bead suspension solution (6000 beads) flowed and stopped. (b) 25 µL/min (c) 100 µL/min (d) 200 µL/min

6.3.2 Comparison of the Model and the Real Magnetic Collector

The collecting efficiency of the magnetic collector was measured for different flow rates and is illustrated in figure 50. It shows that the magnetic collector captures slightly less amount of beads than in the model which is represented with blank circles in figure 50. The results from the model and real measurement are close and show similar trends, which means the model is consistent with the real system. However, there are two major factors not mentioned before which make the real system deviating from the model one.

The first disagreement arises before the beads reach the magnetic field. I assumed that the magnetic beads are light enough for the flow field to carry them without loss. Then, low flow rate is always advantageous over a faster one in terms of collecting efficiency. In reality, particles in a fluid might sink down to the bottom and be entrapped in the corner of pathways when the flow rate is low. Reduced collection efficiency in low flow rate is accounted by the loss of beads in the channel due to sinkage. Fast flow carries magnetic beads along the fluid better and leaves fewer scattered in the microchannel. In this occasion, most of the beads arrive at the magnetic field and specified amount of the beads settle on the collector.

The second loss occurs after the collection of the beads. The settled magnetic beads experience drag force of fluid and skid on the floor of the channel. The movements of accumulated beads were observed under the microscope during collection. In a fast flow, more beads are pushed out of magnetic field region and slide into the fluid. All of the beads were cleared from the magnetic collector with a flow of 1 mL/min.

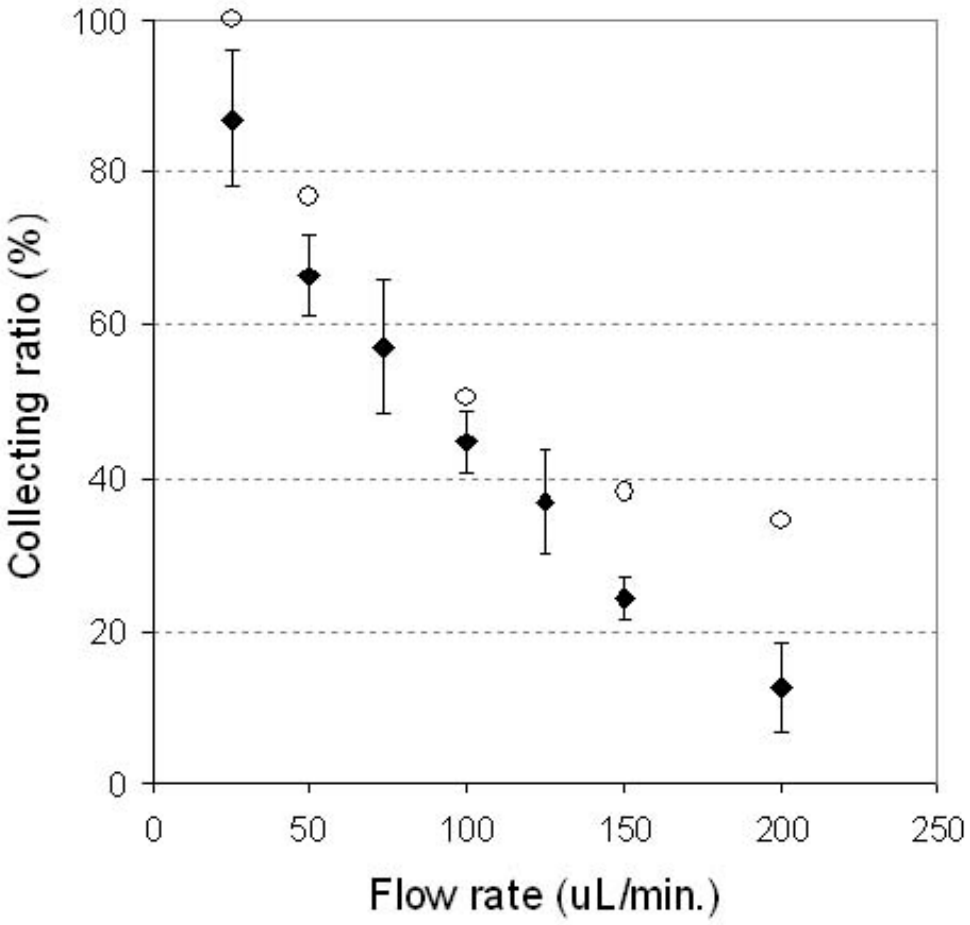

Figure 50. The collecting efficiency of magnetic beads for different flow rate. Calculated value(○) is slightly bigger than the experimental result(◆).

7. IDA ELECTRODE INTEGRATED IN A MICROCHANNEL

7.1 Design of Microchannel and Platform.

Stereolithography (SLA) was employed in fabricating molds and platforms of microchannels. The minimum feasible feature size of SLA is 50 μm on the lateral plane. Considering the size of IDA electrodes (250 × 300 μm), the microchannel was designed to have a width of 500 μm and a height of 300 μm.

The hydraulic diameter of the channel is

$$D_h = \frac{2 \times width \times height}{width + height} = 375 \mu m$$

Then, the Reynolds number of the channel for an aqueous flow of 10 μL/min ~ 1 mL/min ranged at 0.4 ~ 37.2 where the density of water is 1.0 kg/L and the dynamic viscosity is 1.12×10^{-3} N·s/m^2. Since the Reynolds number is below 3000 for this range of flow rate, the channel mostly experiences a laminar flow. To avoid unpredictable results, a laminar flow is preferred to a turbulent flow. As the IDA electrode and magnet are supposed to be in laminar flow region in the model described at chapter 6. The length of entrance region was also calculated 0.84 mm for an aqueous flow of 1 mL/min, which means the IDA electrode and magnet need to be at least 0.84 mm distance apart from any change of the channel such as bend or junction. Fully developed laminar flow was assumed by locating the IDA electrode 5 mm apart from the bend of microchannel (see Figure 51).

Figure 51 illustrates the assembly of microchannel, IDA chip, and magnet using a platform. The microchannel was attached to an IDA chip and then assembled with

magnet to overlap IDA electrode and magnet. The alignment of the magnet and IDA electrode is critical so that tight fitting recesses on the alignment platform guides their position. The flow direction is from left to right and the entrance and exit of microchannel were widened to fit flexible Tygon tubing with I.D. of 0.8 mm and length of 84 mm. The dead volume from the injection tubing and microchannel was calculated to be 44 μL. Top of platform has an opening where the microchannel can be visually inspected *in situ*.

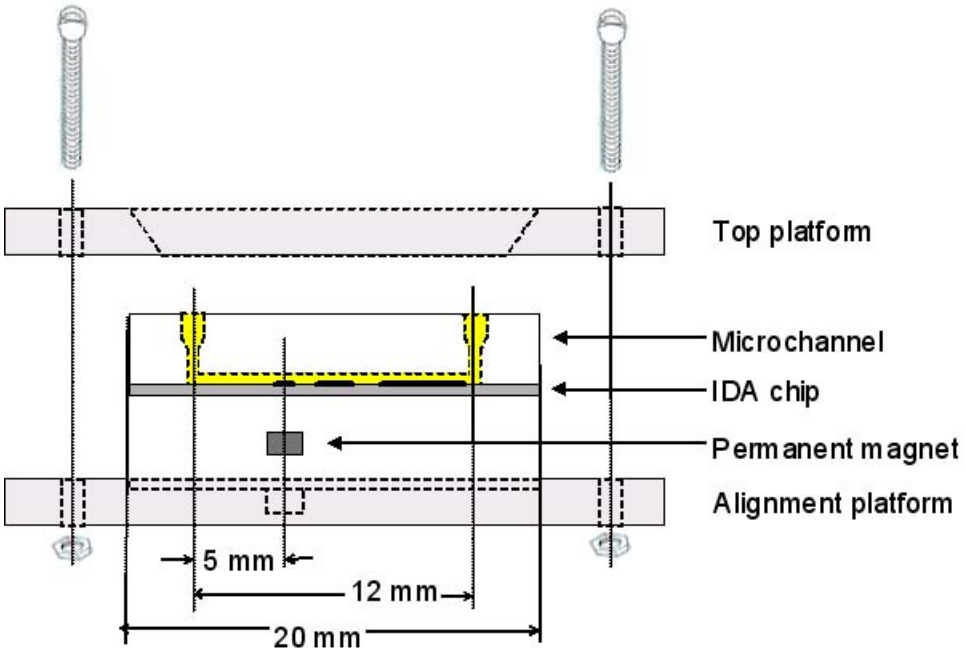

Figure 51. The microchannel and plaform for the assembly with an IDA chip and a magnet.

7.2 Fabrication of Microchannel Assembly

7.2.1 Stereolithography

3-D design of the platform and mold of microchannel was constructed using Pro/Engineer with exact dimensions. The molds for microchannels are specially designed with 3 parts for easier separation of microchannel structure from the mold. With the model opened in Pro/Engineer, it was saved in a STL format for the Stereolithography (SLA) machine to be able to fabricate it. The STL file is inserted into a program called 3D Lightyear which controls the SLA machine. 3D Lightyear allows the user to orient and layout the part on a 3D platform that represents the actual platform of the SLA machine. The support for the designed structure is automatically created by the program.

SLA-Viper from 3D Systems (Valencia, CA) was used to fabricate the mold and platform for microchannel in a high resolution mode. A Nd:YV04 laser defined the structure in a bath of photopolymer resin, Cibatool SL 5510. The tensile strength of the resin is 77 MPa, which is sufficient to provide durability for the molds of microchannel.

Once the parts are completed, the resin was drained and rinsed with Tripropylene Glycol Monomethyl Ether (TPM). Parts with TPM are placed in an ultrasonic bath for 30 minutes to aide the cleaning process. Afterwads, the parts are rinsed with isopropyl alcohol and resin left in narrow holes is removed with a strong air blow. After the cleaning, the parts are cured in a UV oven for 90 minutes.

7.2.2 PDMS Process

We used PDMS (polydimethylsiloxane) to fill the mold and create the device exploiting its ease of fabrication and chemical inertness. PDMS, dubbed 'silicone', is widely used for medical implants due to the high degree of chemical and thermal stability and resistance to oxidation. PDMS is an inorganic polymer with a backbone of a chain of alternating silicon and oxygen atoms. It makes good elastomers because the bonds between a silicon atom and the two oxygen atoms attached to it are very flexible. The angle formed by these bonds can open and close like a scissors without much trouble. The flexibility enabled multiple replications of SLA molds and leak-free binding of PDMS structure to the IDA chip. Additionally, its transparency makes

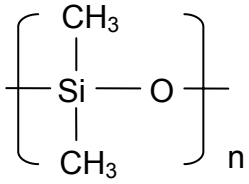

inspection of microbeads feasible.

Sylgard 184 Silicone Elastomer from Dow Corning has minimal shrinkage and no solvent or cure byproducts. The polymer was prepared by adding the curing agent to the base with 10 parts base to 1 parts agent. After mixing them carefully, the mixture was de-aired in a vacuum chamber for 30 minutes. Then, the SLA parts were assembled and the PDMS was poured into the mold. To remove possibly included air while pouring, PDMS in SLA molds were de-aired for another 30 minutes. Finally the PDMS was thermally cured. Since the heat deflection temperature for the Cibatool SL 5510 resin is 62 °C, PDMS was placed into a 60 °C oven for 10 hours. Completed PDMS microchannels were easily demounted by disassembling the SLA molds.

7.2.3 Material Stability of SLA and PDMS

Materials of microchannel are required to be chemically inert to avoid possible contamination. SLA resin, Cibatool SL 5510, was once assessed as a material of microchamber of ECIA since the resin was known to be designed for a high humidity environment. After 5 hours of soaking in 0.1 M phosphate buffer (pH 7), some electrochemically active materials leeched out from a fully cured SLA structure. It was confirmed by bold peaks appeared at 300 mV and 60 mV vs SCE in a cyclic voltammogram of the soak solution. Thus, SLA structure itself was excluded as a microchannel in the present experimental condition.

Likewise, PDMS microchannel was soaked in the buffer solution overnight and the solution was analyzed with cyclic voltammetry. Since the potential range deployed for the immunoassay with PAP is -0.3 ~ 0.3 V vs Ag/AgCl, potential swept in a range of -0.6 ~ 1.0 V leaving no conceivable peaks. It means that the PDMS structure was properly cured and the microchannel offered an interferant-free condition for the ECIA.

7.2.4 Microbead Holdover on the Microchannel

The adhesive surface of PDMS enabled leak-free contact made with the silicon nitride coated silicon wafer using finger pressure. However, it is probable for microbeads to adhere to the surface causing carryover between measurements. It was investigated whether the surface of PDMS microchannel is appropriate for microbead-based immunoassays by comparing with Parylene(poly para-xylylene) coated microchannel.

Parylene reduces elastomer tack and surface stickiness without adding stiffness to the part. Parylene's static and dynamic coefficients of friction, which are in the range of 0.25 to 0.33, allow coated elastomers to approach the dry film lubricity of PTFE[50]. The coefficient of friction for Parylene C, as measured by ASTM D 1984, is 0.29 for both static and dynamic observations. Chemical inertness of Parylene improves the surface characteristics as two of the Parylenes, N and C, are certified to comply with USP biological testing requirements for Classification VI, including Acute Systemic Toxicity, Intracutaneous Toxicity, and Implantation. Parylene provides a pinhole-free coating due to its chemical structure such as high molecular weight, a crystalline form, and an all-carbon backbone. The chemical structure of Parylene C is

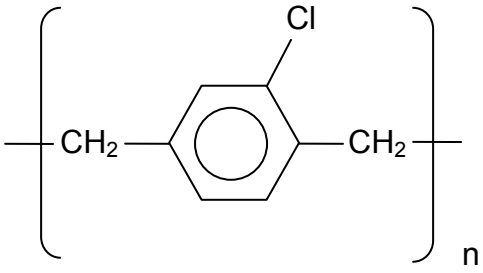

One of the most important distinguishing features of parylene is vacuum deposition leading to the absence of surface tension, meniscus, bridging or pooling. This

unique property is due to the fact that Parylene is deposited as a gas at the molecular level rather than as a liquid. Vacuum deposition results in a very high degree of coating conformality over inside and outside corners, and in deep crevices. Thus, the structure of PDMS channel is exactly maintained after parylene coating. The deposition was carried out at room temperature. of parylene was deposited up to 0.5 μm on the recessed region of PDMS structure while appears a second PDMS film was overlaid the PDMS flow channel to act as a mask to prevent Parylene coating of the edges of the PDMS flow channel.

After 6000 Streptavidin coated M-280 Dynabeads were injected and captured on the magnetic collector, clean buffer solution flew through the microchannel at 2 mL/min to wash out the captured beads. When the beads were settled on PDMS channel, 10 ~ 20 beads were left on PDMS surface after 1 minute of the rinse. In case of parylene coated channel, parylene reduced the stickiness of surface so that the microbeads were clearly rinsed off from the channel. In the immunoassays, the surface-modified beads settled on the IDA chip not on the PDMS surface and microbeads were completely removed after the rinse in both of the PDMS channels with and without parylene coating. β-galactosidase-saturated beads were also cleared of the PDMS microchannel with 1 minute rinse of buffer solution at 2 mL/min. Thus, parylene coating helped to avoid microbeads' clinging to the surface of channel but it was not required for our present purpose. PDMS microchannels were used without parylene coating in the subsequent immunoassays.

7.2.5 Stabilization of Redox Cycling in a Microchannel

After solutions flow through the channel to deliver the enzyme-bound microbeads and substrates, the stream should be intermitted to measure the redox cycling current. IDA electrodes build a diffusion layer of redox cycling immediately after potentials were properly applied and any disturbance of stationary solution will damage the steady-state and perturb the response. Ideally the solution becomes still when the pump was switched off and achieves the steady state of redox cycling. However, it takes time to achieve a stabilized diffusion layer due to the inertia of the flow.

Figure 52 illustrates the progresses of redox cycling current after the pump was stopped. At 1 minute the liquid flow introduced 5 mM $Fe(CN)_6^{3-}$ solution to the IDA electrode and the current upsurges. In spite of multiple grooves in IDA electrodes, blank buffer solution was replaced with ferricyanide solution and uniform current level was accomplished in a few seconds even with slowest flow rate of 0.1 mL/min. It means a few second's flow is enough when we introduce substrate solutions to the collected microbeads. The steady state currents for slower flows are higher than for faster flows since the product of redox cycling is not completely washed out and partially contribute to the response. The pump was stopped at 2 minute and the current increases gradually to reach a steady state of redox cyling, 225 nA. For faster flow rates, the solution approached to the steady state current faster. It took about 30 seconds for flow rates over 1 mL/min but it took over 2 minutes at the flow of 0.1 mL/min.

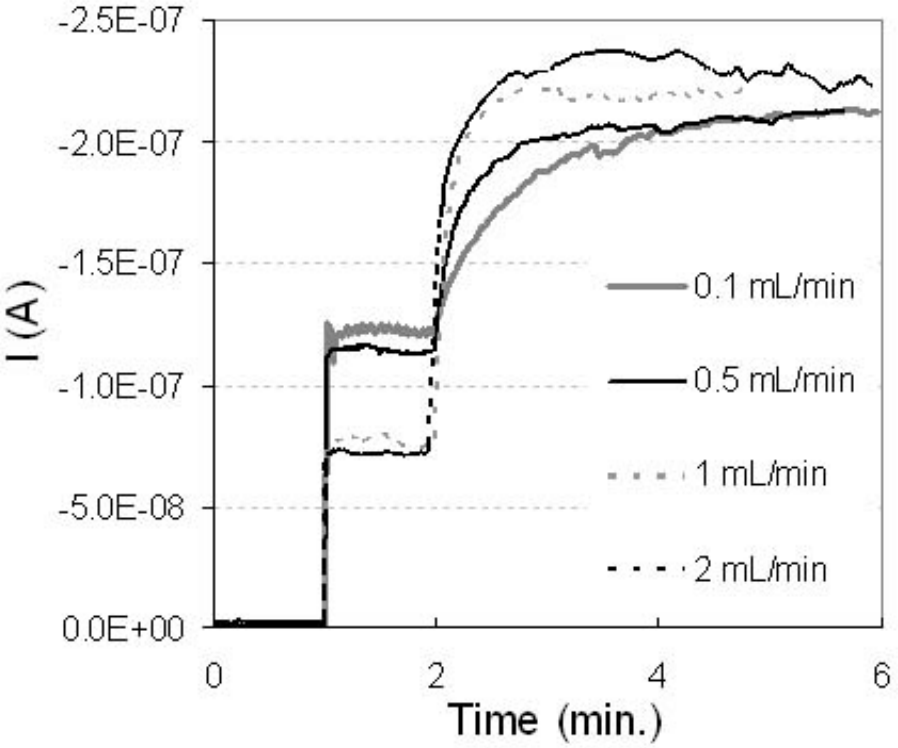

Figure 52. Stabilization time of redox cycling current in a fluidic channel..

7.3 Viral Detection in a Microchannel

Viral agents are one of four classes of bioterrorism agents; toxins, viruses, bacterial cells, and spores. Researchers used simulant agents to test biological warfare detection equipment. A simulant is a relatively safe chemical or biomolecule used to mimic the properties of a hazardous material. Ovalbumin is a stimulant for protein toxin, Erwinia herbicola (EH) is a simulant for vegetative bacterial cells, Bacillus globigii (BG) is a simulant for anthrax spores and bacteriophage MS2 has been used as a stimulant for viral bioterrorism agents. MS2 is a well-characterized virus with a known nucleic acid sequence[51] and crystal structure[52]. MS2 RNA consists of 3569 nucleotides containing the genetic information for the A protein, coat protein, and the replicase protein. The 180 copies of the coat protein and 1 copy of the A protein encase the RNA forming a small viral particle with a 26 nm diameter[53].

IDA sensor in a fluidic channel was applied to MS2 assay using a MS2 specific antibody. Figure 53 shows MS2 bound to the surface of a microbead using anti-MS2 IgG and labeled with a β-galactosidase. The size of MS2 is comparable to β-galactosidase.

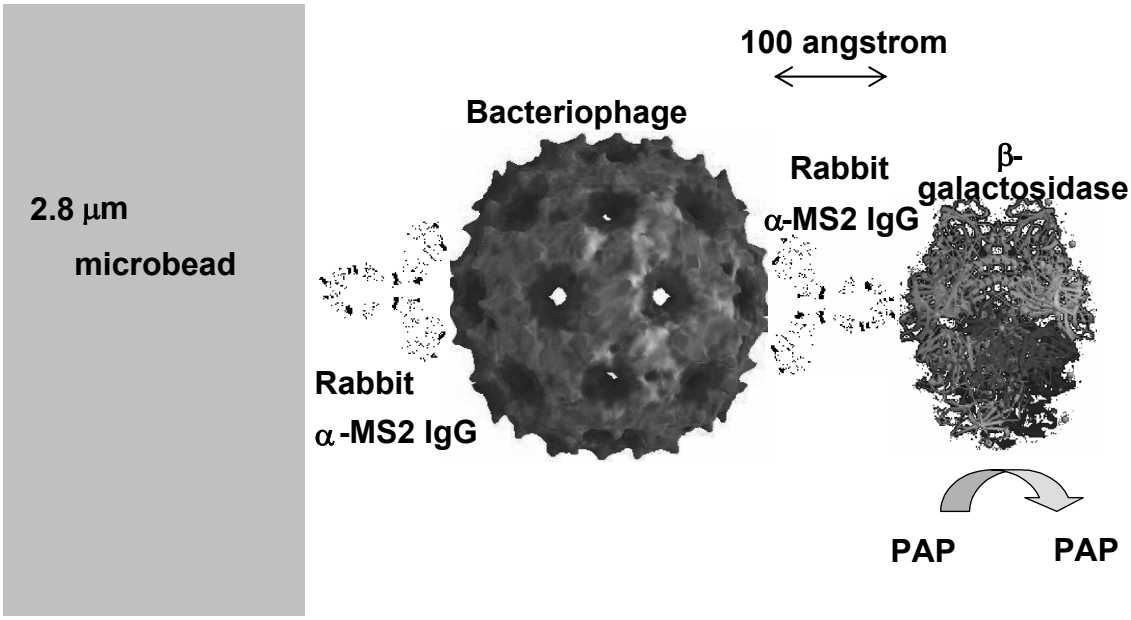

Figure 53. Schematic of the bead-based immunoassay for bacteriophage MS2

7.3.1 Methods

Materials used in the previous immunoassay are described in chapter 5. For the assay of MS2, new materials were added.

Rabbit anti-MS2 IgG was a generous gift from Tetracore, Inc (Gaithersburg, MD). β-Galactosidase and the conjugation of β-galactosidase to rabbit anti-MS2 IgG were from American Qualex Antibodies (San Clemente, CA). Bacteriophage MS2 (1 mg/mL) was generously given by Michael Goode (Aberdeen Proving Ground, MD) and Sulfo-NHS-LC-biotin was from Pierce (Rockford, IL). PBS-B, the biotinylation buffer, was 0.044 M KH_2PO_4, 0.056 K_2HPO_4, and 0.15 M NaCl in OrganicPure H_2O, pH 7.2.

It was necessary to biotinylate the rabbit anti-MS2 IgG (1º Ab) in order to attach it to the streptavidin-coated bead. In a glass vial, 24 μL of 0.018 M sulfo-NHS-LC-biotin in OrganicPure H_2O were added to 900 μL of 3.2 mg/mL rabbit anti-MS2 IgG in PBS-B. The solution was incubated with gentle shaking for 30 min at room temperature. Then, biotin attached rabbit anti-MS2 IgG was separated from the mixture with a desalting column. The biotinylated product was determined to have a molar ratio of 0.9 mol biotin / mol protein, which is sufficient for antibody attachment and fewer biotin per antibody minimizes the chance of biotin being located in the antibody-binding site.

Preparation of enzyme labeled microbeads was identical to the previous one except that biotin-rabbit anti-MS2 IgG (1º Ab), MS2, rabbit anti-MS2 IgG*β-galactosidase (conjugate) was used instead of biotinylated anti-mouse IgG, mouse IgG, anti-mouse IgG-galactosidase. The appropriate MS2 concentration was alloted to glass tubes to give 60 μL of 0, 0.05, 0.1, 0.25, 0.5, 1, and 2 μg/mL MS2.

Figure 54 depicted the experimental setup of microfluidic system for bead-based electrochemical immunoassay with IDA electrodes. Potentials of +290 mV and –300 mV were applied to the two working electrodes of the IDA with a thin film Ag/AgCl reference electode. The current was measured throughout the following procedure. 100 μL of bead solution at 50 μL/min was injected after the channel was rinsed with PBS-D at 500 μL/min for 30 s. Then, PBS-D was injected into the channel for 100 s at 50 μL/min, which is determined by considering the assay time and collection efficiency. Model M362 ThermoOrion Sage (Beverly, MA) syringe pump was used to control the flow during the experiment. At 250 s, 100 μL of 4 mM PAPG were injected at 50 μL/min and the flow was stopped at 360 s. It took about 1 minute for the solution to reach IDA electrode from its vessel. Thus, substrate solution passed the sensing area for 50 seconds which is enough for new solution replace the existing PBS-D. The flow resumed at 480 s, sending PBS-D through the channel at 1 mL/min, and beads were removed from the fluidic device. The IDA was electrochemically cleaned between each sample by cycling the potential between +1500 mV and -1200 mV at 50 mV/s in the presence of PBS-D as in previous assays.

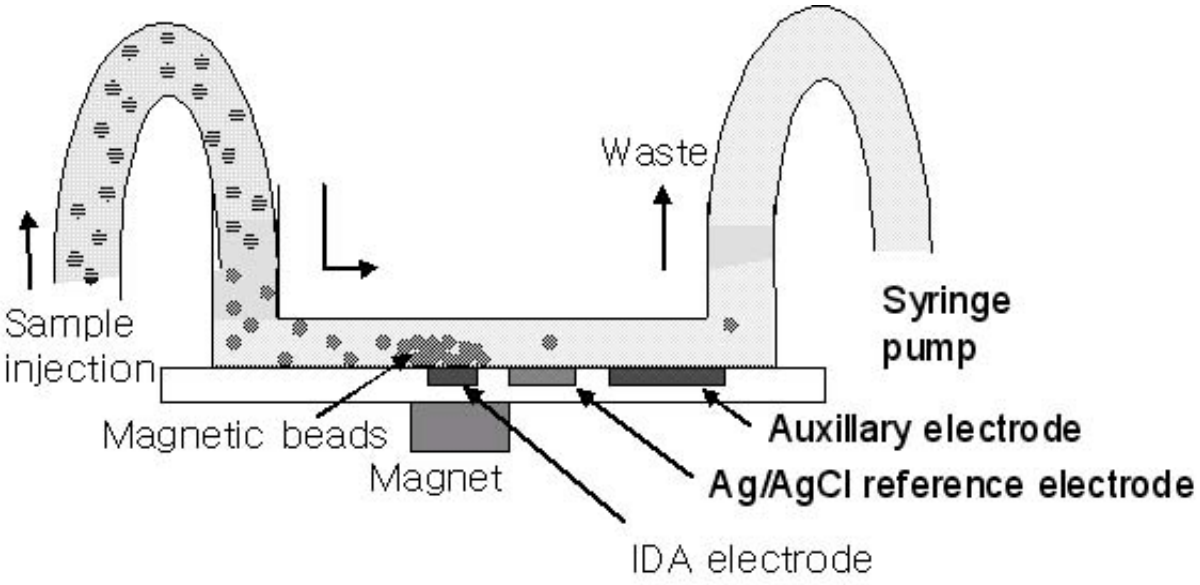

Figure 54. Experimental setup for IDA sensor in a fluidic channel

7.3.2 Minimum Detectable Number of Beads

Performance of the fluidic system for ECIA was compared with the previous setup by measuring the minimum detectable number of beads. Surface of magnetic beads was saturated with β-galactosidase as described in chapter 5. At 290 sec., the current increased proportionally to the number of beads when the substrate solution arrived at the collected beads. However, we were interested in the increase of current after the stream was intermitted since the response was more distinct at 360 sec. The slope of curves was slightly reduced with time due to the reduced concentration of substrate around the beads. However, the flow of the solution through the channel spread the beads over the diameter of the magnet reducing the bead clump seen in a stagnant microdrop of solution. This appeared to minimize enzyme substrate depletion within the vicinity of the bead clump seen in the previous study. Therefore, curves are closer to linear increase than in case of assays in microdrops (Figure 55).

A linear range was established for log [number of beads], between $1.3x10^3$ and $6.5x10^5$ beads, and log [change in generator current with time] between 370 and 380 s with $R^2 = 0.995$. The limit of detection was determined by 3 times the standard deviation of the blank signal, which was 130 beads which is twice of the experiment in microdrops. In the magnetic collector, collecting efficiency was 66% with flow rate of 50 μL/min. The loss of magnetic beads resulted in a reduced sensitivity.

Each sample was measured twice without exclusion of data. Unlike the experiments in microdrops, we do not have to rule out the data when the beads were located off from the IDA sensing area. 1300 enzyme-saturated beads were measured three times to assess the repeatability and the relative standard deviation was 9 %. .

Magnetic collector, injecting the beads into the channel with a syringe pump instead of manually pipetting beads into a drop, was more reproducible as the bead injection did not rely on the experimenter's ability to position the pipet at the same point on the drop.

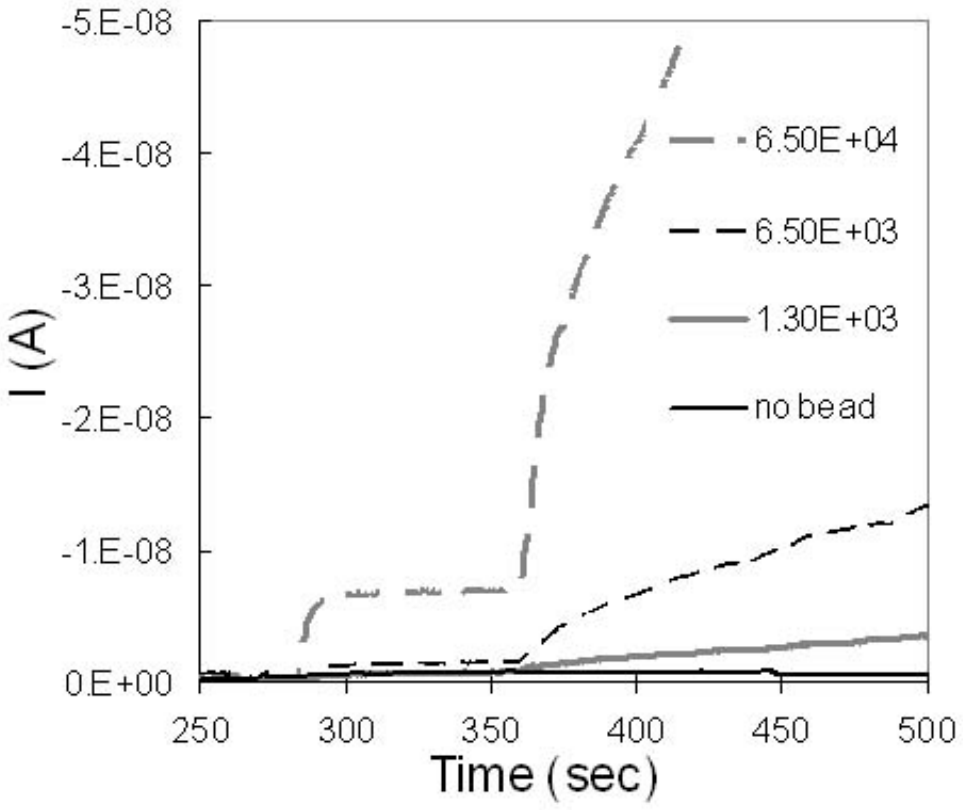

Figure 55. Response of IDA electrode integrated in a microchannel to enzyme saturate microbeads

7.3.3 MS2 Assay with RDE

RDE experiments were carried out to appreciate the IDA sensor in a fluidic channel by comparison with the effect of microfluidic channel on the IDA sensor performance.

The experimental setup is the same as in chapter 5. The detection of bead-based procedures used a 30 μL drop of 5.3 mM PAPG in PBS-D initially and the potential was applied to the electrode spinning at 3000 rpm. After a 15 s quiet time, the current was measured to establish a background slope. At 30 s, 10 μL of bead suspension were added to the drop. The run terminated after 70 s. The slope between 50 and 70 s was corrected by subtracting the background slope, taken between 15 and 25 s. MS2 assay was done in a concentration range between 0 and 25 μg/mL and the results are seen in Figure 56. The assay was limited by the detection method rather than non-specific absorption (NSA), as a significant signal was not detected for the 0 μg/mL MS2 standard. . A plot of this region as log reaction velocity (nA/s) vs. log MS2 concentration (μg/mL) was described by $y = (1.00 \pm 0.12)\, x + (0.81 \pm 0.01)$. The detection limit, determined by three times the standard deviation of the blank signal, was 200 ng/mL MS2, or 3.2×10^{10} viral particles/mL.

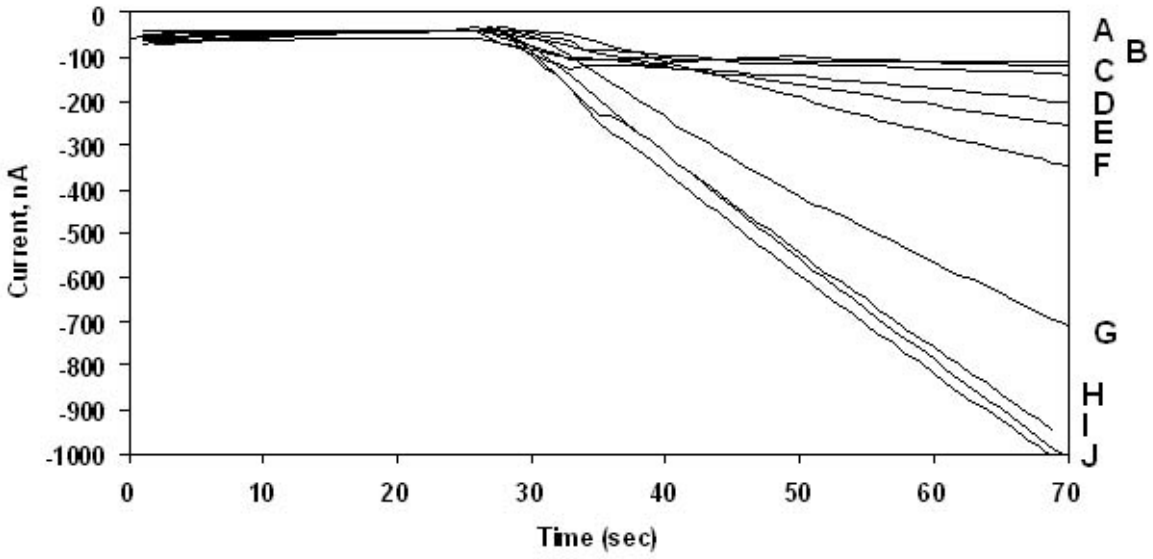

Figure 56. MS2 assay with RDE. MS2 concentrations were A) 0 mg/mL, B) 0.1 mg/mL, C) 0.25 mg/mL, D) 0.5 mg/mL, E) 0.75 mg/mL, F) 1 mg/mL, G) 2.5 mg/mL, H) 5 mg/mL, I) 10 mg/mL, and J) 25 mg/mL.

7.3.4 MS2 Assay with IDA in a Fluidic Channel

An amperogram for the 100 ng/mL MS2 sample is shown in Figure 57 to illustrate the procedure in terms of current vs. time. Initially, potentials were applied to the two working electrodes, +290 mV and -300 mV vs. Ag/AgCl, while PBS-D was flowing through the fluidic device. At 30 s, 100 μL of the bead sample, 1 x 10^6 beads / 100 μL, were injected into the device followed by 80 μL of PBS-D to recover any beads not retained by the flow. At 250 s, 100 μL of the enzyme substrate, PAPG, were injected, and an increase in anodic current was seen when the enzyme substrate reached the beads held over the electrode. In Figure 57, this increase in anodic current was seen at approximately 290 s. The flow was stopped at 360 s, a steady-state was reached, and increasing anodic current was observed which is directly related to the increasing PAP concentration, as the enzyme converted PAPG to PAP. At 480 s, beads were rinsed out of the channel with PBS-D at 1 mL/min. Within 8 min, beads were collected on top of the electrode, enzyme substrate was introduced, and enzymatic conversion of PAP was monitored which related to the concentration of MS2 present in the sample. With a smaller dead volume, the whole process could be done in 5 min.

Figure 58 shows the current vs. time plots for MS2 concentrations between 0 μg/mL and 2 μg/mL for the time period that the enzyme substrate was present in the fluidic device. The lower MS2 concentrations extended down to 50 ng/mL MS2 in hopes of lower detection limits with the IDA electrode than with the RDE method. The log of the slope of current vs. time between 400-450 s was plotted against log MS2 concentration (Figure 59). A linear range was observed from 0.1 μg/mL to 2 μg/mL MS2, and the plot was described by $y = (1.18 \pm 0.09)\, x + (0.06 \pm 0.25)$. The limit of

detection was 0.09 μg/mL MS2, or 1.5 x 10^{10} MS2 particles/mL, as determined by three times the standard deviation of the signal for the 0 μg/mL MS2 sample.

Detection limits with the IDA electrode in the fluidic channel were lower than those obtained with the RDE method. Although the rotation of the RDE provided enhanced mass transport, the electrochemical recycling of the PAP/PQI couple by the IDA electrode gave a detection limit approximately half of the RDE method. Furthermore, a signal from NSA of biomolecules was detectable with the IDA electrode, in contrast to the RDE method, so the IDA electrode detection was limited by NSA of the biomolecules rather than by instrumental capabilities. Suppressing the interference of NSA should lead to even lower detection limits with the IDA method.

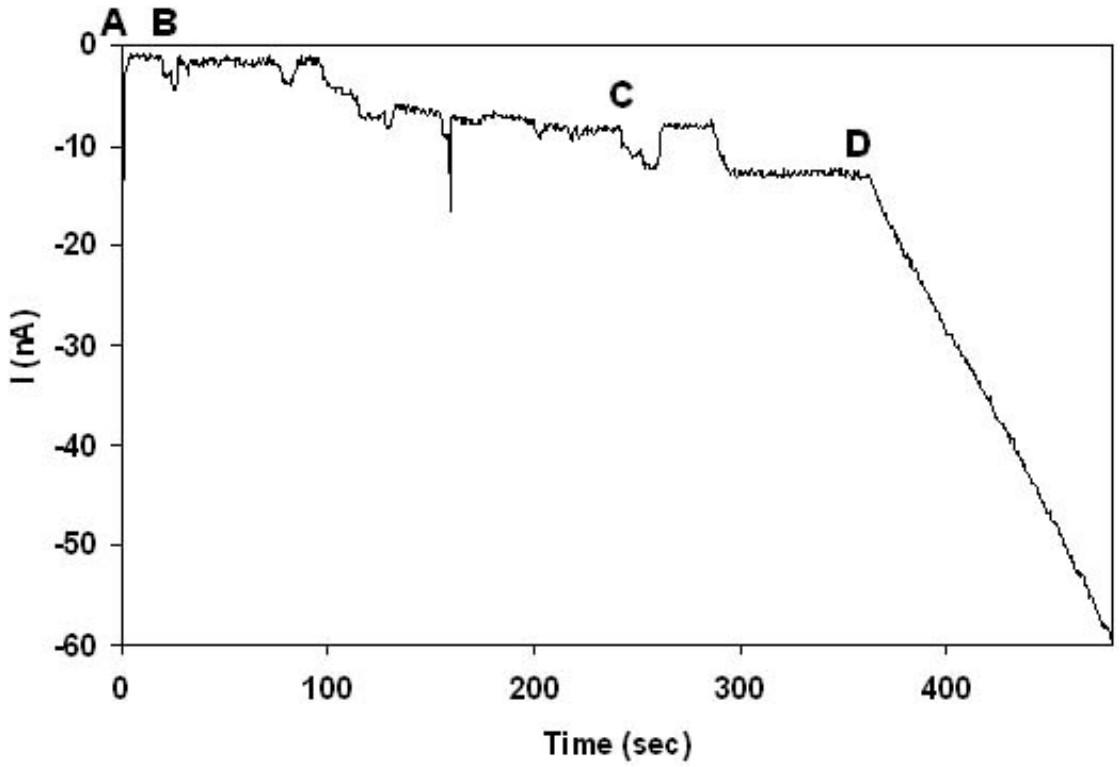

Figure 57. Amperogram for the 100 ng/mL MS2 sample detected in the PDMS channel at an IDA electrode

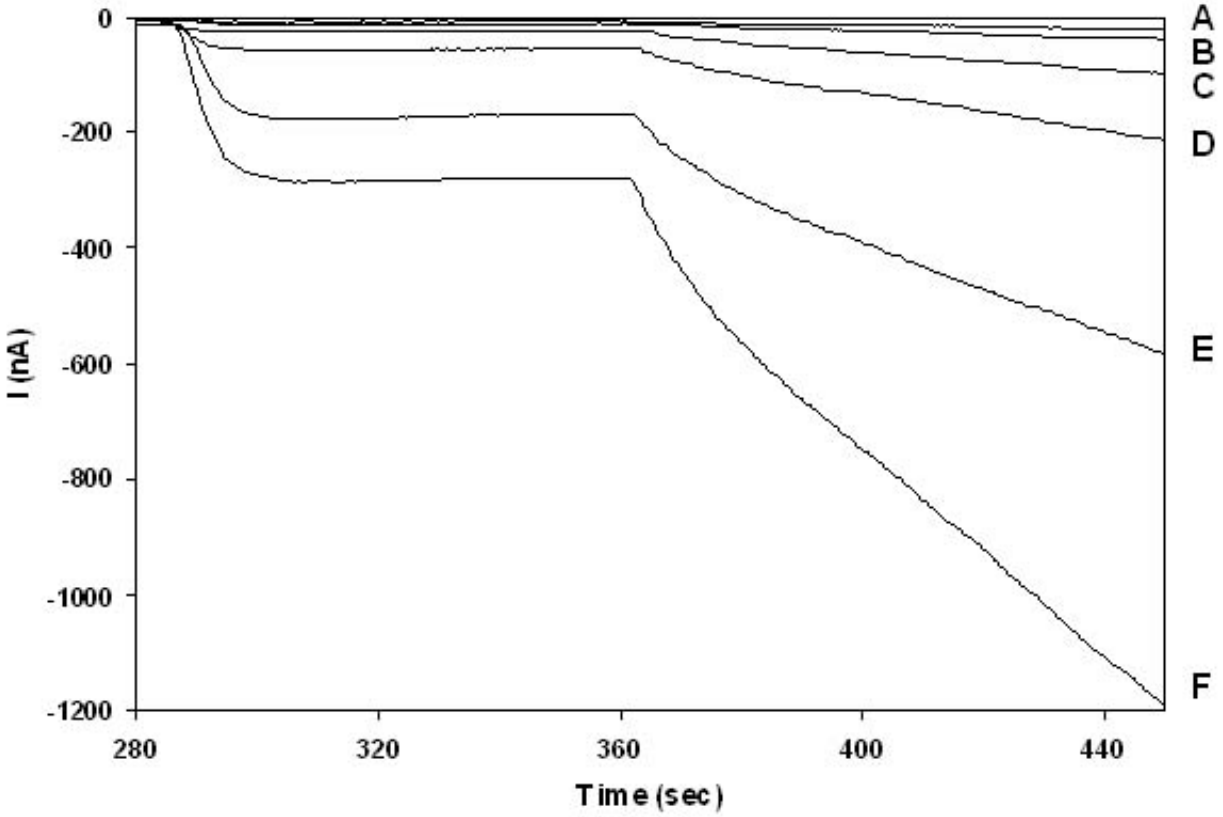

Figure 58. Current vs. time plots for the following MS2 concentrations detected in the PDMS channel at an IDA electrode. A) 0 mg/mL, B) 0.1 mg/mL, C) 0.25 mg/mL, D) 0.5 mg/mL, E) 1 mg/mL, and F) 2 mg/mL

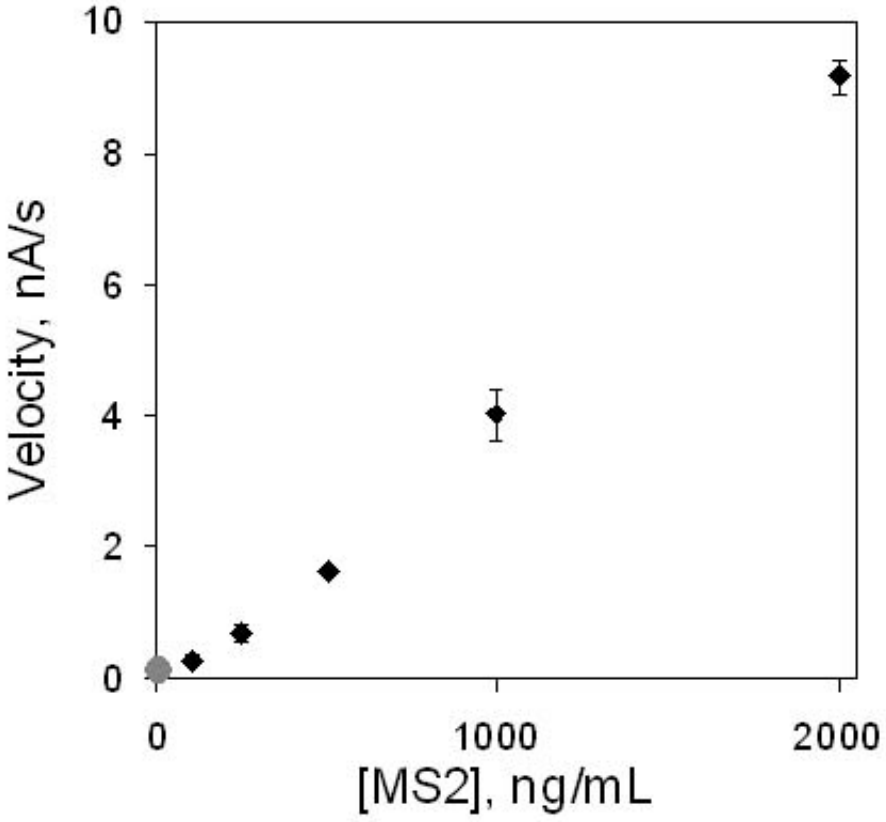

Figure 59. Calibration curve for MS2 with IDA sensor in a fluidic channel. ● represents the signal from non-specific adsorption.

7.3.5 Number of Beads vs. Signal from NSA

For both RDE and IDA experiments, 1 x 10^6 beads were used in each sample. Since NSA was the limiting factor in IDA measurements, the resolution of IDA fluidic sensor can be improved with reduced NSA Thus, the relation between NSA and the number of beads was investigated. Table 3 compares the response with 1 x 10^6 beads and 2 x 10^5 beads in an identical experimental condition. 0, 0.1 ng/mL and 0.25 ng/mL of MS2 solutions were used. The response from NSA was decreased into 1/5 when the number of microbeads was reduced to 1/5. On the other hand, the signal from MS2 samples were decreased only into ½ for 0.1 ng/mL and 0.25 ng/mL of MS2. We could predict that the limit of detection can be lowered into 2/5 by reducing the number of magnetic beads. Even smaller number of bead might lower the detection limit. Due to the limited supply of MS2, the expectation could not be verified completely. However, it could be concluded that smaller number of magnetic beads is advantageous in analysis of diluted samples.

It has been reported that exposure to only 10 particles of smallpox can be toxic if not lethal. Our method is far from detecting concentrations at that level, but falls nearer to the range of toxicity for some viral hemorrhagic fevers[54], between 10^5 and 10^{10} particles with reduced NSA. Although improvements in detection limit are needed for an early warning system, the reported method can selectively detect a virus of interest, assuming the appropriate antibody is available.

Table 3. Current response with varied number of beads in a IDA-integrated fluidic channel.

Unit: pA/sec

	1×10^6 beads	2×10^5 beads
Non-specific adsorption	-6.20	-1.49
0.1 ng/mL	-85.0	-46.8
0.25 ng/mL	-260	-132

8. CONCLUSION

IDA electrodes with different geometric structures were fabricated with the smallest gap being 2.4 μm. A novel comb IDA was made by combining the anisotropic profile of Si deep RIE with the directional evaporation of metals. Both simulation and experiment showed that redox cycling efficiency could be improved with comb IDA electrodes. The comb IDA enhanced the current 3 times more than a conventional coplanar IDA as predicted from FEM modeling.

An electrochemical enzyme assay was carried out with coplanar and comb IDA electrodes. Since the enzyme was attached to the magnetic beads we could move it in a controlled way. These types of assays are versatile since one can easily coat the magnetic beads with a functional group that determines which analytes will be captured. A microbead-based sandwich immunoassay with continuous detection has been demonstrated at a coplanar IDA electrode. Using β-galactosidase as an enzyme label, incubation of the enzyme with the substrate and detection of the enzyme product could occur simultaneously without fouling the surface of electrodes. Each measurement is complete within 10 min, whereas measurements that isolate the incubation of the immunocomplex with the enzyme substrate from electrochemical detection required more than 20 min. The detection limits with continuous measurements are comparable to those obtained with discrete measurements[55]. The detection limit for the immunoassay was 26 ng/mL (3.5×10^{-15} mol) mouse IgG, which is lower than the 50 ng/mL (6.7×10^{-15} mol) mouse IgG detection limit obtained with RDE amperometric detection. The immunoassay was limited by non-specific adsorption of the biomolecules to the bead

surface. Minimizing non-specific adsorption will lower the background current, improving the signal-to-noise ratio.

It was demonstrated that enzyme activity from a bead-based immunoassay can be monitored continuously with an IDA electrode; however, the experimental setup is not ideal. Since the electrodes were separated from the enzyme-labeled beads by a couple of millimeters, the response starts more than 3 minutes after injection. With a comb IDA electrode, magnetic beads were placed directly on the comb structure but they were not in contact with the electrode surface during the measurements. Thus, the current responded immediately and the analysis time was reduced to 1 min with improved sensitivity. The minimum detectable number of beads was 60, equivalent to 70 amole of β-galactosidase, which is 1/20 the amount compared to experiments with coplanar IDA electrodes. The vertical comb electrodes reported by Honda *et al.* [56] have also been applied to redox cycling immunoassay utilizing ALP and paramagnetic beads and demonstrate enhanced entrapment of the PAP/PAPP redox molecules. However, one of the benefits of the comb electrode we report is that the beads are larger than the electrode spacing so that they do not come into direct contact with the surface to avoid potential fouling of the electrode.

The repeatability of each measurement was an issue in the experiments. Manual pippetting was not the best method to introduce magnetic beads into the substrate solution since both the sensor and the solution have a very small size. Incorporating the IDA electrode into an automated fluidic system could improve the procedure by removing the variability associated with manual pipetting and with positioning the beads relative to electrode. An encapsulated detection chamber with the IDA electrode's

position fixed could decrease the detection volume and spread the beads around the electrode.

Behavior of magnetic beads passing a magnetic field in a fluidic flow was simulated to design a magnetic collector. Measured collecting efficiency was slightly lower than that calculated due to the loss of sunken beads before the magnetic field and the skidding beads from the IDA sensor after settlement. Magnetic collector was composed of IDA chips and PDMS microchannels assembled in a platform. The platform and mold of PDMS channel was fabricated with SLA. The minimum detectable number of beads for an IDA sensor with the magnetic collector was 130, which is about double of that for the microdrop experiment. The reduced sensitivity can be explained by the collecting efficiency of magnetic collector, 65 %. However, microbeads were well-dispersed on the IDA electrode in a regular manner, which improved the reproducibility of measurements. The current increased almost linearly since depletion of substrate in the vicinity of the beads was alleviated.

A paramagnetic bead-based electrochemical immunoassay has been developed to detect bacteriophage MS2, a biothreat agent simulant. IDA sensor in the magnetic collector was 2 times more sensitive than RDE in a microdrop. Further improvement was possible by reducing the number of beads for the IDA assay since the detection was limited by non-specific adsorption. The detection methods compare well with other MS2 immunoassays that have been recently reported. Rowe *et al.* have demonstrated an array biosensor that uses a sandwich immunoassay format and fluorescent labels to detect MS2 at 400 ng/mL [57]. McBride *et. al.* reported a detection limit of 3 ng/mL MS2, using a bead-based assay and a flow cytometer[58]. Although the assay detected with the flow

cytometer is more sensitive, it is more likely that the fluidic channel with IDA electrode detection can be developed into a hand-held device to be used in the field. The logical next step would be to include automated bead preparation within the fluidic device.

Table 4. Comparison of 3 electrochemical immunoassay systems with IDA electrodes.

	1st	2nd	3rd
Electrodes	Coplanar IDA	Comb IDA	3 electrodes w/ Comb IDA
Gap	1.6 μm, 2.5 μm	2.5 μm, 4.5 μm	1.6 μm, 2.5 μm
Setup	Vertical	Horizontal	Fluidic channel
Assay time	10 min.	2 min.	5 min.
Minimum detectable # of beads	1000 beads (1.2 fmole)	60 beads (70 amole)	130 beads (150 amole)
Reproducibility	σ=10%, exclude some data	σ=9%, exclude some data	σ=9%
Accomplishment	Coupling redox cycling and enzyme label	Improvement of sensitivity and response time	Improved stability and reproducibility, total analysis system

REFERENCES

1. D.G. Sanderson, L.B. Anderson, Filar electrodes: Steady-state currents and spectroelectrochemistry at twin interdigitated electrodes, Anal. Chem. **57**, 2388-2393 (1985).

2. H. Tabei, M. Takahashi, S. Hoshino, O. Niwa, T. Horiuchi, Subfemtomole detection of catecholamine with interdigitated array carbon microelectrodes in HPLC, Anal. Chem., **66**, 3500-3502 (1994)

3. Niwa, M. Moria, H. Tabei, Highly sensitive and selective voltammetric detection of dopamine with vertically separated interdigitated array electrodes, Electroanal., **3**,163 (1991).

4. Niwa, M. Moria, H. Tabei, Highly selective electrochemical detection of dopamine using interdigitated array electrodes modified with nafion polyester ionomer layered film, Electroanal., **6**, 237 (1994).

5. M. J. Doyle, H. B. Halsall, W. R. Heineman, Enzyme-linked immunoadsorbent assay with electrochemical detection of alpha 1-acid glycoprotein, Anal. Chem., **56**(13), 2355-2360 (1984)

6. W.R. Heineman, H.B. Halsall, Strategies for electrochemical immunoassay, Anal. Chem., **57,** 1321A-1330A (1985).

7. U. Hafeli, W. Schutt, J. Teller, M. Zborowski, Scientific and clinical applications of magnetic carriers, 1997, Kluwer Academic Publishers, New York.

8. J. Choi, K. W. Oh, A. Han, N. Okulan, C. A. Wijayawardhana, C. Lannes, S. Bhansali, K. T. Schlueter, W. R. Heineman, H. B. Halsall, J. H. Nevin, A. J. Helmicki, H. T. Handerson, C. H. Ahn, Development and characterization of microfluidic devices and systems for magnetic bead-based biochemical detection, Biomedical microdevices, **3**(3), 191-200 (2001)

9. Niwa, M. Moria, H. Tabei, Electrochemical-behavior of reversible redox species at interdigitated array electrodes with different geometries - consideration of redox cycling and collection efficiency, Anal. Chem., **62**, 447-452 (1990)

10. K. Aoki, M. Morita, O. Niwa, H. Tabei, Quantitative analysis of reversible diffusion-controlled currents of redox species at interdigitated array electrodes under steady-state conditions, J. Electroanal. Chem. **256**, 269-282 (1988).

11. Niwa, M. Morita, H, Tabei, Highly sensitive small volume voltammetry of reversible redox species with an IDA electrochemical cell and its application to selective detection of catecholamine, Sens. Actuator B, **14**, 558-560 (1993)

12. B. Jin, W.Qian, Z. Zhang, H. Shi, Application of the finite analytic numerical method, part 1. Diffusion problems on coplanar and elevated interdigitated microarray band electrodes. J. Electroanal. Chem,. **411**, 29-36 (1996).

13. G.C.Fiaccabrino, M Koudelka-Hep, Thin-film microfabrication of electrochemical transducers, Electroanal., **10**(4), 217-222 (1998)

14. S. A. Campbell, The science and engineering of microelectronic fabrication, 1996, Oxford University Press, New York, 281-307

15. P. Van Gerwen, K. Baert and R. Rossau, Impedimetric Detection System and Method of Production Thereof, Patent PCT/EP96/05290, (1996)

16. P. Van Gerwen, W. Laureyn, A. Campitelli, P. Jacobs, P. Detemple, K. Baert, W. Sansen and R. Mertens, Cost Effective Realization of Nanoscaled Interdigitated Electrodes, J. Micromech. Microeng., **10** N1-N5 (2000)

17. O. Niwa, H. Tabei, Voltammetric measurements of reversible and quasi-reversible redox species using carbon-film based interdigitated array microelectrodes, Anal. Chem., **66**, 285 (1994)

18. G.C.Fiaccabrino, X. M. Tang, N. Skinner, N. F. deRooij, M. KoudelkaHep, Interdigitated microelectrode arrays based on sputtered carbon thin-films, Sens. Actuator B, **35**(1-3), 247-254, (1996)

19. S.S. Iqbal, M.W. Mayo, J.G. Bruno, B. V. Bronk, C.A. Batt, J.P.Chambers, A review of molecular recognition technologies for detection of biological threat agents, Biosensors Bioelectron., **15**, 549-578 (2000)

20. R.B.Herman, D.W.Mercer, Immunodiagnosis of cancer, 1990, 2nd Ed., Marcel Dekker Inc., New York, V-iv, 17-19

21. M. Aslam, A. Dent , Bioconjugation, 1998, Groves Dictionaries Inc, New York.

22. H.T. Tang, C.E. Lunte, H.B. Halsall, W.R. Heineman, *p*-aminophenyl phosphate: an improved substrate for electrochemical enzyme immunoassay, Anal. Chim. Acta, **214,** 187 (1988)

23. N. Kaneki, Y. Xu, A. Kumari, H. B. Halsall, W. R. Heineman, P. T. Kissinger, Electrochemical enzyme-immunoassay using sequential saturation technique in a 20-µl capillary - digoxin as a model analyte, Anal. Chim. Acta, **287**(3), 253-258 (1994)

24. R. Q. Thompson, M. Porter, C. Stuver, H. B. Halsall, W. R. Heineman, E. Buckley, M. R. Smyth, Zeptomole detection limit for alkaline-phosphatase using 4-aminophenylphosphate, amperometric detection, and an optimal buffer system, Anal. Chim. Acta, **271**(2), 223-229 (1993)

25. C.G. Bauer, A.V. Eremenko, .Ehrentreich-Forster, F.F. Bier, A. Makower, H.B. Halsall, W.R. Heineman, F.W. Scheller, Zeptomole-detecting biosensor for alkaline phosphatase in an electrochemical immunoassay for 2,4-dichlorophenoxyacetic acid, Anal. Chem., **68,** 2453-2458 (1996).

26. T. Huang, A.Warsinke, T. Kuwana, F.W. Scheller, Determination of L-phenylalanine based on an NADH-detecting biosensor, Anal. Chem., **70,** 991-997 (1998)

27. V. C. Yang, T. T. Ngo, Biosensors and their applications, 2000, Plenum publisher, New York, 113-130.

28. N. J. Ronkainen-Matsuno, J. H. Thomas, H. B. Halsall, W. R. Heineman, Electrochemical inmunoassay moving into the fast lane, Trends in Anal. Chem., **21**(4), 213-226 (2002)

29. C. A. Wijayawardhana, S. Purushothama, M. A. Cousino, H. B. Halsall, W. R. Heineman, Rotating disk electrode amperometric detection for a bead-based immunoassay. J. Electroanal. Chem., **468**, 2-8 (1999).

30. H. Harma, P. Lehtinen, H. Takalo, T. Lovgren, Immunoassay on a single microparticle: the effect of particle size and the number on a miniaturized time-resolved fluorometric assay of free prostate-specific antigen, Anal. Chim. Acta, **387,** 11-19 (1999)

31. H. Harma, P. Aronkyto, T. Lovgren, Multiplex immunoassays on size-categorized individual bead using time-resolved fluorescence, Anal. Chim. Acta, **410,** 85-96 (2000)

32. J. Ugelstad, A. Berge, T. Ellingsen, Preparation and application of new monosized polymer particles, Prog. Polym. Sci., **17,** 87-161 (1992)

33. http://en.wikipedia.org/wiki/Superparamagnetism

34. W. Zhang, C. H. Ahn, A microfabricated planar magnetic particle separator with optically inspectable flowchannel, 18th Annual international conference of the IEEE engineering in medicine and biology society, Amsterdam, 1996, 252-253

35. M. Tondra, M. Granger, R. Fuerst, M. Porter, C. Nordman, J. Taylor, S. Akou, Design of integrated microfluidic device for sorting magnetic beads in biological assays, IEEE transactions on magnetics, **37**(4), 2621-2623 (2001)

36. H. Suzuki, C. Ho, A magnetic force driven chaotic micro-mixer, 15th IEEE International Conference on Micro Electro Mechanical Systems: Las Vegas, Nevada, January 20-24, 2002, 40-43

37. T. Takagi, N. Nakajima, Architecture combination by microphotoforming process, Proc. IEEE MEMS, 1994, pg. 211-216.

38. K. W. Vogt, P. A. Kohl, W. B. Carter, R. A. Bell, L. A. Bottomley, Characterization of thin titanium oxide adhesion layers on gold: resistivity, morphology, and composition, Surface science, **301**, 203-213 (1994)

39. K. Yu, M. Feldbaum, T. Pandhumsoporn, P. Gadgil,, Deep anisotropic ICP etching designed for high volume MEMS manufacturing. SPIE, **3874**, 218-227 (1999)

40. H. Szuki, T. Hirakawa, S. sasaki, I. Karube, Micromashined liquid-junction Ag/AgCl reference electrode, sens. actuators B, **46** 146-154 (1998)

41. S. Ito, H. Hachiya, K. Baba, Y. Asano, H. Wada, Improvement of the silver/silver chloride reference electrode and its application to pH measurement , Talanta, **42**(11), 1685-1690 (1995)

42. H. Angerstein-Kozlowska, B.E. Conway, W.B.A. Sharp, The real condition of electrochemically oxidized platinum surfaces, J. Electroanal. Chem., **43**, 9-36 (1973).

43. P.N. Ross, Structure sensitivity in the electrocatalytic properties of Pt, J. Electrochem. Soc., **126**, 67-77 (1979).

44. C.E. Chidsey, B. J. Feldman, C. Lundgren, R.W. Murray, Micrometer-spaced platinum interdigitated array electrode: Fabrication, theory, and initial use, *Anal. Chem*., **58,** 601-607 (1986).

45. Niwa, Y Xu, H. B Halsall, W R. Heineman, Small-volume voltammetric detection of 4-aminophenol with interdigitated array electrodes and its application to electrochemical enzyme immunoassay, Anal. Chem., **65** (11), 1559-1563 (1993)
46. M. Cardosi, S. Birch, J. Talbot, A. Phillips, An electrochemical immunoassay for Clostrium perfringens phospholipase C, Electroanal., **3**, 169-176 (1991)

47. www.Dynal.com

48. C. A. Wijayawardhana, H. B. Halsall, W. R. Heineman, Microvolume rotating disk electrode (RDE) amperometric detection for a bead-based immunoassay, Anal. Chim. Acta, **399**, 3-11 (1999)

49. S. V. Sasso, R. J. Pierce, R. Walla, A. M. Yacynych, Electropolymerized 1,2-diaminobenzene as a means to prevent interferences and fouling and to stabilize immobilized enzyme in electrochemical biosensors, Anal. Chem., **62**, 1111-1117 (1990).

50. http://www.scscookson.com/applications/mems.cfm

51. W. Fiers, R. Contreras, F. Duerinck, G. Haegeman, D. Iserentant, J. Merregaert, W. M. Jou, F. Molemans, A. Raeymaekers, A. V. Berghe, G. Volckaert, M. Ysebaert, Complete nucleotide sequence of bacteriophage MS2 RNA: primary and secondary structure of the replicase gene, Nature, **260**(5551), 500-507 (1976)

52. K. Valegard, L. Liljas, K. Fridborg, T. Unge, The three-dimensional structure of the bacterial virus MS2, Nature, **345**, 36-41 (1990)

53. J. H. Strauss Jr., R. L. Sinsheimer, Purification and properties of bacteriophage MS2 and of its ribonucleic acid, J. Mol. Biol., **7**, 43-54 (1963)

54. W. D. Burrows, S. E. Renner, Biological Warfare Agents as Threats to Potable Water, Environ. Health Perspect., **107**, 975-984 (1999)

55. Niwa, Y. Xu, H. B. Halsall, W. R. Heineman, Small-volume voltammetric detection of 4-aminophenol with interdigitated array electrodes and its application to electrochemical enzyme immunoassay, Anal. Chem., **65**(11), 1559-1563 (1993)

56. N. Honda, K. Emi, T. Katagiri, T. Irita, S. Shoji, H. Sato, T. Homma, T. Osaka, M. Saito, J. Mizuno, and Y. Wada, 3-D Comb Electrodes for Amperometric Immuno Sensors, Digest of Technical Papers for Transducers'03 the 12th International Conference on Solid-State Sensors, Actuators, and Microsystems, June 8-12th, 2003, Boston, MA

57. C. A. Rowe, L. M. Tender, M. J. Feldstein, J. P. Golden, S. B. Scruggs, B. D. MacCraith, J. J. Cras, F. S. Ligler, Array Biosensor for Simultaneous Identification of Bacterial, Viral, and Protein Analytes, Anal. Chem.**, 71,** 3846-3852 (1999)

58. M. T. McBride, S. Gammon, M. Pitesky, T. W. O'Brien, T. Smith, J. Aldrich, R. G. Langlois, B. Colston, K. S. Venkateswaran, Multiplexed Liquid Arrays for Simultaneous Detection of Simulants of Biological Warfare Agents, Anal. Chem., **75**, 1924-1930 (2003)